UNIVERSITY OF CALIFORNIA SANTA CRUZ

Paleomagnetic Correlation of Yellowstone Hotspot Related Rheomorphic Ignimbrite in the Snake River Plain of Southern Idaho, USA

A dissertation submitted in partial satisfaction of the requirements for the degree of

DOCTOR OF PHILOSOPHY

In

EARTH SCIENCES

by

David Ryan Finn

March 2016

The Dissertation of David R. Finn is approved:

_____
Emeritus Professor, Robert Coe, Chair

_____
Professor Jeremy Hourigan

_____
Research Geophysicist Xixi Zhao

_____
Tyrus Miller
Vice Provost and Dean of Graduate Studies

TABLE OF CONTENTS

List of Figures, Tables, and Supplementary Material

Chapter 1: Magnetic anisotropy in rhyolitic ignimbrite, Snake River Plain: implications for using remanent magnetism of volcanic rocks for correlation, paleomagnetic studies and geological reconstructions

Chapter 2: A New Protocol for 3-Axis Static Alternating Field Demagnetization of Rocks

Chapter 3: Distinguishing and Correlating deposits from large Ignimbrite Eruptions Using Paleomagnetism: the Cougar Point Tuffs (Mid-Miocene), Southern Snake River Plain, Idaho, USA

Chapter 3 Supplementary Material

Chapter 3 Supplementary Tables Available for Download

Abstract

Paleomagnetic Correlation of Yellowstone Hotspot Related Rheomorphic Ignimbrite in the Snake River Plain of Southern Idaho, USA

By

David Ryan Finn

Large-volume explosive volcanic eruptions from the Bruneau-Jarbidge region of southwestern Idaho are thought to have impacted mid-Miocene environments across continental USA and probably perturbated global climate. They are recorded by widely dispersed tephras and a proximal succession of welded rhyolitic ignimbrites known as the Cougar Point Tuffs (CPT). Ignimbrite successions similar to the CPT in age, chemistry, and physical characteristics are present along both the southern and northern margins of the central Snake River Plain (cSRP). Identification of individual eruption-units spanning between distant locations is essential to understand the true scale and frequency of volcanism. Fortunately, the CPT record an unusual pattern of geomagnetic field directions that provides the basis for robust stratigraphic correlations. Paleomagnetic characterization of eruption-units based on geomagnetic field variation has a resolution on the order of a few centuries or less, providing the means for strong tests of whether two deposits could have been emplaced from the same eruption or from temporally separate events. In this thesis, I present paleomagnetic, geochemical, mineralogical, and geochronologic evidence for correlation of the CPT eastward to the Brown's Bench escarpment (6 common

eruption-units) and Cassia Mountains (3 common eruption-units) regions of southern Idaho. The new stratigraphy presented here significantly reduces the frequency and increases the scale of known cSRP ignimbrite eruptions.

Individual ignimbrite cooling-units, however, display significant variation of magnetic remanence directions and other magnetic properties. This complicates paleomagnetic correlation. The ignimbrites are intensely welded and exhibit mylonite-like flow-banding produced by rheomorphic ductile shear during emplacement, prior to cooling below magnetic blocking temperatures. This results in a large anisotropy of thermal remanent magnetization, which in turn results in large deflections of the stable remanence direction. To obtain reliable paleomagnetic directions, the anisotropy of anhysteretic remanence was measured in the CPT to correct for magnetic anisotropy. In addition to magnetic anisotropy, the strong preferential alignment of anisotropic grains results in the acquisition of a significant component of gyroremanence (GRM) during alternating field demagnetization. The accepted method proposed by Dankers and Zjiderveld (1981) for excluding GRM affected measurements requires nearly triple the amount of lab work, and by consequence, is almost never regularly implemented on large batches of samples. Here, I present a laboratory procedure and subsequent analysis (SI method) that removes the effects of GRM in static AF demagnetization without requiring extra laboratory work.

Acknowledgments

I consider myself incredibly lucky to have advisors like Xixi Zhao and Rob Coe. Rob gave me freedom and encouragement to explore my own ideas, and seemingly had endless amounts of time for discussing science, working with me in the lab, and in the later stages, dramatically improving my writing. Under his guidance I gained invaluable knowledge of paleomagnetism and how to approach science in general. Early work with Xixi on several different tectonic problems in Asia in the field and in the laboratory provided me with a great introduction to paleomagnetism, as well as instilling in me the value of hard work and dedication. His continued support up to the end of my graduate career has been a huge factor in my completion of this significant accomplishment.

Thanks to all who helped along the way with field and laboratory work, scientific analysis, writing, and in teaching (in no particular order): Mike Branney, Thomas Knott, Marc Reichow, Bill Bonnichsen, Michael Storey, Walter Schillinger, Eli Morris, Ethan Brown, Grant Rhea-Downing, Francesca Spinardi, Andrew Pike, Hilde Schwarz, Jeremy Hourigan, Henry Kelly, Jordan Murphy, Sadie Bodiford, Sophie Foster, Rachel Hohn, Zach Mayo, Liam McDonnell, Fabian Wadsworth, Mark Baldwin, Jun Meng, Yu-Xiu Zhang, Chengshan Wang, Shihong Zhang, Peter Lippert, Yalin Li, JinGen Dai, and all the undergraduates I have TA'd. Finally, this wouldn't have been possible without the teaching assistant support from the Earth Science Department (n=22).

Previously Published Material:

The text of this dissertation includes modified reprints from previously published material. Chapter 1 is a slightly edited reprint of Finn, D. R., Coe, R. S., Kelly, H., Branney, M., Knott, T., & Reichow, M. (2015). Magnetic anisotropy in rhyolitic ignimbrite, Snake River Plain: implications for using remanent magnetism of volcanic rocks for correlation, paleomagnetic studies and geological reconstructions. Journal of Geophysical Research: Solid Earth. Coauthor Coe directed the research. Coauthor Kelly helped with all aspects of the paper including field work, laboratory work, and writing. Coauthors Branney, Knott, and Reichow helped with the field work and writing.

Dissertation Introduction

Migration of the Yellowstone hotspot center tracks northeast along the central Snake River Plain (cSRP), leaving a succession of calderas, bimodal rhyolitic and basaltic volcanism, and crustal deformation. Large-scale explosive volcanism common to this province between 13–8 Ma is characterized by unusually high-temperature, intensely welded, rheomorphic rhyolitic ignimbrites, typical of what is now known as 'Snake River (SR)-type volcanism'. Individual eruption volumes likely exceed 450 km^3 but are poorly known due to the difficulty of correlating units between widely spaced (50-200 km) exposures along the north and south of the plain. Radiometric dating does not have the resolution to identify the eruptive units. In this thesis I use a combination of paleomagnetic, chemical and geochronologic characterization to establish robust correlations and better constrain eruption volumes and frequencies.

Paleomagnetic correlation using the stable remanence, which is the main focus of my thesis, has the advantage of very high temporal resolution of the order of centuries. This is due to the geologically rapid rate of geomagnetic secular variation and high accuracy to which extrusive rocks may record the instantaneous direction of the magnetic field. In chapter 3 of this thesis I demonstrate the correlation of the Cougar Point Tuff in southwest Idaho eastward to the Brown's Bench escarpment (6 common eruption-units) and Cassia Mountains (3 common eruption-units) regions of southern Idaho. The new stratigraphy presented here has significantly reduced the known

frequency and increased the known scale of known cSRP ignimbrite eruptions.

I have found, however, that the use of paleomagnetism is complicated by a large variation in the paleomagnetic direction that sometimes exists both within and between sub-lithologies of the same flow. Individual SR-type ignimbrite cooling-units have an upper and lower glassy margin (vitrophyre) enclosing a lithoidal (microcrystalline) zone. These vitrophyre lithologies often have a shallow paleomagnetic direction compared to the lithoidal lithologies, which results from a large magnetic anisotropy. I have found a relationship between anisotropy of thermal remanent magnetization (ATRM), coercivity, natural remanent magnetization intensity, and deflection of remanence direction. A strong lineation observed in the ATRM anisotropy suggests contemporaneous rheomorphic shear strain of the welding fabric during early stages of emplacement plays a key role in generating magnetic anisotropy. The much lower anisotropy of the lithoidal zone implies that crystallization somehow helps anneal this anisotropy prior to cooling below the unblocking temperature of the constituent magnetic minerals. The glassy margins must be retaining an anisotropic fabric related to emplacement which affects their ability to accurately record the magnetic field during cooling. The anisotropic fabric in the lithoidal zone is overprinted by continued grain growth and/or alteration and, therefore, more accurately records the paleomagnetic field direction. This lithoidal lithology, is therefore, the most optimal target for paleomagnetic sampling of strongly

welded and rheomorphic ignimbrites. Although much lower, the lithoidal zone may still have a magnetic anisotropy capable of deflecting remanence, and should be evaluated and corrected for as necessary.

In addition to magnetic anisotropy, the strong preferential alignment of anisotropic grains results in the acquisition of a significant component of gyroremanence (GRM) during alternating field (AF) demagnetization. Static three-axis AF demagnetization is the most common method regularly implemented for removing magnetic components of rock samples. This method is so widely used that one of its main limitations, the acquisition of gyroremanence (GRM), is often not accounted for or even discussed. The presence of GRM likely interferes more than is recognized in accurate determination of the most stable remanence. The accepted method proposed by Dankers and Zjiderveld (1981) for excluding GRM affected measurements requires nearly triple the amount of lab work, and by consequence, is almost never regularly implemented on large batches of samples. In this thesis, I present a laboratory procedure and subsequent analysis (SI method) that removes the effects of GRM in static AF demagnetization without requiring extra laboratory work. This paper, therefore, describes a new standard protocol for efficient static AF demagnetization of rocks.

Chapter 1

Magnetic anisotropy in rhyolitic ignimbrite, Snake River Plain: implications for using remanent magnetism of volcanic rocks for correlation, paleomagnetic studies and geological reconstructions

Published: **Finn, D. R.,** Coe, R. S., Kelly, H., Branney, M., Knott, T., & Reichow, M. (2015). Magnetic anisotropy in rhyolitic ignimbrite, Snake River Plain: implications for using remanent magnetism of volcanic rocks for correlation, paleomagnetic studies and geological reconstructions. Journal of Geophysical Research: Solid Earth.

1. Introduction

Characterizing the direction of stable thermoremanent magnetization (TRM) of lavas and ignimbrites has long been used to aid high-precision geochronologic and stratigraphic correlation and to estimate duration of volcanic activity [*e.g.*, Grommé et al., 1972; Choiniere and Swanson, 1979; Bogue and Coe, 1981; Hildreth and Mahood, 1985, Speranza et al., 2012; Ort et al., 2013; Piper et al., 2013]. TRM of extrusive rocks can resolve with high accuracy the direction of the geomagnetic field as it changes during typical geomagnetic secular variation, which occurs on the order of centuries. In volcanology, TRM is also used in breccia and fold tests to determine whether initial emplacement and subsequent folding pre-or post-dates cooling [Piper et al., 1997; McClelland et al., 2003; Geissman et al., 2010; Lesti et al., 2011]. The premise of all these studies is that the TRM of the volcanic rock faithfully preserves the orientation of the geomagnetic direction relative to the position of the rock as it cooled through the blocking temperatures of the magnetic minerals. However, we have discovered significant departures from this basic assumption.

Northeastward migration of the Yellowstone hotspot across Idaho was accompanied by voluminous explosive super-eruptions [Smith and Braile, 1984; Pierce and Morgan, 1992 and 2009; **Fig. 1**]. Thick rhyolitic successions of outflow ignimbrites exposed in widely separated massifs along the northern and southern margins of the plain were derived from Mid-Miocene calderas now buried beneath basalt lavas in the central Snake River Plain [e.g. Bonnichsen and Citron 1982; Honjo et al., 1992;

Perkins et al., 1995; McCurry et al., 1996; Cathey and Nash, 2004; Andrews et al., 2008]. Correlation of individual ignimbrites between the widely separated locations is required to determine the sizes and frequency of the rhyolitic eruptions [e.g. Ellis et al., 2012]. Then their regional geographic distributions can be ascertained and volumes of individual eruptions estimated to infer magmatic productivity, how this changed with time, and the potential relationship with climate and tectonics.

Paleomagnetic cores were collected from 134 sites to help build a regional stratigraphy between the dozens of similar-looking welded ignimbrites in the central Snake River Plain. This was combined with detailed field logging, geochemical characterization, and high-precision radiometric dating. For correlation, paleomagnetism has proven helpful, invaluable in some cases, but sometimes is complicated by a significant variation in the paleomagnetic direction both within and between sub-lithologies of the same deposit. In general, glassy lithologies such as vitrophyre tend often to have a shallower direction than the lithoidal zone (**Fig. 2**). Mechanisms proposed to account for discrepant paleomagnetic directions in ignimbrites elsewhere have included sub-blocking-temperature grain rotation [Geissman, 1980; Rosenbaum, 1986, Uno et al., 2014], chemical remagnetization during devitrification [Reynolds, 1977], secular variation during prolonged cooling [Wells and Hillhouse, 1989], and large magnetic anisotropy [Gattacceca and Rochette, 2002]. Most of these ignimbrites are significantly less-intensely welded than Snake-River-type ignimbrites.

This paper presents paleomagnetic results for a profile sampled through a particularly well-characterized rheomorphic ignimbrite in the central Snake River Plain. The ignimbrite is a simple cooling-unit emplaced during a single eruption, and it features almost a meter of baked soil at its base. This is a great advantage because the baking remanence is almost certainly a stable thermal remanent magnetization (TRM) that faithfully records the field orientation at the time the baked soil and the overlying ignimbrite cooled. Our results reveal that those samples that exhibit a large discrepancy between their direction of stable remanence and that of the baked soil are characterized by having a large anisotropy of TRM (ATRM). In the following sections we examine how the anisotropy may have formed and how the deflection of remanence can be avoided or corrected to record more faithfully the paleo-geomagnetic field. This may be useful in other studies of rheomorphic ignimbrites and rhyolitic lavas

2. The Grey's Landing Member

The c. 8 Ma Grey's Landing Member of the Rogerson Formation in southern Idaho [Andrews et al., 2008; Andrews et al. 20011] is the type ignimbrite in a recently defined class of volcanism known as Snake River (SR)-type volcanism [Branney et al., 2004 and 2008]. It is a high-temperature, rhyolitic ignimbrite, lithic-poor, metaluminous and ferroan, with low $\delta^{18}O$ and welding so intense that the lithology is dense, flow-banded and 'lava-like' (Branney and Kokelaar 1992). Intense

rheomorphic shear during emplacement produced a mylonite-like flow-lamination with a prominent extensional lineation and intrafolial sheath folds. The Grey's Landing ignimbrite is at least 60 m thick, with a devitrified interior, thin laminated basal ash fall layer, and upper orange tuff, and overlies a paleosol and other fused parts of the Brown's View Member ignimbrite (**Fig 3**). Its estimated volume in the Rogerson area exceeds 13 km3, which is a minimum estimate for this eruption-unit as it likely correlates with ignimbrite exposures far outside the graben [Andrews and Branney, 2011]. The main zones of the Grey's Landing ignimbrite, plus its associated ash fall layers at the base and top and the baked and fused underlying unit, are described below and depicted in **Fig. 3** (see Andrews and Branney [2011] for the microfabrics of each zone). They occur at one or both of the two localities shown in **Fig. 4**.

2.1. Baked and fused zones (BS, FBM, UBM) of the underlying Brown's View Member

The Brown's View Member paleosol (BS), just beneath the Grey's Landing fused basal ash fall layer, is baked to orange terracotta. Its maximum thickness is 90 cm and it displays leaf casts on its upper surface. Immediately below is a reworked and bioturbated rhyolitic ash, once called the 'Backwater Member' by Andrews et al. [2008], that is fused to black vitrophyre (FBM) for about a meter at the top and becomes progressively lighter and less glassy below (UBM).

2.2. Fused Basal Ash Fall (Zone FAF)

A parallel-laminated tuff layer, ~60 cm thick, underlies the Grey's Landing ignimbrite and records ash fallout during the first phase of the Grey's Landing explosive eruption. It has been fused to a dark grey vitrophyre by emplacement of the overlying hot ignimbrite. The parallel laminations have laterally constant thicknesses with no evidence of rheomorphic deformation.

2.3. Glassy Basal Vitrophyre

2.3.1. Eutaxitic Lower Basal Vitrophyre (Zone LBV)

The lowest part (< 0.5 meters thick) of the basal vitrophyre (Zone LBV) exhibits a microscopic eutaxitic fabric defined by oblate ash shards and attenuated vesicles. Fabrics indicate that it has undergone welding compaction and a small component of non-coaxial ductile shear strain. The magnitude of the strain increases as it grades into the overlying zone.

2.3.2 Flow-banded Upper Basal Vitrophyre (Zone UBV)

Zone UBV is the upper part of the lower black vitrophyre that is flow-laminated with rotated crystals, asymmetric microscopic folds, prolate vesicles and rare isoclinal intrafolial F1 sheath folds. These features record intense non-coaxial ductile shear strain during hot emplacement. It is 0.5 m thick at the southern drilling location in **Fig. 4**, but increases to several meters elsewhere. Spherulites are common and increase upwards toward the devitrification front.

2.4. Devitrified Lithoidal Center

2.4.1. Lower Transitional Lithoidal Zone (LL)

Just above the devitrification front (UBV-LL contact), the lithoidal lithology displays a gradation in color, becoming an increasingly lighter grayish tan. This color gradation is approximately 2 m thick and is likely related to the remaining glass content. The magnetic properties of this lower gradational Zone LL, which are discussed below in detail, gradually change over this interval as well. This zone exhibits ductile rheomorphic fabrics such as flat-lying flow-banding and is characterized by increasingly abundant lithophysea closer to the devitrification front **(Fig. 3).**

2.4.2. Upper Lithoidal Zone (Zone UL)

Zone UL is the light gray to tan thoroughly devitrified (microcrystalline) lithology that makes up the bulk of the lithoidal interior. It is up to 60 m-thick and exhibits ductile rheomorphic fabrics similar to those in the zones below. The base of Zone UL consists of a pervasive flat-lying flow lamination that is accompanied by an intense stretching lineation and intrafolial, isoclinal F1 sheath folds, which indicates high ductile shear during emplacement (Lower Flat Domain, of Andrews and Branney, 2011). In the central and upper part of Zone UL, the fabric and F1 folds are refolded by secondary (F2) rheomorphic folds with wavelengths of 1-20 m. In this ‘upper

contorted domain' the original flat-lying welded fabric ranges in attitude from horizontal to vertical.

2.5. Upper Vitrophyre (Zone UV) and overlying Orange Tuff (Zone OT)

The upper part of the Grey's Landing ignimbrite is best exposed near Salmon Reservoir Dam (**Fig. 4**). An intensely folded and locally autobrecciated upper vitrophyre (Zone UV) is overlain by a mainly non-welded orange tuff (Zone OT) in which the lower ~25 cm is locally fused (**Fig. 3**) by contact with the underlying ignimbrite. Andrews and Branney [2011] tentatively interpreted the orange tuff as a disturbed ash-fall deposit on the basis of its good sorting and general absence of crystals, but emplacement by cooler density currents cannot be excluded.

3. Methods

3.1 Sample Collection

The Grey's Landing ignimbrite was sampled at two locations near Rogerson, Idaho **(Fig. 4)**. A vertical profile was collected at the southernmost sampling location at Backwaters on the east side of Salmon Reservoir (**red star in Fig. 4**). This profile includes the underlying Brown's View Member, baked soil, fused basal ash fall, basal vitrophyre, and lower through upper lithoidal zones. At this location the ignimbrite is ~60 meters thick, though its full thickness is not seen. The upper vitrophyre and Orange Tuff are absent at this drilling site and were sampled ~10 km away at the Salmon Reservoir Dam (**blue circle in Fig. 4).** Paleomagnetic cores were collected

with a gas-powered drill and oriented with a magnetic compass. Correction for the local magnetic field anomaly was made individually for each core by using the observed azimuth of the sun.

3.2 Laboratory Procedures

Laboratory work was conducted at the University of California, Santa Cruz. Anisotropy of magnetic susceptibility (AMS) and susceptibility-versus-temperature curves were measured using a Kappabridge KLY-3 susceptibility bridge with a CS-2 furnace and analyzed with AGICO software. Magnetic hysteresis parameters were determined with a Princeton Measurements MicroMag 2900 alternating gradient magnetometer. Magnetic remanence measurement, automated progressive alternating field (AF) demagnetization up to 200 mT, and anhysteretic remanent magnetization (ARM) acquisition were performed on a 2G cryogenic magnetometer and Sapphire Instruments demagnetizer using a customized sample handler and software [Morris et al., 2009].

Thermal demagnetization was carried out in a home-built oven, housed in a magnetically shielded room along with the AF demagnetizer and cryogenic magnetometer. Anisotropy of thermal remanence (ATRM) experiments were made in a custom-built paleointensity oven by applying thermal remanent magnetizations in known directions. Fisher statistics [Fisher, 1953] and principal component analysis [Kirschvink, 1980] were used to average individual sample directions and to calculate

the best-fit lines to demagnetization data, respectively.

3.3 Anisotropy of Thermal Remanent Magnetizations (ATRM)

The equation relating the applied magnetic field vector (H_{app}) during cooling to the acquired thermal remanent magnetization vector (M_{obs}) of a sample is

$$M_{obs}=\chi * H_{app} \quad (1)$$

where χ is the 3x3 symmetric ATRM tensor. The ATRM ellipsoids were determined by heating each sample four times in air to 680°C using an approach similar to that of Stephenson et al. (1986). Namely, prior to the first heating, an ARM was applied and measured in the core Z using a 0.1 mT DC field applied over a 155 mT to 0 mT AF range. After the first heating the samples were cooled in the absence of a field to measure the baseline magnetization, which later was subtracted from all subsequent measurements. For half the samples another identical ARM was then applied and measured to check for changes in the magnetic mineralogy (see second-to-last column in Table 1). During the next heating a 0.5 Oe field was applied along the X direction, and then the remanence components M_{xx}, M_{xy}, M_{xz} were measured in the X, Y, Z directions, respectively. This was repeated in the third and fourth heatings where the field was applied in the Y and Z directions, respectively. The observed remanent magnetizations consist of the following array of nine values:

M_{xx} M_{xy} M_{xz} (field along x)

M_{yx} M_{yy} M_{yz} (field along y)

M_{zx} M_{zy} M_{zz} (field along z)

Ideally, the off-diagonal pairs of this array should be symmetric (e.g. $M_{xy}=M_{yx}$), so that dividing the six independent coefficients by the applied field magnitude H_{app} would give the components of the ATRM tensor. In our experiments the average difference observed between the off-diagonal elements was ~10% of the average TRM. This significant discrepancy is probably due to continued chemical alteration during subsequent heating steps, as well as to smaller orientation and other experimental errors. The least-squares-best-fit tensor to the nine measurements for this case is obtained by simply taking the average of each off-diagonal pair.

The maximum ($K1_{atrm}$), intermediate ($K2_{atrm}$), and minimum ($K3_{atrm}$) principal susceptibility directions and magnitudes are found by computing the eigenvectors and eigenvalues of χ, respectively. The anisotropy (P), lineation (L) and foliation (F) parameters used in this paper are defined by P = K1/K3, L = K1/K2, and F = K2/K3. Subscripts P_{ATRM} and P_{AMS} will be used to distinguish between ATRM and AMS anisotropy parameters.

A large ATRM causes the observed magnetization of a sample to deflect away from the applied field direction and toward a direction or plane of higher susceptibility. To calculate the paleofield direction corrected for the anisotropy of these samples, the

inverse of the laboratory measured ATRM tensor χ is multiplied by the observed remnant direction (M_{rem})

$$H_{cor}=Inv(\chi)*M_{rem} \quad (2)$$

4. Experimental Results

4.1 Introduction

We have obtained useful remanence directions from three core samples from the non-fused and four samples from the fused zones of the upper Browns View Member, eight samples from the baked soil (BS), three samples from the basal ash fall, three samples from the lower basal vitrophyre (LBV), five samples from the upper basal vitrophyre (UBV), five samples from the lower lithoidal (LL), nine samples from the lithoidal zone (UL), fifteen samples from the upper vitrophyre (UV), and ten samples from the upper orange tuff (OT; **Table 1)**. One core (LBV9) from zone LBV carries only a low-coercivity magnetic direction that we exclude as a normal overprint (**Table 2)**. Another core, UBV17 lost its orientation after being demagnetized and having its AMS measured, but before the ATRM measurement. Therefore, the orientation of the ATRM tensor for this core is unknown and the related directional data will not be presented (i.e. the K1-K3 directions and remanence correction). The glassy LBV and UBV zones are nearly indistinguishable in the field, have a gradational boundary in terms of both their physical and magnetic properties, and are anisotropic. For this reason, samples from these two sub-lithologies will be averaged

together for analysis of lithology mean directions, but they will be grouped separately in tables and discussions of individual sample's magnetic properties to highlight end-member characteristics of the basal vitrophyre. Only AF demagnetization and AMS measurements were performed on the upper vitrophyre and fused upper ash.

4.2 Magnetic Mineralogy

Susceptibility-versus-temperature heating curves measured in argon gas show a dominant Curie temperature of ~580°C in the baked soil and UBV, LL and UL zones, indicating titanium-poor magnetite is the dominant magnetic mineral **(Fig. 5).** In contrast, the most important magnetic phase in zone LBV is titanium-rich magnetite, as demonstrated by a principal Curie temperature of ~200°C. During laboratory heating this phase altered to titanium-poor magnetite, and samples heated at slower rates over longer periods of time altered more. Zones UBV, LL, and UL display small inflections in their heating curves at temperatures around 200-300°C, suggesting the presence of a small percentage of titanium-rich magnetite. All lithologies except the baked soil and upper lithoidal had some susceptibility remaining at temperatures above 580°C, suggesting the presence of minor titanohematite, but their remanence was entirely unblocked by 580°C during thermal demagnetization. The baked soil and upper lithoidal lithologies altered very little during heating, whereas a significant increase in susceptibility around 300-400°C is observed in the UBV and LL cooling curves. This susceptibility increase could be related to alteration of a pre-existing phase or an effect of cation disordering during heating (Bowles et al., 2013).

The ARM susceptibility along the core z-axis of all lithologies before and after heating to 680°C changed considerably (**Table 1).** Baked soil samples decreased consistently in ARM susceptibility by about 40%, whereas the ignimbrite samples increased on average by ~25%. The magnetization of samples from all lithologies was completely removed at less than 600°C during progressive thermal demagnetization. Samples from Zone LBV, however, differed from the rest in having only ~20% or less of their magnetization remaining after heating to 250°C, with all their magnetization removed by 450°C.

Hysteresis loops for most lithologies saturate in fields below 0.6 T, even for Zone LBV that exhibits lower Curie and unblocking temperatures **(Fig. 5).** Zone UBV samples have significantly greater coercivities and Mr/Ms ratios than the other lithologies, and their NRM intensities are also much higher (**Fig. 6**; **Tables 1 and 4**). This indicates that these samples have the largest percentage of single to pseudosingle domain grains [Parry 1965; Day 1977]. All three of these previously listed magnetic properties increase from the Zones LBV to UBV. Lower values in the LBV zone likely result from a larger abundance of even finer superparamagnetic grains, as was observed in the Tiva Canyon Tuff (Till et al., 2011). Zone LL has a similar coercivity to Zone UL, but with higher Mr/Ms ratios and NRM intensities. This trend likely

corresponds to an increasing percentage of larger magnetic grains in Zone UL zone due to the slower cooling of these units.

4.3 Magnetic Remanence and Anisotropy of TRM

Samples from Zone LBV behaved poorly and had somewhat different directions during thermal and AF demagnetization. The samples from this thin zone right at the base are weakly magnetized, and probably contain a combination of coarse-grained titanium-rich and very fine-grained titanium-poor magnetites, the latter is likely carrying most of the anisotropy. We suspect that gyroremanence in the latter may have contributed to the poor AF demagnetization behavior [Stephenson 1993] and titanomagnetite-to-magnetite alteration (oxyexsolution) during heating in the former caused the poor thermal demagnetization behavior. Samples from all other sub-lithologies yield linear trends to the origin in Zijderveld diagrams and better agreement between thermal and AF demagnetization techniques (**Table 2; Figs. 5 and 7**). A very small, normal, low-temperature (20-150°C or less) or low-coercivity component (all but one 0-10 mT or less) was common in all sub-lithologies. It could be a viscous overprint, mixed with some other secondary remanence since it is oriented somewhat east of the current field direction **(Table 2).**

The underlying baked soil has the most magnetically isotropic TRM (P_{ATRM}= 1.07-1.1) of all the sub-lithologies, and it has tightly clustered ChRM directions (**Tables 1 and 3**). Correcting for TRM anisotropy using the inverse of the ATRM tensor

(equation 2) only changes the mean direction by 0.8°, to D = 331.5 and I = 57.5 with a precision parameter k = 442 and confidence limit α_{95} = 2.6° (**Table 3**). We conclude, therefore, that this corrected mean direction of the baked soil faithfully represents the orientation of the paleofield during cooling. Remanence directions from the underlying fused and non-welded Brown's View Member and the fused ash fall match within error that of the baked soil (**Table 3**).

Samples from zone LBV are moderately anisotropic (P_{ATRM}= 1.29-1.67), whereas zone UBV samples have a large anisotropy (P_{ATRM}= 2.05-3.68) and decently clustered sample directions. The combined LBV and UBV mean direction is 26.4° from the ATRM-corrected baked soil (BS) mean (**Fig. 7; Table 3).** Samples from zone LL are moderately anisotropic (P_{ATRM}=1.23-1.67) with a mean magnetic direction that is 8.8° from that of the ATRM-corrected baked soil. Except for one discrepantly steep direction (LL22), samples, from zone LL are tightly clustered. Zone UL samples, collected much higher above the basal vitrophyre, have a low-to-moderate magnetic anisotropy (P_{ATRM} = 1.06-1.21) and a well-defined mean direction that is only 3.5° from that of the ATRM-corrected baked soil**.**

The zones with samples that have more discrepant magnetic directions are also characterized by larger coercivity, NRM magnetization, Mr/Mrs ratio and magnetic anisotropy (**Fig. 6**; **Table 1; 4**), indicating a higher proportion of fine, single-domain or pseudo-single-domain grains. Zones LBV, UBV, and LL have a maximum

magnetic susceptibility (K1) with northward dipping imbrication, suggesting flow to the south away from the Snake River Plain (**Fig. 9; Table 5) [**Incoronato et al., 1983; Knight et al., 1986]. Magnetic fabrics observed in samples collected from the upper, contorted portion of the ignimbrite (zones UL, UV, and OT) are more randomly oriented as a result of multiple generations of folding.

The directions of samples of UBV and LL, and to a lesser extent those of LBV, display inclinations shallower and declinations rotated clockwise relative to those of the baked soil (**Fig. 7a**). This is what one would expect from the nearly north-south orientation of the ATRM K1 axis and lineation and the nearly horizontal foliation (**Table 1**; **Fig. 9c and 9e**). Applying equation 2 to correct the ChRM directions of individual samples for ATRM improves the mean directions of all ignimbrite zones by moving them closer to the baked soil mean, but with varying degrees of success (**Fig. 7, Tables 1 and 3**). The mean from zone UL, already only 3.5° from the mean from the baked soil, moves just 0.8° closer. The LL mean moves 8.3 degrees closer, to a position only 0.5° from the mean from the baked soil. But the combined mean direction from zones LBV and UBV, which is the most discrepant, moves only one-third of the way to the baked soil mean.

The magnetic directions in the upper vitrophyre (zone UV) and upper fused ash (OT) have a mean direction that matches within error that of the baked soil, though with considerably more scatter than lithoidal samples (**Fig. 10, Table 3**). Samples from the

steeply-dipping limbs of rheomorphic folds and subhorizontal fold hinges fail the fold test (i.e. remanence directions are more scattered after bedding tilt corrections). Those collected from fold limbs with steeply dipping AMS fabrics (i.e., smaller inclinations of $K3_{ams}$) have steeper remanence directions, and those collected from hinges with shallowly dipping fabrics have shallow remanence directions, suggesting a causal relationship between anisotropy and deflection of remanence (**Fig. 10; Table 6**).

5. Discussion

5.1 Discrepant Magnetic Directions in Other Welded Ignimbrites

Problems with paleomagnetic studies of welded ignimbrites have long been observed, yet there is no consensus over which sub-lithologies are best for sampling and what mechanisms affected the magnetic directions. Similar to our study, correction for a large foliated ATRM and AARM carried by titanomagnetite significantly reduced the scatter of inclinations within some Sardinian ignimbrites [Gattacceca and Rochette 2002]. After the correction, however, the remanence directions were still streaked with a larger range of inclinations than declinations, suggesting that the correction may have only partly worked. In addition to ignimbrites, discrepant TRM directions have been observed in some rhyolitic lavas [Hoshi 2002; Singer and Brown 2002; Uno et. al., 2013] and attributed at least in part to flow structure (magnetic anisotropy).

Partial to complete remagnetization via low temperature oxidation in the upper parts of welded ignimbrite has been documented in several studies [Reynolds 1977; Ellwood et al., 1989; McIntosh 1991]. In the Huckleberry Ridge Tuff of Yellowstone, Reynolds [1977] inferred that low-temperature oxidation produced a normal-polarity chemical-remanent overprint (CRM) and a wide dispersion of directions in the more porous, weaker and less stably magnetized lithoidal lithology. The basal vitrophyre, however, yielded internally consistent, shallow reversed directions that agreed with those of included xenoliths and underlying baked sediment. Ellwood [1989] interpreted the reversed polarity that he observed in the top of the otherwise normally magnetized Fish Canyon Tuff of southern Colorado to result from alteration of magnetite to stable maghemite long after initial cooling.

In the ~100 m thick welded Peach Springs Tuff of southeast California, Wells and Hillhouse [1989] interpreted systematic variation of magnetic directions with height as the recording of secular variation during prolonged cooling. In a micro-analytical study of ignimbrites of the Yerington succession in Nevada, Geissman [1980] observed larger scattering and systematic offset in the magnetic directions of lithoidal compared to vitrophyre magnetic directions in sub-millimeter sized components (e.g., groundmass, crystals, lithics) that he ascribed to grain rotation below the blocking temperature. In contrast to the observations above of Geissman and Reynolds, Rosenbaum [1986] showed that the basal vitrophyre of the Tonapah Spring ignimbrite in southern Nevada has shallower magnetic directions than the lithoidal

center. He attributed the shallow vitrophyre directions to sub-blocking-temperature rotation during welding.

5.2 Discrepant Magnetic Directions in the Grey's Landing Ignimbrite

Rheomorphic shear strain indicated by a variety of features such as flow banding and rotated crystals increases with height in the basal vitrophyre [Andrews and Branney, 2011]. The very base of the ignimbrite quickly chilled against the substrate, thereby limiting crystallization of anisotropic fine-grained magnetite and inhibiting strain accumulation. ATRM jumps by a factor of 2.5 between the four samples closest to the base and the two just above (**Fig. 6a**), which is why we divide the basal vitrophyre there into lower (LBV) and upper (UBV) zones. Other parameters, however, such as NRM intensity, coercivity and Mr/Ms change more gradually (**Fig. 6**), and the two zones are difficult to distinguish in the field, so we combine the samples of the LBV and UBV for purposes of calculating the uncorrected and corrected lithology means in **Table 3**. Their mean direction differs by 26.4° from that of the ATRM corrected baked soil mean, shallower and somewhat clockwise rotated. Applying the inverse of the ATRM tensor measured for each sample to its characteristic remanent direction (**eq. 2**) corrects the mean remanence direction back closer to the paleofield orientation given by the baked soil, but only one-third of the way (**Fig. 7**). The incompleteness of this correction may be due to changes in the ATRM tensor during laboratory heating (**Table 1**), precipitation of magnetic grains below their blocking temperature, or to shallowing from another mechanism such as sub-blocking-temperature grain rotation.

Though less discrepant than the basal vitrophyre, the sample mean remanence direction from lower lithoidal zone LL is also shallower and clockwise rotated with respect to the baked soil direction. In this case the measured ATRM tensor does successfully correct the shallow remanence of LL, from 8.3° to within 0.5° of the baked soil direction. The effectiveness of this correction suggests that remanence anisotropy was the sole cause of the spurious shallowness. Lithoidal samples collected from zone UL (**Fig. 3**), are much less anisotropic on average than in the LL zone, and they have a steeper mean magnetic direction similar to that of the baked soil (**Figs. 7 & 8**). These samples also have a more randomly oriented magnetic fabric as a result of secondary folding (**Fig. 9; Table 5**) that is not correlated with the directions of remanence. This shows that late stage folding in the UL zone occurred above the unblocking temperatures of the constituent magnetic minerals, in agreement with recent observations from the Huckleberry Ridge Tuff in Yellowstone [Geissman et al., 2010] and the Nuraxi Tuff in Sardinia, Italy [Pioli et al., 2008]. In contrast to the observations of Wells and Hillhouse [1989] on the Peach Springs Tuff, the similarity of magnetic directions in the fastest cooled baked soil and slowest cooled UL zone indicates that the time-span of cooling was short compared to the rate of secular variation.

5.3 Origin of the Magnetic Fabric

Many factors may affect the development of magnetic anisotropy in ash-flow tuffs, such as rheomorphic and compaction strain, temperature, degree of welding, composition, thicknesses of the ignimbrite and of the basal vitrophyre, and height above the base (cooling time). The magnetic fabric likely resides mainly in elongate fine-grained magnetite that precipitates and grows at temperatures above 580°C [Geissman et al., 1983; Schlinger et al., 1988; Pioli et al., 2008; Gee et al., 2010]. Magnetic anisotropy develops from shear and compaction during emplacement, but may also form during continued grain growth or crystallization of new grains that inherit the pre-existing magnetic or silicate fabric, respectively, after emplacement [Wolff et al., 1989; Pioli et al., 2008]. The size, shape, and distribution of post-emplacement magnetite grains are likely controlled at least in part by the thermal history of the volcanic glass. The large variations we observe in magnetic behavior near the rapidly cooled ignimbrite base may result from the steep thermal gradient after emplacement and the dependence of magnetic properties on grain growth [Riehle 1973; Schlinger et al., 1991; McIntosh 1991; Pioli et al., 2008; Till et al., 2011].

Proportionately less fine-grained magnetite appears to have crystallized in the lowest, most quickly chilled part of zone LBV of the Grey's Landing ignimbrite compared to the rest of the BV. The magnetization in this zone has a more significant contribution from large multi-domain and mostly isotropic magmatic low-Fe titanomagnetite grains. This is illustrated by its low NRM and ATRM, large, low-unblocking and

low-Curie temperature phase, low remanent coercivity and low Mr/Ms compared to values for samples higher in the vitrophyre (**Tables 1, 2 and 4; Fig. 5 and 6**). Above this zone the post-emplacement, fine-grained magnetite dominates the magnetic properties. The degree of alignment, aspect ratio, magnetic domain state, and degree of interaction between fine-grained magnetite likely evolved with continued nucleation and growth. Even higher above the base, in the upper half of the UBV and continuing upward in the LL, NRM and TRM susceptibility, coercivity and intensity of ATRM generally decrease (**Fig. 6**), perhaps as grains grew larger by Ostwald ripening, absorbing the more coercive and anisotropic smaller grains. In addition, the distribution and form of magnetite crystals may have changed with height, as has been observed in some other ignimbrites, from homogenously dispersed magnetically non-interacting crystallites to heterogeneous clusters of intersecting and strongly interacting grains [Schlinger et al., 1988; Till et al., 2011]. Such a process in the lithoidal zone could have reduced an initially strong magnetic fabric that formed from shearing and compaction during emplacement. The successful ATRM correction of mean direction in the LL zone suggests that the evolution of magnetic fabric in the Grey's Landing ignimbrite was essentially complete before cooling below the remanence blocking temperatures, but this would not necessarily be true for all ignimbrite bodies.

5.4 AMS as a Proxy for ATRM?

It has long been recognized that remanence anisotropy is generally larger than susceptibility anisotropy in paleomagnetically relevant samples [Jackson, 1991]. This is very much the case for the Grey's Landing ignimbrite (**Table 1; Fig. 8**), and for this reason AMS is not suitable for evaluating and correcting deflection of remanence that results from its large ATRM. The oft-cited rule of thumb employing AMS to assess whether anisotropy could affect thermoremanent magnetization appreciably [e.g., Rosenbaum, 1986], namely that an AMS of at least 5% is required to cause a deflection in TRM direction of 3° [Stacey and Banerjee, 1974], fails spectacularly for the Grey's Landing ignimbrite. For example, the average AMS values for the basal vitrophyre (LBV+UBV) and LL zones are 5.74% and 2.9%, yet the resultant average remanence deflections are 26.4° and 8.8°, respectively (**Tables 1 and 3**). This is not surprising considering that the calculation on which the rule of thumb is based assumes a rock containing only multidomain grains [Stacey and Banerjee, 1974, p. 118-120]. Likewise, there is no direct relationship between P^2_{AMS} and P_{ATRM} (**Table 1**) such as was derived and observed by Cogné [1987] for TRM and susceptibility carried by multi-domain grains with shape anisotropy. However, the orientation of the AMS and ATRM principal axes agree well in the basal vitrophyre, and also well for the maximum principal axes in the LL zone. Thus the easier and more rapid AMS measurement may be just as effective in estimating flow direction. Despite the likely presence of single-domain grains in the glassy lithology, we don't observe inverting of K1 and K3 axes, probably because the ATRM resides predominantly in single-domain grains and the AMS in multidomain grains.

5.5 Recommendations for Sampling SR-Type Ignimbrites

We found that lithoidal samples taken in the chaotically folded lithoidal interior, the UL zone well above the highly sheared vitrophyre-lithoidal transition, are least anisotropic and yielded a site-mean direction statistically indistinguishable from the paleofield direction recorded in the baked soil. Moreover, for samples that are significantly anisotropic and chaotically folded, their variably oriented magnetic fabrics help randomize and average out the deflection of remanence directions. For our study this is best demonstrated by the upper vitrophyre UV, sampled at the top of the Grey's Landing ignimbrite in the section at Salmon Dam (**Fig. 1)**, where the averaging of a large range of deflections toward the variably dipping planes of maximum magnetic anisotropy results in a mean direction that agrees within error with that of the baked soil (**Fig. 10 and Table 3**). In contrast, anisotropic samples collected exclusively from the lower zones, with flat-lying flow banding and corresponding planes of maximum anisotropy, systematically shallowed the site mean direction. It is advisable to sample in the central lithoidal zone to avoid potential CRM overprinting near the top of the ignimbrite [Reynolds 1977; Ellwood et al., 1989].

6. Conclusions

We have observed that the strongly rheomorphic vitrophyre and lowermost lithoidal zones of several central Snake River Plain ignimbrites carry remanent magnetization

that is discrepantly shallow and sometimes rotated compared to that of the central lithoidal zone. In this contribution, we present a detailed paleomagnetic study of a vertical profile through one such unit, the Grey's Landing ignimbrite, which has the advantage of including an underlying baked soil that presumably carries a faithful record of the ancient field direction. We found large deflection of stable natural remanent direction as high as 38° accompanied by large anisotropy of thermoremanent magnetization (P_{ATRM}=3.33), in glassy samples that contain fine-grained magnetite with high Mr/Ms ratio, coercivity, TRM susceptibility and NRM intensity. The corresponding intensity of anisotropy of magnetic susceptibility was modest (P_{AMS}=1.053), providing no warning for such large deflection of TRM. These samples have a stronger fabric lineation than foliation, implying that rheomorphic shear strain was larger than compaction-related strain during emplacement, and thus had a greater effect on the magnetic direction. Anisotropy decreases with height above the vitrophyre in the lithoidal zone and so does deflection of the NRM, with the result that the upper lithoidal zone is a faithful paleomagnetic recorder and carries the same mean characteristic direction as the baked soil. This observation suggests either that slower cooling promoted devitrification accompanied by nucleation of new and continued growth of existing magnetic grains that reduced anisotropy prior to cooling below the remanence blocking temperatures, or that shearing was progressively less intense above the vitrophyre-lithoidal transition, or both. We therefore recommend that paleomagnetic studies of strongly welded ignimbrites such as those in the Snake River Plain preferentially target lithoidal lithologies in the chaotically folded zone. If

needed, the anisotropy of remanence rather than anisotropy of magnetic susceptibility should be measured and used to correct the remanence directions. Even though magnetic directions from the vitrophyre lithology may be stable and well clustered, they could still be systematically offset owing to strong anisotropy.

7. Acknowledgements

Some of the field and laboratory expenses for this work were covered by the Natural Environment Research Council (NERC) Grant NE/G005372/1. The salary and school fees for the first author were covered in part by a National Science Foundation NSF grant (EAR 1250444) awarded to X. Zhao. We also would like to thank Jordan Murphy, Francesca Spinardi, and Sophie Foster for assistance with laboratory and field work, and also thank Rachel Hohn and Zach Mayo for help in the field. Please contact the first author via email at dfinn@ucsc.edu for data requests and other questions.

8. References

Andrews, G. D. M., M. J. Branney, B. Bonnichsen, and M. McCurry (2008), Rhyolite ignimbrites in the Rogerson Graben, southern Snake River Plain volcanic province: Volcanic stratigraphy, eruption history and basin evolution: Bulletin of Volcanology, v. 70, p. 269–291, doi: 10.1007/s00445-007-0139-0.

Andrews G. D. M, and M. J. Branney (2011) Emplacement and rheomorphic deformation of a large, lava-like rhyolitic ignimbrite: Grey's Landing, southern Idaho. Geol Soc Am Bull 123:725–743. doi:10.1130/B30167.1

Bogue, S. W., and R. S. Coe (1981), Paleomagnetic correlation of Columbia River basalt flows using secular variation, J. Geophys. Res., 86, 11883-11897

Bonnichsen B, and G. P. Citron (1982) The Cougar Point Tuff, southwestern Idaho. In: Bonnichsen B, Breckenridge RM (eds) Cenozoic Geology of Idaho. Idaho Bur Mines Geol Bull 26:255–281

Bowles, J. A., Jackson, M. J., Berquó, T. S., Sølheid, P. A., & Gee, J. S. (2013). Inferred time-and temperature-dependent cation ordering in natural titanomagnetites. Nature Communications, 4, 1916 doi: 10.1038/ncomms2938.

Branney, M. J., B. Bonnichsen, G. D. M. Andrews, B. Ellis, T. L. Barry, and M. McCurry (2008), 'Snake River (SR)-type'volcanism at the Yellowstone hotspot track: distinctive products from unusual, high-temperature silicic super-eruptions. Bulletin of Volcanology, 70(3), 293-314.

Cathey H. E., B. P. Nash (2004), The Cougar Point Tuff: implications for thermochemical zonation and longevity of high-temperature, large volume silicic magmas of the Miocene Yellowstone hotspot. J Petrol 45:27–58

Choiniere, S. R., and D. A. Swanson (1979), Magnetostratigraphy and correlation of Miocene basalts of the northern Oregon coast and Columbia Plateau, southeast Washington, Am. J. Sci., 279, 755

Cogné, J. P. (1987). TRM deviations in anisotropic assemblages of multidomain magnetite. Geophysical Journal International, 91(3), 1013-1023.

Day, R., M. Fuller, and V. A. Schmidt (1977), Hysteresis properties of titanomagnetites: Grain size and composition dependence, Phys. Earth Planet. Inter., 13, 260 – 267.

Ellis, B. S., M. J. Branney, T. L. Barry, D. Barfod, I. Bindeman, J. A. Wolff, and B. Bonnichsen (2012), Geochemical correlation of three large-volume ignimbrites from the Yellowstone hotspot track, Idaho, USA. Bulletin of volcanology, 74(1), 261-277.

Ellwood, B. B., Stormer, J. C., & Whitney, J. A. (1989). Fish Canyon Tuff, Colorado: the problem of two magnetic polarities in a single tuff. Physics of the earth and planetary interiors, 56(3), 329-336.

Fisher, R.A (1953), Dispersion on a sphere: Royal Society of London Proceedings, v. 217, ser. A, p. 295–305.

Gattacceca, J., and P. Rochette (2002). Pseudopaleosecular variation due to remanence anisotropy in a pyroclastic flow succession. Geophysical research letters, 29(8), doi:10.1029/2002GL014697.

Gee, J. S., Y. Yu, and J. Bowles (2010), Paleointensity estimates from ignimbrites: An evaluation of the Bishop Tuff, Geochem. Geophys. Geosyst., 11, Q03010, doi:10.1029/2009GC002834.

Geissman J.W. (1980), Paleomagnetism of ash-flow tuffs: micro-analytical recognition of TRM components Geophys. Res., 85, pp. 1487–1499

Geissman, J. W., N. G. Newberry, and D. R. Peacor (1983). Discrete single-domain and pseudo-single-domain titanomagnetite particles in silicic glass of an ash-flow tuff. Canadian Journal of Earth Sciences, 20(2), 334-338.

Geissman, J. W., D. Holm, S. S. Harlan, and G. F. Embree (2010), Rapid, high-temperature formation of large-scale rheomorphic structures in the 2.06 Ma Huckleberry Ridge Tuff, Idaho, USA, Geology, 38, 263–266, doi:10.1130/ G30492.1.

Grommé, C. S., E. H. McKee, M. C. Blake Jr. (1972), Paleomagnetic correlations and potassium argon dating of middle Tertiary ashflow sheets in the eastern Great Basin, Nevada and Utah, Geol. Soc. Am. Bull., 83(6), 1619-1638

Hildreth, W., and G. A. Mahood (1985), Correlation of ash-Dow tuffs: Geological Society of America Bulletin, v. 96, p. 968-974.

Honjo N, B. Bonnichsen, W. P. Leeman, J. C. Stormer Jr. (1992), Mineralogy and geothermometry of high-temperature rhyolites from the central and western Snake River Plain. Bull Volcanol 54:220–237

Hoshi, H. (2002). Paleomagnetic direction of the Kumano acidic igneous rocks, Kii Peninsula, Japan. Bulletin-Geological Survey Japan, 53(1), 43-50.

Incoronato, A., F. T. Addison, D. H. Tarling, G. Nardi, and T. Pescatore (1983), Magnetic fabric investigations of pyroclastic deposits from Phlegrean Fields, southern Italy. Nature, 306, 461–463, doi:10.1038/306461a0.

Jackson, M. (1991). Anisotropy of magnetic remanence: a brief review of mineralogical sources, physical origins, and geological applications, and comparison with susceptibility anisotropy. Pure and Applied Geophysics, 136(1), 1-28.

Kirschvink, J. L. (1980), The least-squares line and plane and the analysis of paleomagnetic data. Geophysical Journal of the Royal Astronomical Society, 62, pp. 699 -7 18.

Knight, M. D., G. P. Walker, B. B. Ellwood, and J. F. Diehl (1986), Stratigraphy, paleomagnetism, and magnetic fabric of the Toba Tuffs: constraints on the sources and eruptive styles. Journal of Geophysical Research: Solid Earth (1978–2012), 91(B10), 10355-10382.

Lesti, C., M. Porreca, G. Giordano, M. Mattei, R. A. Cas, H. M. Wright, ... and J. Viramonte (2011). High-temperature emplacement of the Cerro Galán and Toconquis Group ignimbrites (Puna plateau, NW Argentina) determined by TRM analyses. Bulletin of volcanology, 73(10), 1535-1565.

McClelland, E., and P. S. Erwin (2003). Was a dacite dome implicated in the 9,500 BP collapse of Mt Ruapehu? A palaeomagnetic investigation. Bulletin of volcanology, 65(4), 294-305.

McIntosh, W. C. (1991). Evaluation of paleomagnetism as a correlation criterion for Mogollon-Datil Ignimbrites, southwestern New Mexico. Journal of Geophysical Research: Solid Earth (1978–2012), 96(B8), 13459-13483.

Morris, E.R., W. Schillinger, R. S. Coe, C. J. Pluhar, N. A. Jarboe (2009), Automating the 2G superconducting rock magnetometer for single-solenoid alternating field demagnetization. G-cubed, 10. doi:10.1029/2008GC002289.

Ort, M. H., S. L. de Silva, N. Jiménez C., B. R. Jicha, and B. S. Singer (2013), Correlation of ignimbrites using characteristic remanent magnetization and anisotropy of magnetic susceptibility, Central Andes, Bolivia, Geochem. Geophys. Geosyst., 14, 141–157, doi:10.1029/2012GC004276.

Parry, L. G. (1965). Magnetic properties of dispersed magnetite powders.Philosophical Magazine, 11(110), 303-312.

Perkins M.E., W. P. Nash, F. H. Brown, R. J. Fleck (1995) Fallout tuffs of Trapper Creek Idaho—a record of Miocene explosive volcanism in the Snake River Plains volcanic province. Geol Soc Amer Bull 07:1484–1506

Pierce, K.L., L. A. Morgan (1992), The track of the Yellowstone hotspot: volcanism, faulting, and uplift. In: Link, P.K., Kuntz, M.A., Platt, L.B. (eds.) Regional Geology of Eastern Idaho and Western Wyoming. Geological Society of America Memoir 179, 1–53.

Pierce, K. L., and L. A. Morgan (2009). Is the track of the Yellowstone hotspot driven by a deep mantle plume?—Review of volcanism, faulting, and uplift in light of new data. Journal of Volcanology and Geothermal Research, 188(1), 1-25.

Pioli, L., Lanza, R., Ort, M., and Rosi, M. (2008). Magnetic fabric, welding texture and strain fabric in the Nuraxi Tuff, Sardinia, Italy. Bulletin of Volcanology, 70(9), 1123-1137.

Piper, J. D. A., J. C. Stephen, and M. J. Branney (1997). Palaeomagnetism of the Borrowdale and Eycott volcanic groups, English Lake District: primary and secondary magnetization during a single late Ordovician polarity chron. Geological Magazine, 134(04), 481-506.

Piper, J. D. A., F. Koçbulut, H. Gürsoy, O. Tatar, L. Viereck, P. Lepetit, ... and Z. Akpınar (2013). Palaeomagnetism of the Cappadocian Volcanic Succession, Central Turkey: Major ignimbrite emplacement during two short (Miocene) episodes and Neogene tectonics of the Anatolian collage. Journal of Volcanology and Geothermal Research, 262, 47-67.

Reynolds, R. L. (1977), Paleomagnetism of the welded tuffs of the Yellowstone group, J. Geophys. Res.., 82, 3677-3693

Riehle, J. R. (1973). Calculated compaction profiles of rhyolitic ash-flow tuffs. Geological Society of America Bulletin, 84(7), 2193-2216.

Rosenbaum, J. G. (1986). Paleomagnetic directional dispersion produced by plastic deformation in a thick Miocene welded tuff, southern Nevada: Implications for welding temperatures. Journal of Geophysical Research: Solid Earth (1978–2012), 91(B12), 12817-12834.

Schlinger, C. M., J. G. Rosenbaum, and D. R. Veblen (1988). Fe-oxide microcrystals in welded tuff from southern Nevada: Origin of remanence carriers by precipitation in volcanic glass. Geology, 16(6), 556-559.

Schlinger, C. M., D. R. Veblen, and J. G. Rosenbaum (1991). Magnetism and magnetic mineralogy of ash flow tuffs from Yucca Mountain, Nevada. Journal of Geophysical Research: Solid Earth (1978–2012), 96(B4), 6035-6052.

Singer, B., and L. L. Brown (2002). The Santa Rosa Event:< sup> 40</sup> Ar/< sup> 39</sup> Ar and paleomagnetic results from the Valles rhyolite near Jaramillo Creek, Jemez Mountains, New Mexico. Earth and Planetary Science Letters, 197(1), 51-64.

Smith, R.B., L. W. Braile (1984), The Yellowstone hotspot. Journal of Volcanology and Geothermal Research, Volume 61, Issues 3–4, July 1994, Pages 121-129,

Speranza F., A. Di Chiara, and S. G. Rotolo (2012), Correlation of welded ignimbrites on Pantelleria (Strait of Sicily) using paleomagnetism, Bull. Volcanol., 74, 341–357, doi:10.1007/s00445-011-0521-9.

Stacey, F. D., & Banerjee, S. K. (1974). The physical properties of rock magnetism. Developments in Solid Earth Geophysics, 5.

Stacey, F. D., & Banerjee, S. K. (1974). The physical properties of rock magnetism. Developments in Solid Earth Geophysics, 5. Elsevier, Amsterdam, 195pp

Stephenson, A., S. Sadikun, and D. K. Potter (1986), A theoretical and experimental comparison of the anisotropies of magnetic susceptibility and remanence in rocks and minerals. Geophys. J. R. Astron. Sot., 84: 185-200

Stephenson, A. (1993). Three-axis static alternating field demagnetization of rocks and the identification of natural remanent magnetization, gyroremanent magnetization, and anisotropy. Journal of Geophysical Research: Solid Earth (1978–2012), 98(B1), 373-381.

Till, J. L., M. J. Jackson, J. G. Rosenbaum, and P. Solheid (2011). Magnetic properties in an ash flow tuff with continuous grain size variation: A natural reference for magnetic particle granulometry. Geochemistry, Geophysics, Geosystems, 12(7).

Uno, K., Y. Kaneshige, K. Furukawa, T. Shinmura, and M. Miyoshi (2013). Paleomagnetic investigation of rhyolite lava: Is rhyolite with clearly marked flow structure a high-fidelity geomagnetic field recorder?. Earth Planets Space,65(4), 331-336.

Uno, K., K. Furukawa, H. Ando, T. Shinmura, and M. Miyoshi (2014). Instantaneous record of the geomagnetic field direction of various facies from pyroclastic flow

deposits: Tests for consistency in paleomagnetic directions. Physics of the Earth and Planetary Interiors.

Wells, R. E., and J. W. Hillhouse (1989), Paleomagnetism and tectonic rotation of the lower Miocene Peach Springs Tuff, Colorado Plateau, Arizona to Barstow, California: Geological Society of America Bulletin, v. 101, p. 846-863

Wolff, J. A., B. B. Ellwood, and S. D. Sachs (1989). Anisotropy of magnetic susceptibility in welded tuffs: application to a welded-tuff dyke in the Tertiary Trans-Pecos Texas volcanic province, USA. Bulletin of volcanology, 51(4), 299-310.

9. Table Captions

Table 1: Magnetic Anisotropy and Remanence Data

Data are shown for baked soil (BS1-BS8), lower basal vitrophyre (LBV9-LV11), upper basal vitrophyre (UBV12-UV17), lower transitional lithoidal (LL18-LL22), and upper lithoidal (UL23-UL31) Grey's Landing ignimbrite samples. The table includes the anisotropy (P), lineation (L) and foliation (F) from the thermoremanent (ATRM) and low-field susceptibility (AMS) anisotropy ellipsoids, the intensity of natural remanent magnetization (NRM) and the direction (DEC and INC) of characteristic remanence (ChRM) directions (see Table 2 for details), ATRM corrected ChRM directions, the angle between the uncorrected sample mean and corrected baked soil mean remanence directions (ϕ), average percent errors between

theoretically identical off-diagonal elements of the ATRM tensor over the average TRM values, ratios of the ARM susceptibility in the core Z direction after heating to 680° to the value measured prior to heating. (See text for P, L, F, and % Error equations), and the height in centimeters the core was taken above the base of the lower vitrophyre.

Table 2: Alternating Field and Thermal Demagnetization Results

Sample remanence data are shown for the baked soil (BS1-8), lower basal vitrophyre (LV9-11), upper basal vitrophyre (UBV12-17), lower transitional lithoidal (LL18-22), and lithoidal (UL23-31). N/D/I/MAD are number of points used/declination/inclination/maximum angular deviation for best-fit line as determined by principal component analysis [Kirschvink, 1982]. In the column containing step range, alternating magnetic field values are in units of milliTesla and temperature is in units of degrees Celsius. Sample directions with an '*' in front of their ID are not used in any analysis and are only meant to compare AF and thermal demagnetization techniques.

Table 3: Lithology Mean Remanence Directions

Mean directions (*in situ* coordinates) are shown for the unfused Browns View member (UBM), fused Browns View member (FBM), baked soil (BS), fused ash fall (FAF), basal vitrophyre (BV=UBV+LBV), lower transitional lithoidal (LL), lithoidal (UL), upper vitrophyre (UV), and upper fused orange tuff (OT) lithologies, with number of samples (N), declination (D), inclination (I), precision parameter (k), 95% confidence circle radius (a95), and angle made with the ATRM corrected baked soil

mean direction (ϕ). UBM, FBM, and FAF remanence directions match that of the baked soil within error. They are shown here for completeness, but are not discussed in detail in the paper.

Table 4: Hysteresis Parameters

Coercivity (Hc), remanent coercivity (Hcr), magnetic saturation (Ms), and magnetic remanence (Mr) are shown along with their ratios for the Grey's Landing ignimbrite.

Table 5: Anisotropy Tensor Directional Data

The eigenvectors (K1-K3) of the tensors describing the anisotropy of thermal remanent magnetization (ATRM) and low field induced magnetization (AMS) are shown for the Grey's Landing ignimbrite.

Table 6: Upper Vitrophyre and Orange Ash Remanence and AMS Data

Sample remanence directional data are shown for the upper vitrophyre (UV) and overlying orange tuff (OT). The lineation (L), foliation (F), and anisotropy (P), and eigenvectors (K1-K3) of the tensors describing the low field induced susceptibility ellipse (AMS) are also shown.

10. Figure Captions

Figure 1: Simplified geologic map of southern Idaho showing the northeastward progressing Yellowstone Hotspot Track and the trailing succession of calderas, bimodal rhyolitic to basaltic volcanism, and crustal deformation. The location of the

Rogerson Graben is shown in the white box, as well as the inferred eruptive centers shown with dashed circles: Bruneau-Jarbidge (BJ), Twin Falls (TF), and the Yellowstone caldera (Y). (Figure modified from Andrews et al., 2011)

Figure 2: Two examples of shallow paleomagnetic directions in the vitrophyre compared to the upper lithoidal zone. Squares and diamonds indicate vitrophyre (V) and upper lithoidal (UL) mean directions, respectively, and n represents the number of samples. All plots are lower hemisphere.

Figure 3: Graphic log of the Grey's Landing ignimbrite, including top of the Brown's View Member [unfused & fused ash flow (UBM & FBM) and baked soil (BS)] and the Grey's Landing Member fused ash fall (FAF), lower basal vitrophyre (LBV), upper basal vitrophyre (UBV), lower lithoidal (LL), upper lithoidal (UL), upper vitrophyre (UV), and upper orange tuff (OT) lithologies. The upper vitrophyre and ash fall have been eroded away. Two structural domains are observed, a lower, flat domain with sub-horizontal planar fabrics and intrafolial isoclinal (F1) folds, and an upper, contorted zone, in which early F1 folds are refolded and the fabrics vary from horizontal to steep. Sampling locations are indicated by arrows on the stratigraphic log. (Figure modified from Andrews et al., 2011)

Figure 4: Shaded relief and fault map of the Rogerson Graben showing the sampling locations. Red star: vertical profile through the Grey's Landing Ignimbrite from the underlying thermal contact zone to upper lithoidal (Lat.\Long.= 42°4'5"\114°45'45"). Blue circle: upper vitrophyre sampling location at Salmon Dam (Lat.\Long.= 42°12'42"\114°44'6"). Figure 1 shows the location of this map as an inset.

Figure 5: Typical zjiderveld diagrams of thermal and alternating magnetic field demagnetizations of samples from Grey's Landing ignimbrite together with their associated normalized decay of magnetization, temperature susceptibility curves measured in argon, and hysteresis loops, are shown for the baked soil (BS), lower basal vitrophyre (LBV), upper rheomorphic basal vitrophyre (UBV), lower transitional lithoidal (LL), and lithoidal (UL) zones.

Figure 6. Systematic changes of magnetic parameters as a function of height above base. Plots show ATRM anisotropy, remanence inclination, normalized ATRM susceptibility, NRM intensity, coercivity, and the ratio of magnetic remanence to magnetic saturation (Mr/Ms) versus height (centimeters) above the base of the Grey's Landing ignimbrite. The ATRM corrected baked soil remanence inclination is indicated by a dashed red line in Figure 6b.

Figure 7: Lower hemisphere stereographic plot of individual sample (a,b) and lithology mean (c,d) directions before and after correcting using the measured ATRM tensor. The vitrophyre sample direction from plot 'a' with an 'X' in the symbol lost its orientation before the anisotropy of thermal remanence measurements and does not have a corrected direction in plot 'b'. The size of samples in plots 'a' and 'b' indicates the intensity of anisotropy (P).

Figure 8: Systematics of anisotropy parameters—ATRM vs. AMS. (a) and (b): Note the excellent correlation of stronger ATRM (P) with shallow inclination, much better than that shown by AMS. (c) and (d): Note that the more anisotropic samples show much stronger lineation (L) than foliation (F) for ATRM, whereas the opposite is true

for AMS. Sample LBV9 has an overprinted remanence direction and is only seen in plots ‘c’ and ‘d’.

Figure 9: Systematics of anisotropy eigenvectors—ATRM vs. AMS. Maximum (K1, blue squares), intermediate (K2, green triangles), and minimum (K3, pink circles) susceptibility directions are shown for baked soil (BS), upper and lower basal vitrophyre (BV), lower lithoidal (LL), and upper lithoidal (UL). Symbols are labeled by the number segment of their sample name. All directions are plotted on the lower hemisphere.

Figure 10: $K3_{AMS}$ inclination vs. TRM inclination. Folding preceded TRM acquisition, so the systematic dependence of TRM direction on orientation of magnetic fabric is because anisotropy has caused major deflections of remanence (see text). Dashed line represents inclination of the baked soil. Because the deflections largely averaged out, the mean directions of the upper vitrophyre (UV) and orange tuff (OT) correspond well with the ancient field direction (Table 3).

Table 1. Magnetic Anisotropy and Remanence Correction

	Height	ATRM			AMS			NRM	ChRM		Cor. ChRM			Non-Diag.	ARM
Sample	(meters)	P	L	F	P	L	F	(A/m)	DEC	INC	Dec	Inc	ϕ (deg)	% Error	680°/20°
BS1		1.10	1.03	1.06	1.013	1.001	1.012	1.1	335	57	335	58	1	11	0.6
BS2		1.09	1.04	1.05	1.013	1.001	1.012	1.5	335	53	336	55	4	9	0.5
BS3		1.10	1.05	1.05	1.015	1.000	1.014	2.9	328	61	325	62	6	5	0.6
BS4		1.10	1.03	1.07	1.012	1.001	1.011	1.7	337	59	337	60	3	7	0.6
BS5		1.07	1.02	1.06	1.015	1.001	1.014	1.4	335	56	335	56	1	4	
BS6		1.09	1.02	1.07	1.015	1.001	1.014	2.3	328	57	327	58	5	7	
BS7		1.11	1.04	1.06	1.015	1.001	1.014	2.3	330	55	332	54	4	3	
BS8		1.10	1.03	1.07	1.015	1.001	1.015	2.2	325	56	324	57	7	5	
LBV9	.11	1.29	1.11	1.16	1.081	1.017	1.063	0.1	29	57	22	62	29	9	2.0
LBV10	.16	1.39	1.09	1.28	1.060	1.016	1.043	0.1	340	49	337	58	8	4	
LBV11	.24	1.35	1.07	1.26	1.053	1.002	1.051	6.2	338	53	331	60	3	6	1.4
LBV12	.38	1.67	1.34	1.25	1.053	1.010	1.042	10.0	358	33	356	45	27	8	
UBV13	.53	3.68	2.54	1.45	1.038	1.027	1.010	24.8	355	22	4	30	37	39	1.3
UBV14	.56	3.33	1.98	1.68	1.053	1.017	1.036	22.9	350	20	354	26	38	14	
UBV15	.76	2.26	1.43	1.57	1.076	1.026	1.049	23.4	343	33	327	45	24	32	1.2
UBV16	.80	2.40	2.14	1.13	1.064	1.023	1.040	21.0	348	24	335	29	34	6	
UBV17	.91	2.05	1.47	1.39	1.038	1.008	1.031	17.3	0	32			29	12	1.0
LL18	1.14	1.66	1.41	1.17	1.030	1.018	1.011	3.7	346	47	331	58	11	7	
LL19	1.42	1.60	1.35	1.18	1.044	1.020	1.023	3.6	347	47	335	57	12	19	
LL20	1.64	1.47	1.38	1.06	1.036	1.023	1.013	2.0	352	45	338	52	14	3	
LL21	2.11	1.23	1.13	1.08	1.014	1.007	1.007	1.4	344	51	338	52	7	9	
LL22	2.61	1.40	1.23	1.14	1.019	1.014	1.006	1.3	322	66	302	69	14	22	
UL23	~30	1.15	1.05	1.10	1.008	1.004	1.004	1.4	334	61	334	60	5	8	1.1
UL24	~30	1.15	1.02	1.13	1.009	1.005	1.004	1.3	352	63	354	62	9	8	1.4
UL25	~30	1.12	1.05	1.07	1.015	1.008	1.006	0.9	338	61	336	58	5	7	1.0
UL26	~30	1.17	1.06	1.10	1.006	1.002	1.004	1.0	325	51	326	47	9	13	0.5
UL27	~60	1.16	1.04	1.11	1.036	1.032	1.003	0.7	320	50	319	53	12	5	
UL28	~60	1.15	1.08	1.06	1.049	1.024	1.025	0.6	331	69	336	69	13	8	
UL29	~60	1.12	1.03	1.09	1.022	1.012	1.010	0.6	346	64	341	63	9	8	1.4
UL30	~60	1.06	1.04	1.01	1.038	1.019	1.019	2.6	313	61	314	61	13	10	0.9
UL31	~60	1.21	1.13	1.07	1.038	1.008	1.031	0.4	328	66	337	65	10	7	1.5

Table 2. Alternating Field and Thermal Demagnetization Results

Stable Component							Overprint			
ID	Procedure	STEP RANGE	N	Dg	Ig	MAD	STEP RANGE	N	Dg	Ig
BS1	AF	20-199 mT	7	335	57	0.9				
BS2	AF	20-199 mT	6	335	53	0.7	NRM-10 mT	2	45	47
BS3	AF	20-199 mT	6	328	61	0.5	NRM-10 mT	2	47	53
BS4	AF	20-199 mT	6	337	59	0.5	NRM-10 mT	2	29	56
BS5	Thermal	200-565 °C	12	335	56	1.4	NRM-100 °C	2	99	31
*BS5-b	AF	20-90 mT	9	329	59	0.6				
BS6	Thermal	150-565 °C	13	328	57	1.4	NRM-100 °C	2	55	16
BS7	Thermal	250-565 °C	11	330	55	1.2	NRM-100 °C	2	87	75
BS8	Thermal	150-565 °C	13	325	56	1	NRM-150 °C	2	39	55
*BS8-b	AF	20-199 mT	6	321	56	0.7				
LBV9	AF						NRM-20 mT	3	29	57
LBV10	Thermal	150-400 °C	6	340	49	8.2	NRM-100 °C	2	49	56
LBV10-b	AF	30-199 mT	6	337	35	7.3	NRM-15 mT	2	41	56
LBV11	AF	10-150 mT	5	338	53	0.9	NRM-5 mT	2	60	64
LBV12	AF	40-180 mT	6	358	33	0.8				
UBV13	AF	10-199 mT	7	355	22	0.4	NRM-10 mT	2	17	43
UBV14	Thermal	200-565 °C	13	350	20	1.4				
UBV14-b	AF	60-199 mT	5	348	24	0.5				
UBV15	AF	NRM-199 mT	7	343	33	1.3				
UBV16	Thermal	150-575 °C	14	348	24	2				
UBV16-b	AF	90-199 mT	4	352	28	1.6				
UBV17	AF	NRM-199 mT	7	0	32	1				
LL18	Thermal	NRM-565 °C	17	346	47	1.1				
LL19	Thermal	200-565 °C	13	347	47	2.2	NRM-100 °C	2	32	38
LL20	Thermal	150-605 °C	16	352	45	2.1	NRM-100 °C	2	42	57
LL21	Thermal	150-605 °C	16	344	51	1.8	NRM-100 °C	2	26	48
LL22	Thermal	475-595 °C	8	322	66	1.1				
UL23	AF	3-199 mT	16	334	61	1.4	NRM-3 mT	2	358	65
UL24	AF	8-199 mT	9	352	63	0.4	NRM-4 mT	2	24	74
UL25	AF	8-150 mT	11	338	61	0.4	NRM-4 mT	2	46	56
UL26	AF	8-199 mT	12	325	51	0.5	NRM-4 mT	2	50	61
UL27	AF	30-199 mT	5	320	50	1.3				
UL28	AF	40-180 mT	6	331	69	0.7				
UL29	AF	4-199 mT	10	346	64	0.7	NRM-4 mT	2	49	46
UL30	AF	90-199 mT	3	313	61	1.5	NRM-4 mT	2	287	45
UL31	AF	30-199 mT	5	328	66	1.3	NRM-8 mT	3	15	-80

Table 3. Lithology Mean Remanence Directions

Samples		Uncorrected lithology means					ATRM corrected lithology means				
Type	N	D	I	k	a95	ϕ (deg)	D	I	k	a95	ϕ (deg)
UBM	3	332.0	60.6	206.5	8.6	2.2					
FBM	4	320.0	58.2	77.5	10.5	8.3					
BS	8	331.6	56.7	551.6	2.4	0.8	331.6	57.5	442.1	2.6	0.0
FAF	3	344.6	60.9	51.8	17.3	4.6					
BV	7	348.2	33.6	30.9	11.0	26.4	344.9	42.7	21.5	13.3	17.0
LL	5	343.4	51.9	49.5	11.0	8.8	331.3	58.0	66.4	9.5	0.5
UL	9	331.0	61.0	90.1	5.5	3.5	332.0	60.2	84.1	5.6	2.7
UV	15	331.6	59.8	22.0	8.3	2.3					
OT	10	348.0	57.8	50.0	6.9	7.0					

Table 4. Hysteresis Parameters

Sample	Height (meters)	Hc (mT)	Hcr (mT)	Ms (μAm2)	Mr (μAm2)	Hcr/Hc	Mr/Ms
BS1		17.04	47.33	274.30	78.46	2.78	0.29
BS2		17.61	39.21	380.30	112.50	2.23	0.30
BS3		16.02	36.28	440.40	127.50	2.26	0.29
BS4		17.82	39.68	335.20	104.10	2.23	0.31
BS5		12.43	36.36	189.00	58.83	2.93	0.31
BS6		14.07	38.07	270.70	89.20	2.71	0.33
BS7		12.42	34.68	311.70	95.20	2.79	0.31
BS8		13.73	35.61	295.20	96.96	2.59	0.33
LBV9	.11	4.96	11.93	704.10	78.42	2.41	0.11
LBV10	.16	10.96	19.08	378.60	107.80	1.74	0.28
LBV11	.24	36.57	84.12	628.90	201.60	2.30	0.32
LBV12	.38	40.08	84.80	601.20	211.90	2.12	0.35
UBV13	.53	44.08	87.06	519.90	206.90	1.98	0.40
UBV14	.56	46.66	93.39	474.70	229.00	2.00	0.48
UBV15	.76	27.61	65.35	911.10	247.60	2.37	0.27
UBV16	.80	44.98	78.83	475.80	252.50	1.75	0.53
UBV17	.91	40.08	84.80	601.20	211.90	2.12	0.35
LL18	1.14	28.90	55.96	873.70	309.20	1.94	0.35
LL19	1.42	18.81	42.67	625.60	197.80	2.27	0.32
LL20	1.64	24.68	53.69	665.70	213.40	2.18	0.32
LL21	2.11	18.15	34.90	531.50	165.00	1.92	0.31
LL22	2.61	17.30	40.58	371.80	123.00	2.35	0.33
UL23	~30	12.79	25.98	540.60	115.70	2.03	0.21
UL24	~30	23.40	48.84	458.40	114.60	2.09	0.25
UL25	~30	19.31	40.27	492.60	107.90	2.09	0.22
UL26	~30	19.38	41.56	591.50	175.50	2.14	0.30
UL27	~60	22.52	54.53	279.50	49.98	2.42	0.18
UL28	~60	25.86	57.69	210.20	52.94	2.23	0.25
UL29	~60	24.04	57.10	228.40	49.79	2.38	0.22
UL30	~60	23.57	55.84	172.40	44.75	2.37	0.26
UL31	~60	21.01	51.80	253.20	48.13	2.47	0.19

Table 5. Anisotropy Tensor Directional Data

	ATRM						AMS					
Sample	K1dec	K1inc	K2dec	K2inc	K3dec	K3inc	K1dec	K1inc	K2dec	K2inc	K3dec	K3inc
BS1	148	11	337	79	238	2	302	6	212	2	108	84
BS2	343	7	246	45	80	44	330	1	240	4	75	86
BS3	343	15	107	65	248	20	263	3	354	9	153	81
BS4	318	9	75	71	226	17	336	6	66	2	175	83
BS5	249	27	12	47	141	30	134	3	44	2	289	87
BS6	47	15	305	36	156	50	285	2	15	3	164	87
BS7	245	31	6	40	130	34	101	1	192	3	349	87
BS8	82	12	340	45	184	43	49	3	319	0	226	87
LBV9	55	10	323	10	187	76	142	30	47	9	302	59
LBV10	348	3	79	6	229	83	357	13	267	1	171	77
LBV11	31	14	121	0	213	76	74	9	341	18	190	70
LBV12	7	12	274	10	147	74	218	2	308	3	96	87
UBV13	349	17	91	33	236	52	91	4	1	4	225	85
UBV14	346	16	80	16	213	67	89	2	358	7	191	83
UBV15	355	21	98	28	234	53	7	11	276	5	161	78
UBV16	0	19	269	2	173	71	23	7	113	4	235	82
UBV17							294	4	204	4	67	84
LL18	9	17	102	9	220	70	13	11	103	2	204	79
LL19	16	12	286	2	186	78	190	1	99	19	284	72
LL20	22	12	124	42	280	45	18	9	108	3	217	81
LL21	201	9	93	65	295	24	8	7	99	9	239	79
LL22	3	30	208	57	100	11	4	18	97	8	211	70
UL23	172	71	337	18	68	5	87	22	354	9	243	66
UL24	21	89	155	1	245	1	358	1	254	88	88	2
UL25	66	72	230	17	321	5	318	7	91	80	227	7
UL26	195	68	59	16	325	15	283	2	13	2	150	87
UL27	83	15	175	7	288	74	43	14	138	20	280	65
UL28	229	29	346	40	114	37	356	65	235	14	139	21
UL29	192	21	78	47	298	36	23	16	209	74	114	2
UL30	160	16	264	40	54	46	229	69	126	5	34	20
UL31	230	45	344	22	91	37	321	22	192	57	61	23

Table 6. Upper Vitrophyre and Orange Ash Remanence and AMS Data

	Remanence Directions					Anisotropy of Magnetic Susceptibility								
Sample	AF Range	N	Dec	Inc	MAD	L	F	P	K1dec	K1inc	K2dec	K2inc	K3dec	K3inc
UV32	0-199	7	316	74	1.1	1.028	1.040	1.069	299	85	209	0	119	5
UV33	0-199	6	312	70	2.5	1.050	1.030	1.081	228	28	27	61	133	9
UV34	0-199	6	330	28	0.9	1.023	1.026	1.050	242	8	333	7	105	79
UV35	0-199	6	320	74	1.6	1.023	1.084	1.108	75	5	329	73	166	16
UV36	0-199	6	295	68	3.3	1.027	1.040	1.068	240	41	85	46	342	13
UV37	0-199	6	332	75	2.2	1.029	1.078	1.109	131	53	270	29	12	20
UV38	0-199	6	24	67	2.2	1.017	1.056	1.074	77	25	195	46	328	34
UV39	0-199	6	1	62	1.2	1.027	1.011	1.038	45	43	174	34	285	29
UV40	0-199	6	323	42	0.9	1.011	1.034	1.046	244	8	154	1	60	82
UV41	0-120	5	336	46	0.9	1.024	1.037	1.062	18	4	288	6	141	83
UV42	25-199	5	348	46	1.2	1.016	1.053	1.070	56	21	323	8	214	67
UV43	0-199	8	333	55	1.7	1.022	1.025	1.047	319	41	108	45	214	16
OT44	0-199	6	338	52	0.6	1.006	1.002	1.008	206	30	315	29	80	46
OT45	0-199	4	330	54	0.7	1.007	1.003	1.010	197	27	303	28	71	50
OT46	0-199	6	338	55	0.5	1.006	1.005	1.011	303	48	71	29	178	27
OT47	0-199	5	329	59	1.0	1.008	1.009	1.017	271	49	142	29	36	27
OT48	0-120	4	331	65	0.7	1.023	1.045	1.069	326	64	214	10	119	23
OT49	50-120	3	15	56	1.4	1.009	1.016	1.025	74	24	185	38	320	42
OT50	25-120	4	6	60	0.5	1.007	1.017	1.024	95	38	204	23	318	43
OT51	25-120	4	359	45	1.0	1.009	1.017	1.027	224	2	133	22	320	68

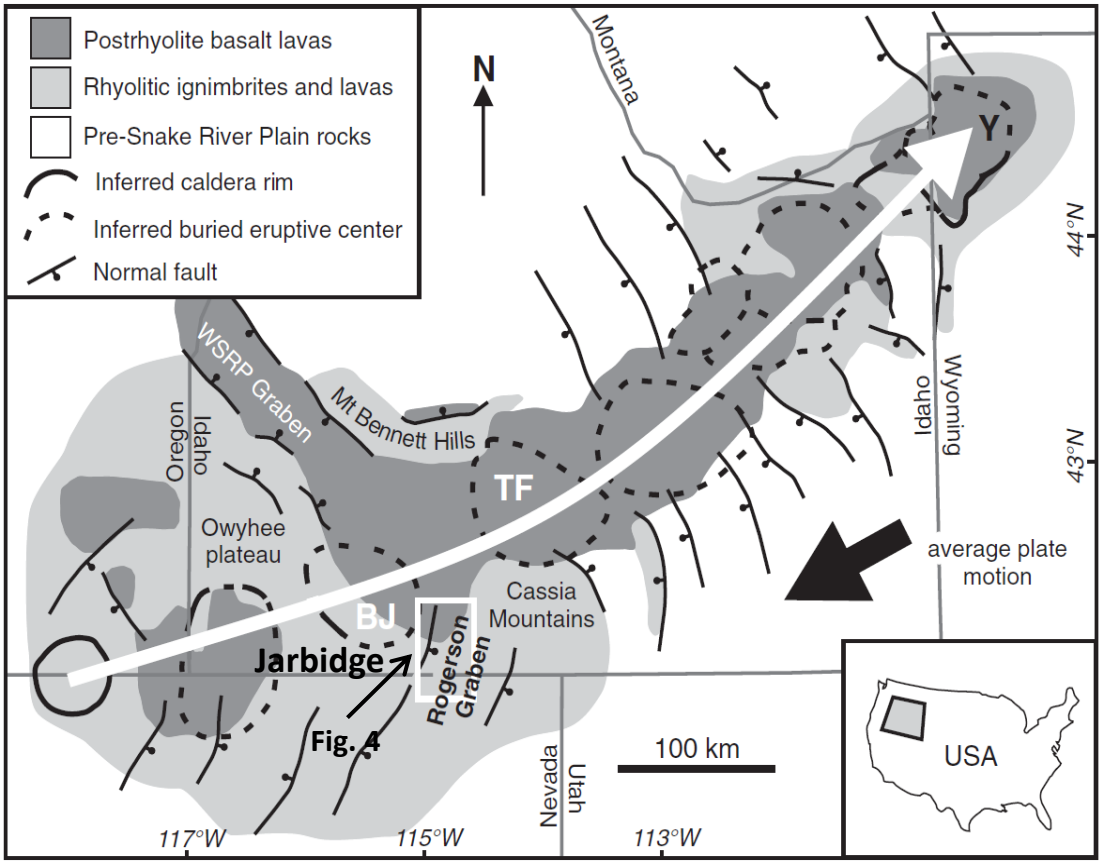

Figure 1: Simplified geologic map of southern Idaho showing the northeastward progressing Yellowstone Hotspot Track and the trailing succession of calderas, bimodal rhyolitic to basaltic volcanism, and crustal deformation. The location of the Rogerson Graben is shown in the white box, as well as the inferred eruptive centers shown with dashed circles: Bruneau-Jarbidge (BJ), Twin Falls (TF), and the Yellowstone caldera (Y). (Figure modified from Andrews et al., 2011)

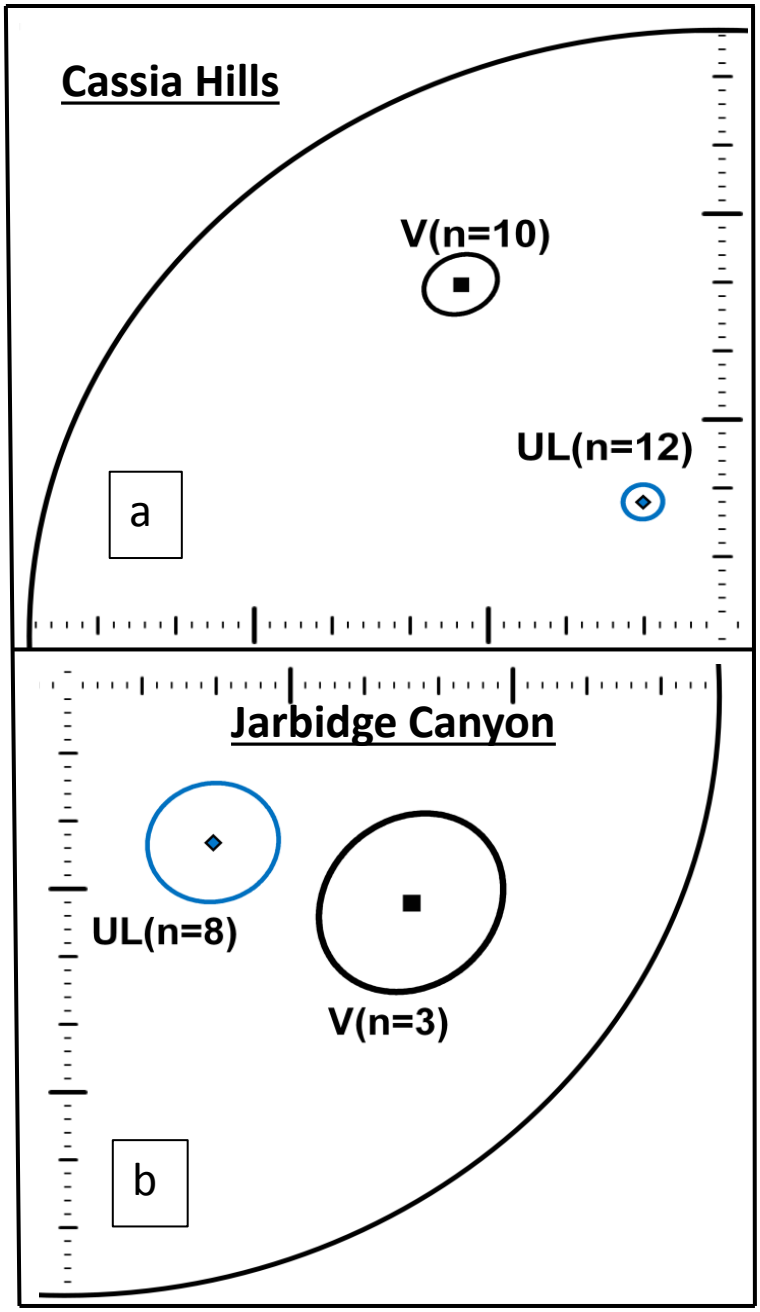

Figure 2: Two examples of shallow paleomagnetic directions in the vitrophyre compared to the upper lithoidal zone. Squares and diamonds indicate vitrophyre (V) and upper lithoidal (UL) mean directions, respectively, and n represents the number of samples. All plots are lower hemisphere.

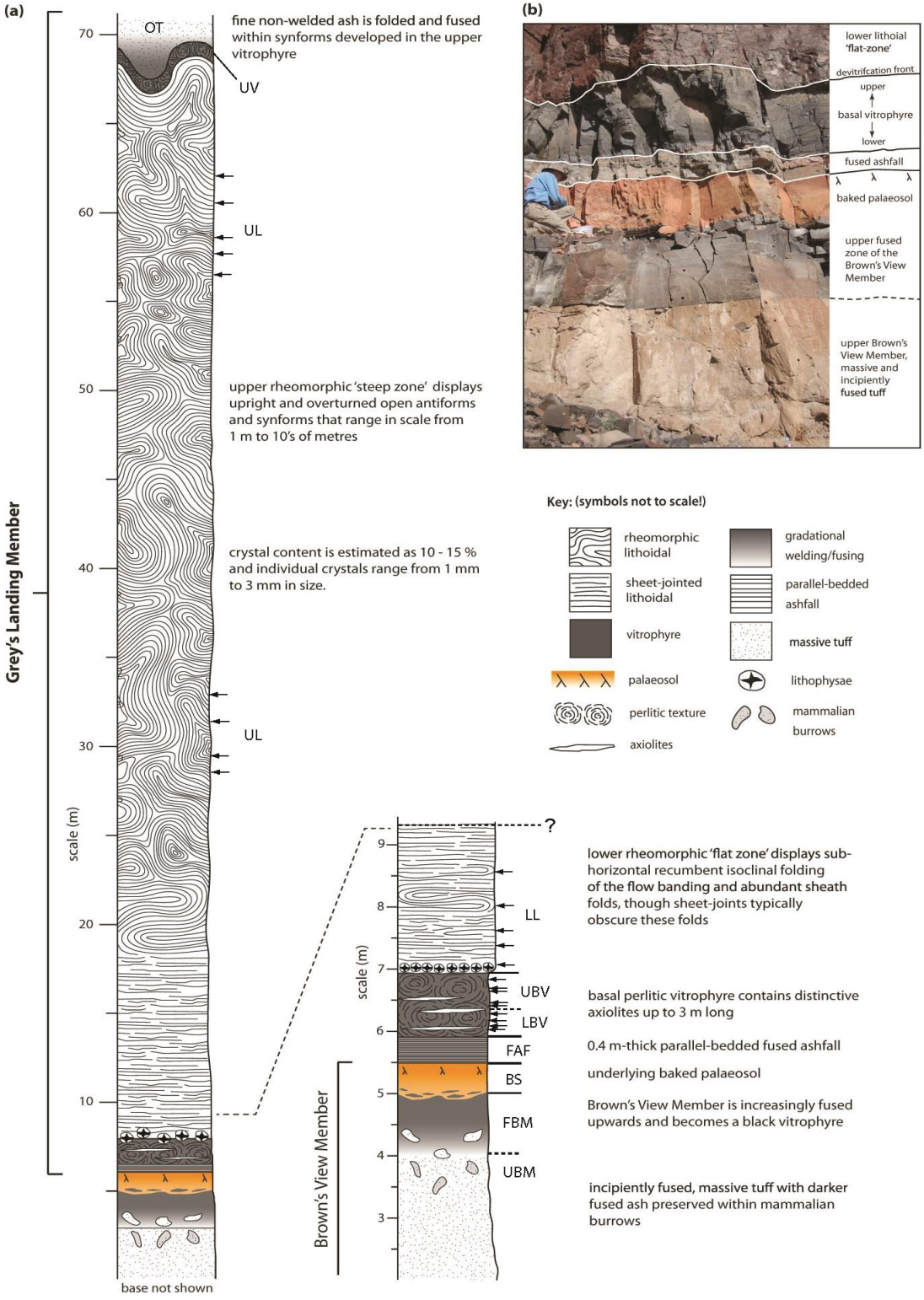
(a)
Grey's Landing Member
scale (m)
70
60
50
40
30
20
10
OT
UV
UL
UL
fine non-welded ash is folded and fused within synforms developed in the upper vitrophyre
upper rheomorphic 'steep zone' displays upright and overturned open antiforms and synforms that range in scale from 1 m to 10's of metres
crystal content is estimated as 10 - 15 % and individual crystals range from 1 mm to 3 mm in size.
base not shown
?
9
8
7
6
5
4
3
LL
UBV
LBV
FAF
BS
FBM
UBM
Brown's View Member
lower rheomorphic 'flat zone' displays sub-horizontal recumbent isoclinal folding of the flow banding and abundant sheath folds, though sheet-joints typically obscure these folds
basal perlitic vitrophyre contains distinctive axiolites up to 3 m long
0.4 m-thick parallel-bedded fused ashfall
underlying baked palaeosol
Brown's View Member is increasingly fused upwards and becomes a black vitrophyre
incipiently fused, massive tuff with darker fused ash preserved within mammalian burrows
(b)
lower lithoial 'flat-zone'
devitrifcation front
upper
basal vitrophyre
lower
fused ashfall
baked palaeosol
upper fused zone of the Brown's View Member
upper Brown's View Member, massive and incipiently fused tuff
Key: (symbols not to scale!)
rheomorphic lithoidal
sheet-jointed lithoidal
vitrophyre
palaeosol
perlitic texture
axiolites
gradational welding/fusing
parallel-bedded ashfall
massive tuff
lithophysae
mammalian burrows

Figure 3: (Previous page) Graphic log of the Grey's Landing ignimbrite, including top of the Brown's View Member [unfused & fused ash flow (UBM & FBM) and baked soil (BS)] and the Grey's Landing Member fused ash fall (FAF), lower basal vitrophyre (LBV), upper basal vitrophyre (UBV), lower lithoidal (LL), upper lithoidal (UL), upper vitrophyre (UV), and upper orange tuff (OT) lithologies. The upper vitrophyre and ash fall have been eroded away. Two structural domains are observed, a lower, flat domain with sub-horizontal planar fabrics and intrafolial isoclinal (F1) folds, and an upper, contorted zone, in which early F1 folds are refolded and the fabrics vary from horizontal to steep. Sampling locations are indicated by arrows on the stratigraphic log. (Figure modified from Andrews et al., 2011)

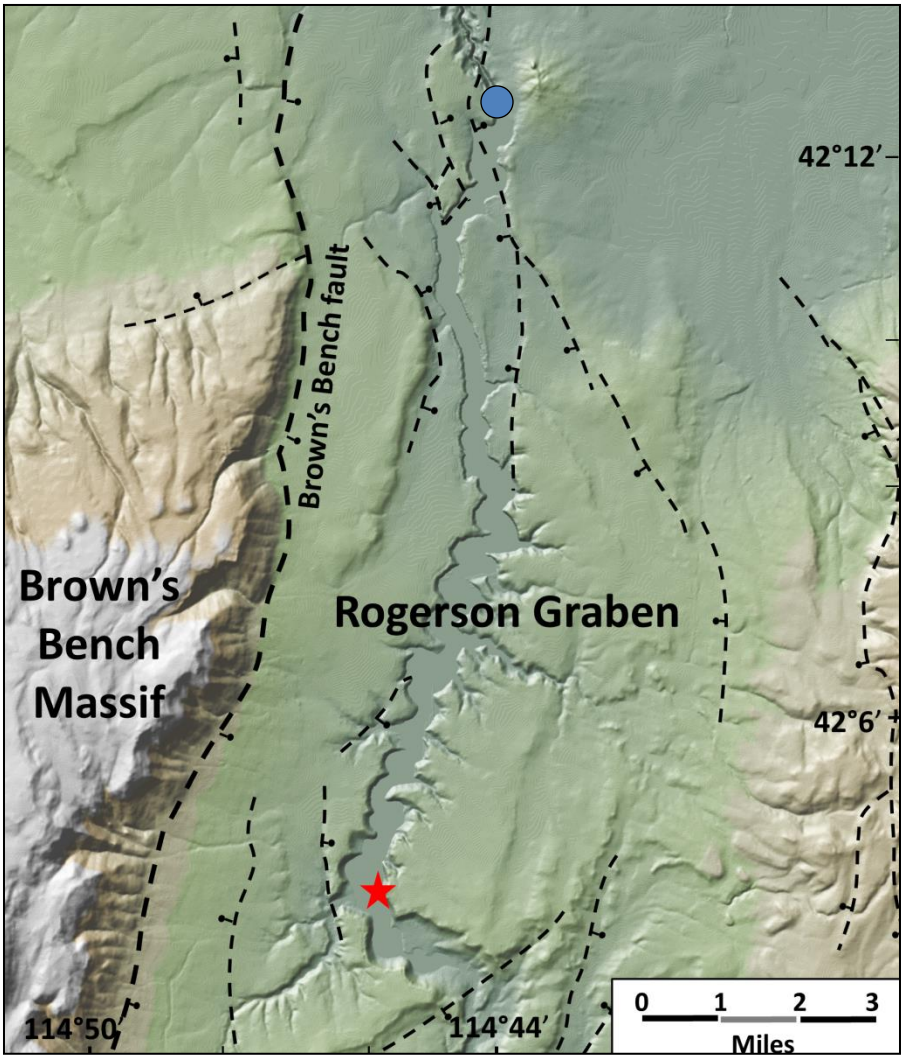

Figure 4: Shaded relief and fault map of the Rogerson Graben showing the sampling locations. Red star: vertical profile through the Grey's Landing Ignimbrite from the underlying thermal contact zone to upper lithoidal (Lat.\Long.= 42° 4'5"\114° 45'45"). Blue circle: upper vitrophyre sampling location at Salmon Dam (Lat.\Long.= 42° 12'42"\114° 44'6"). Figure 1 shows the location of this map as an inset.

	Thermal Demag. Zjiderveld Plot	Normalized Demagnetization	Temperature Susceptibility Curve (in Argon)	Hysteresis Curve
BS8	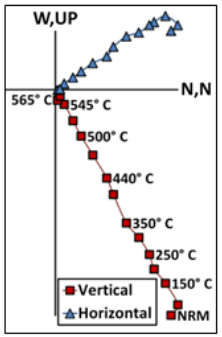	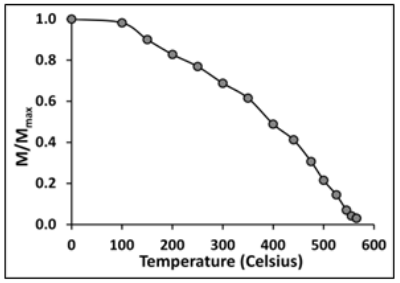	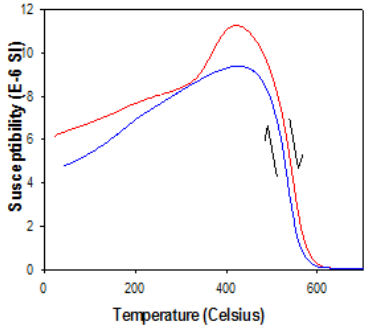	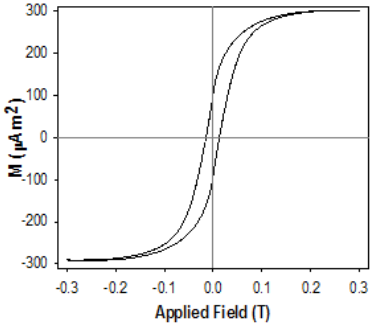
LBV10	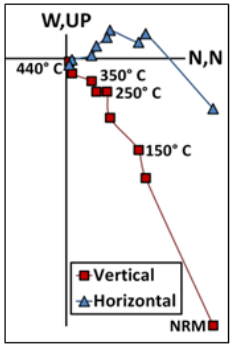	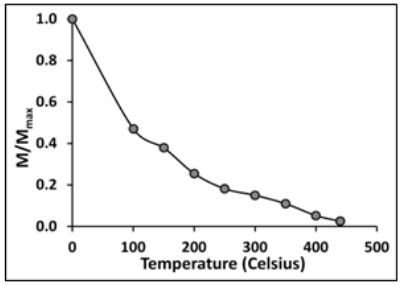	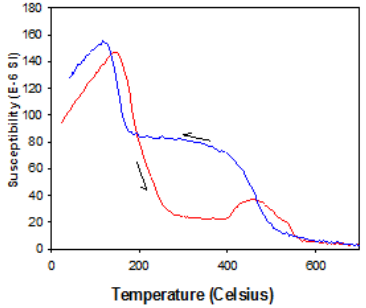	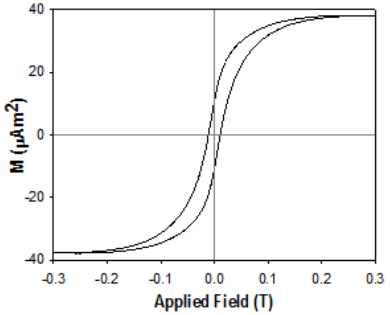
UBV16	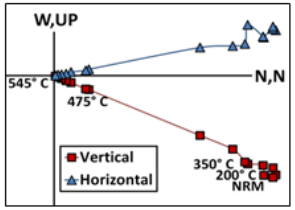	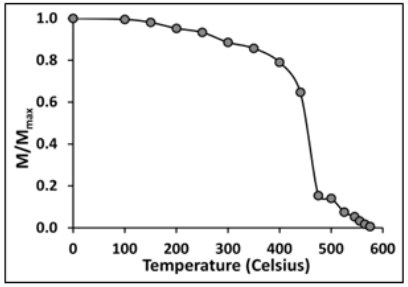	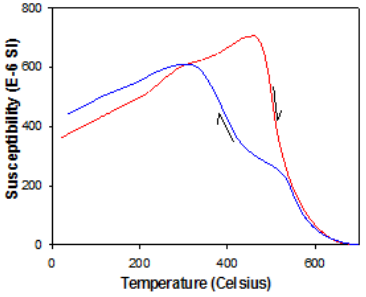	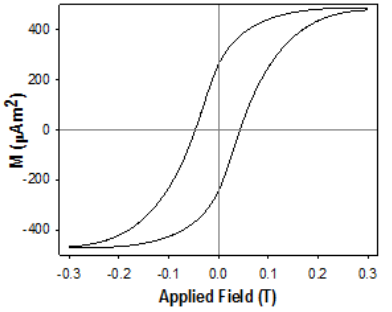

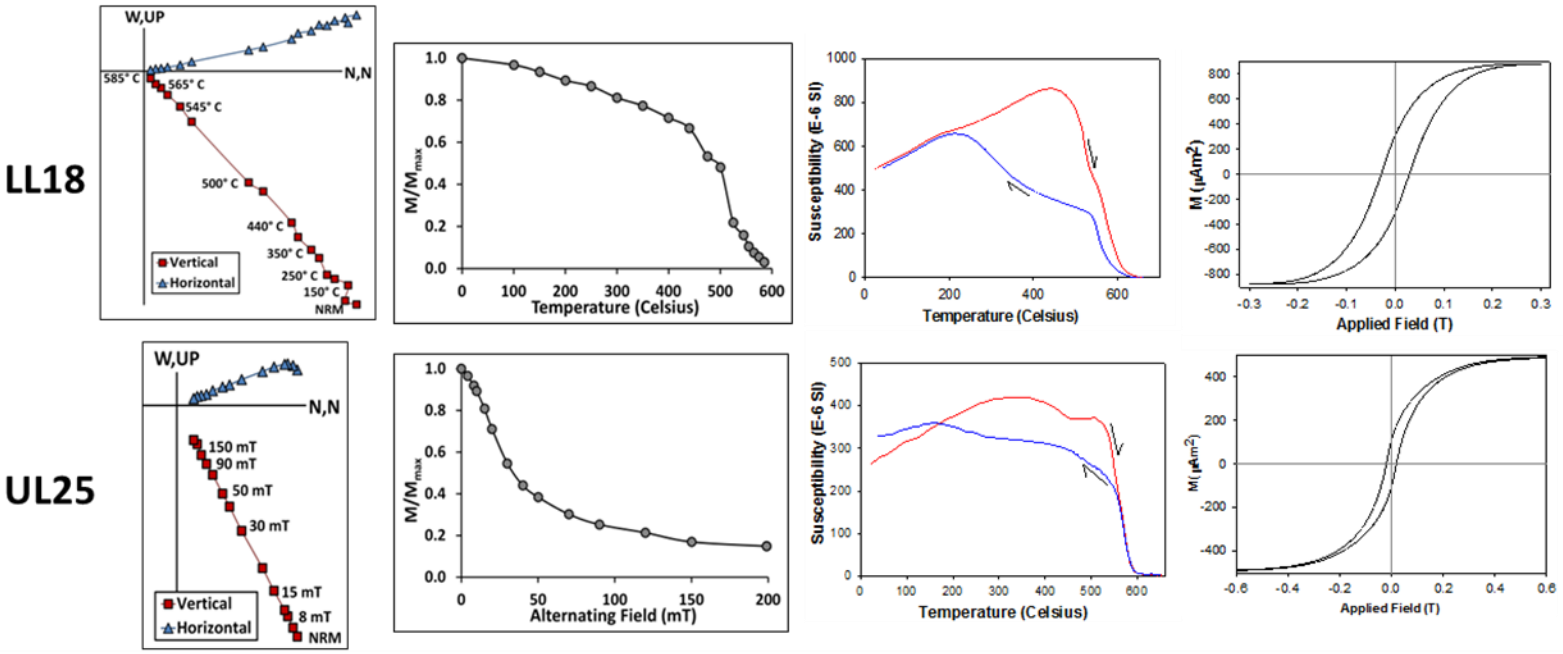

Figure 5: (Continued from previous page) Typical zjiderveld diagrams of thermal and alternating magnetic field demagnetizations of samples from Grey's Landing ignimbrite together with their associated normalized decay of magnetization, temperature susceptibility curves measured in argon, and hysteresis loops, are shown for the baked soil (BS), lower basal vitrophyre (LBV), upper rheomorphic basal vitrophyre (UBV), lower transitional lithoidal (LL), and lithoidal (UL) zones.

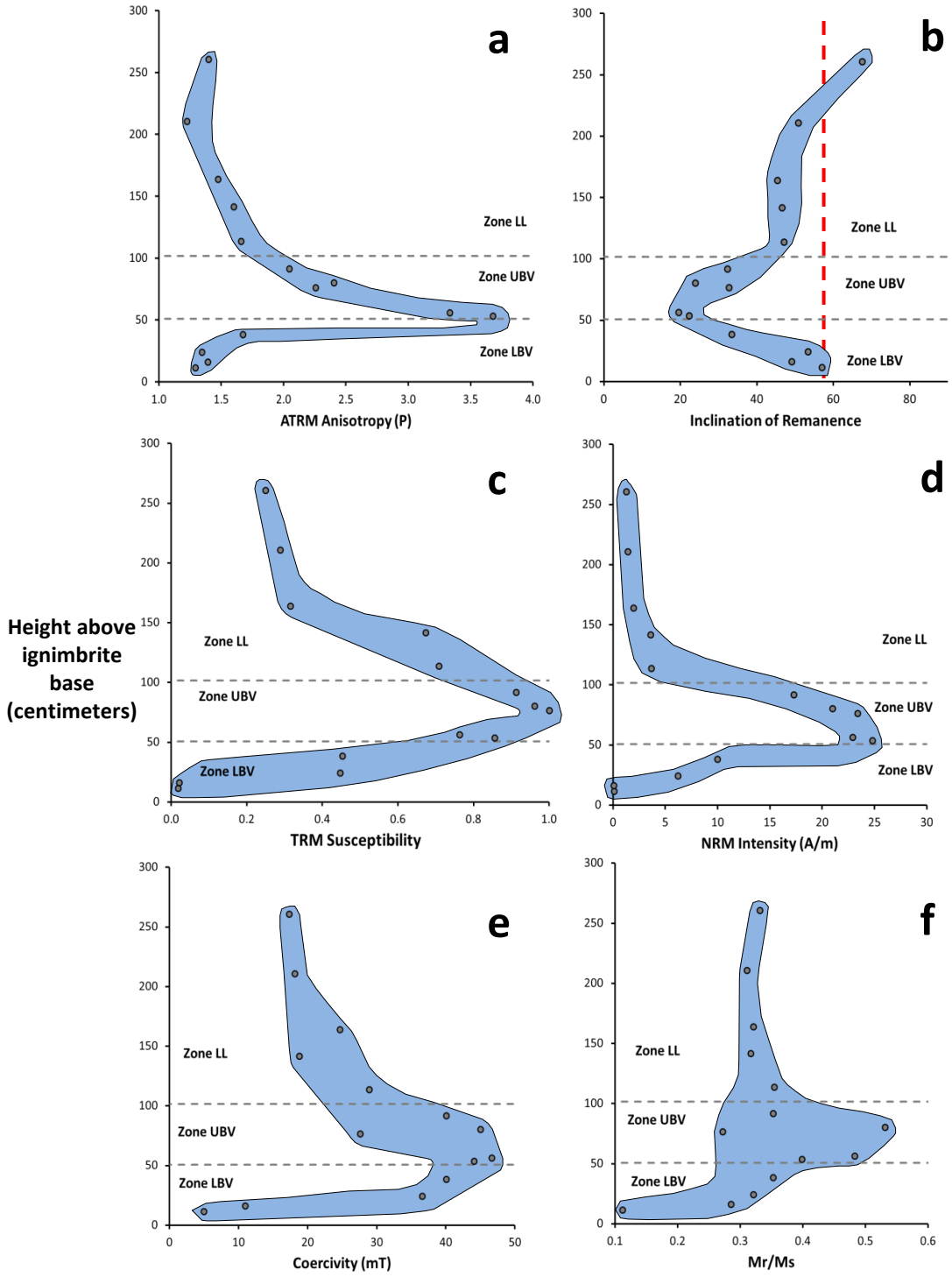
a
b
c
d
e
f
Zone LL
Zone UBV
Zone LBV
ATRM Anisotropy (P)
Inclination of Remanence
TRM Susceptibility
NRM Intensity (A/m)
Coercivity (mT)
Mr/Ms
Height above ignimbrite base (centimeters)

Figure 6. (Previous page) Systematic changes of magnetic parameters as a function of height above base. Plots show ATRM anisotropy, remanence inclination, normalized ATRM susceptibility, NRM intensity, coercivity, and the ratio of magnetic remanence to magnetic saturation (Mr/Ms) versus height (centimeters) above the base of the Grey's Landing ignimbrite. The ATRM corrected baked soil remanence inclination is indicated by a dashed red line in Figure 6b.

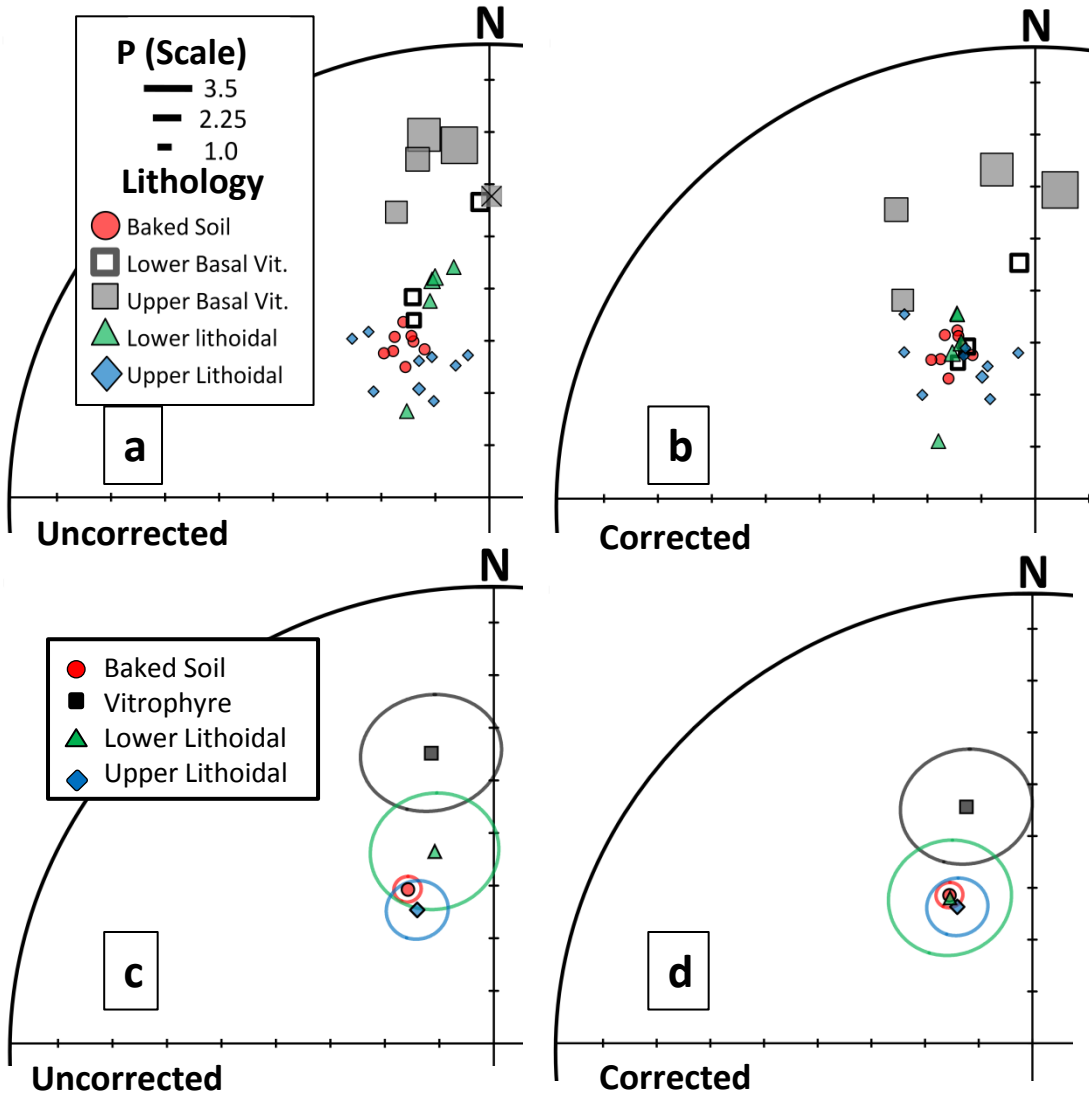

Figure 7: Lower hemisphere stereographic plot of individual sample (a,b) and lithology mean (c,d) directions before and after correcting using the measured ATRM tensor. The vitrophyre sample direction from plot 'a' with an 'X' in the symbol lost its orientation before the anisotropy of thermal remanence measurements and does not have a corrected direction in plot 'b'. The size of samples in plots 'a' and 'b' indicates the intensity of anisotropy (P).

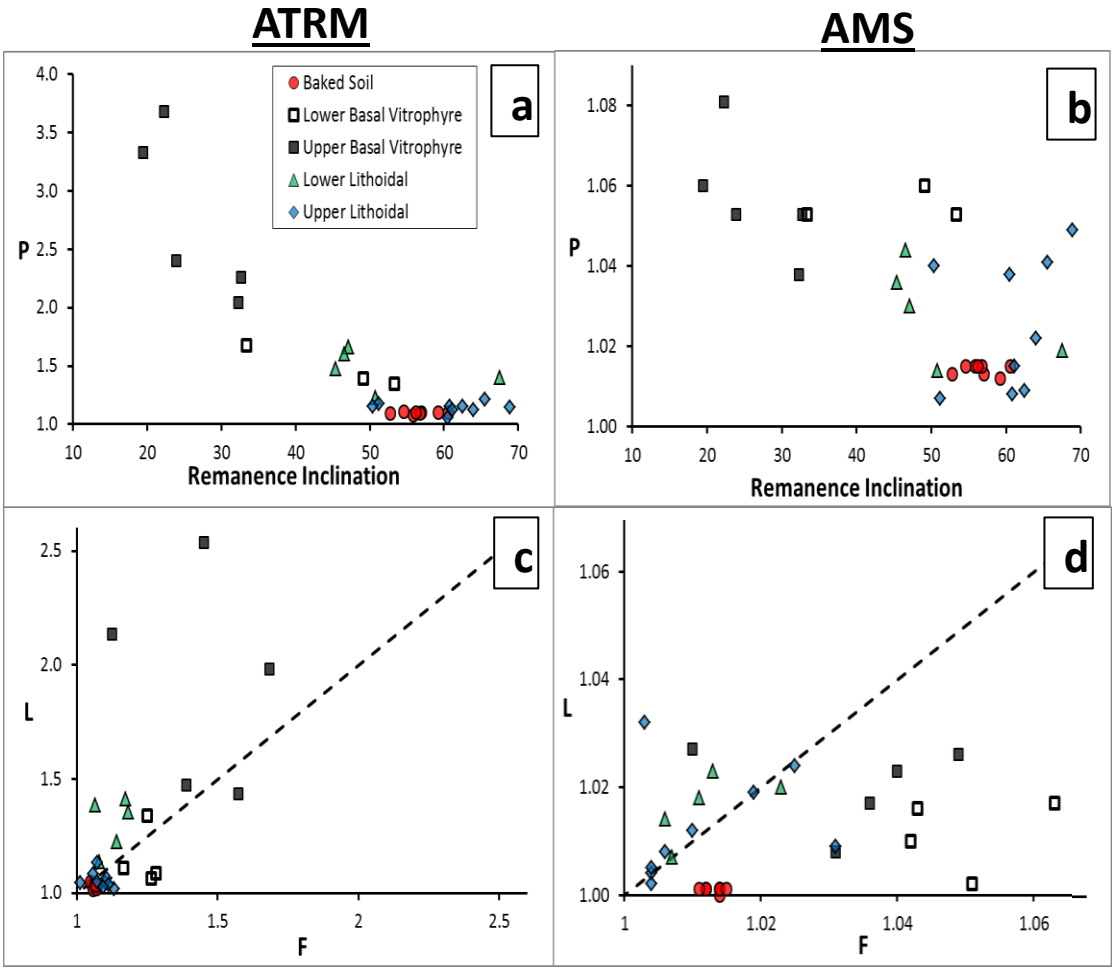

Figure 8: Systematics of anisotropy parameters—ATRM vs. AMS. (a) and (b): Note the excellent correlation of stronger ATRM (P) with shallow inclination, much better than that shown by AMS. (c) and (d): Note that the more anisotropic samples show much stronger lineation (L) than foliation (F) for ATRM, whereas the opposite is true for AMS. Sample LBV9 has an overprinted remanence direction and is only seen in plots 'c' and 'd'.

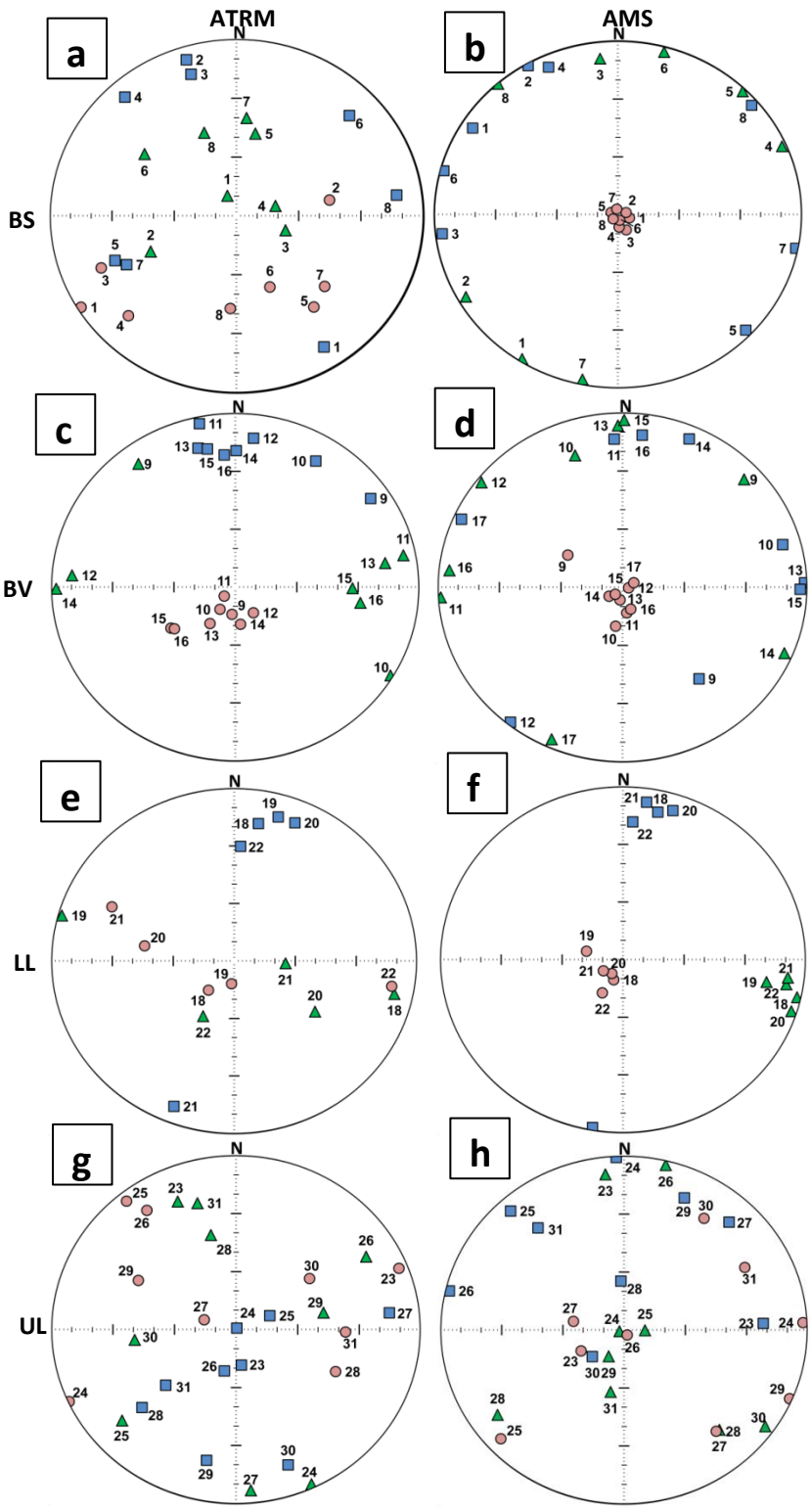
ATRM
AMS
a
b
c
d
e
f
g
h
BS
BV
LL
UL
N

Figure 9: (Previous page) Systematics of anisotropy eigenvectors—ATRM vs. AMS. Maximum (K1, blue squares), intermediate (K2, green triangles), and minimum (K3, pink circles) susceptibility directions are shown for baked soil (BS), upper and lower basal vitrophyre (BV), lower lithoidal (LL), and upper lithoidal (UL). Symbols are labeled by the number segment of their sample name. All directions are plotted on the lower hemisphere.

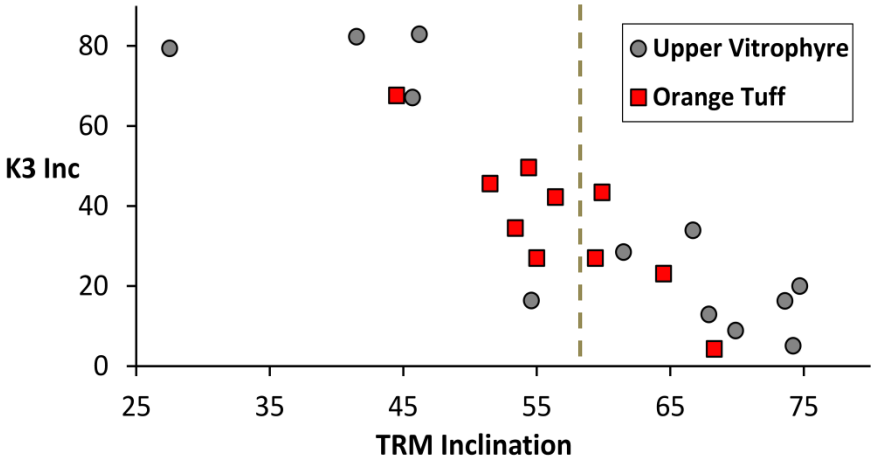

Figure 10: $K3_{AMS}$ inclination vs. TRM inclination. Folding preceded TRM acquisition, so the systematic dependence of TRM direction on orientation of magnetic fabric is because anisotropy has caused major deflections of remanence (see text). Dashed line represents inclination of the baked soil. Because the deflections largely averaged out, the mean directions of the upper vitrophyre (UV) and orange tuff (OT) correspond well with the ancient field direction (Table 3).

Chapter 2

A New Protocol for 3-Axis Static Alternating Field Demagnetization of Rock

1. Introduction

The most widely used method for demagnetizing rocks requires application of an alternating field along three orthogonal directions and one measurement of remanence for each step in a sequence of progressively increased peak-field intensities. The AF causes rapid flips of the magnetic moment of grains and randomization of their direction. This sudden forced rotation of the magnetic moment vector for grains of a particular size, shape, and composition, takes a gyroscopic form due to a transient field generated antiparallel to the rotation vector during the flip [Stephenson 1980]. As a result, a sample acquires a net GRM that is perpendicular to both the applied AF and direction of preferred grain alignment in the sample. This is typically thought of as a spurious unwanted component of AF demagnetization, and if large enough, can make demagnetization data unusable if it has not been accounted for (Figures 1a, 1e). Dankers and Zjiderveld [1981] devised a measurement routine that excludes measured components affected by GRM. This procedure, which we refer to as the exclusion method, requires five AF applications (e.g. AF along y, z, x, y, then z) with measurements of remanence made after each of the last three AFs. The only component of magnetization used from each measurement is the one in which the AF was applied along just before the measurement is made. Because GRM is acquired perpendicular to the AF direction, in many cases these three measurements yield three GRM-free NRM components (Figures 1d, 1h).

Despite GRM being commonly reported in paleomagnetically important minerals, such as fine-grained magnetite, the exclusion method is not regularly implemented because it entails so much extra laboratory work. This is partly because it cannot be known in advance if a particular sample will suffer from GRM effects, and the extra precautionary steps, which nearly triple the amount of lab work, could be unnecessary. GRM can be a big problem for paleomagnetic laboratories that have automated routines for completely AF demagnetizing samples, the more so if they demagnetize large batches at a time.

To reduce the effect of GRM without extra measurements, in our Santa Cruz lab we permute the order of AF axes with each progressively larger AF step [Morris et al., 2009]. This has the effect of permuting the direction in which the GRM component is acquired between subsequent AF steps, enabling a significantly better determination of the stable natural remanence during routine principal component analysis if GRM is not too large (Figures 1b, 1f, 2). In cases where GRM is excessive, we have developed a simple subsequent analysis, the Smoothing-Interpolation (SI) method, which achieves excellent results by dramatically reducing the amplitude of GRM with no additional laboratory measurements. Here we demonstrate the proposed method on both natural and anhysteretic remanence demagnetizations of a welded tuff sample (Figures 1c, 1g, 2). But even if one does not expect to use the SI method, we recommend that permutation of demagnetization axes be adopted as a standard

procedure for 3-axis AF demagnetization so that GRM effects can be dealt with if they turn out to be serious.

2. Sample Description

The paleomagnetic sample chosen for this paper was collected from the crystalline center of the Cougar Point Tuff (CPT) Xll ignimbrite in southwest Idaho, an intensely welded sheet of ash-flow tuff emplaced at high temperature over a large area in the mid-Miocene [Bonnichsen and Citron 1982]. Its NRM is weak and southeast and down, indicating that it was magnetized in a weak transitional field of intermediate polarity, and thus during AF demagnetization its GRM makes a relatively larger contribution to the remanence. The GRM in these ignimbrites is carried by anisotropic fine-grained magnetite, which likely crystallized from the volcanic glass during and shortly after deposition [Finn et al., 2015 and references therein]. We collected samples from the CPT Xll along the Bruneau River and the East and West Forks of the Jarbidge River. The NRM of samples from this tuff typically consists of three components, a minor low- and tiny high-coercivity normal component that overprints a larger intermediate transitional component acquired during initial cooling.

3. NRM Demagnetization and Analysis

We progressively AF demagnetized and measured remanence of the rhyolitic sample using a Sapphire SI-4 demagnetizer that is mounted inline with a 2G cryogenic magnetometer. Both instruments are held in a magnetically shielded room at the UC Santa Cruz Paleomagnetism Laboratory, and automated demagnetization is run by custom software [Morris et al., 2009]. To compare the effects of GRM, we followed the Dankers and Zjiderveld [1981] procedure and applied the AF sequentially along the y, z, x, y, and then z directions, with measurements of the magnetization after the last three steps [Appendix].

3.1 Non-Permuted Demagnetization

Most paleomagnetic laboratories do not permute the sample axes in which the AF is applied during a progressive demagnetization. Figure 1a and 1e show results from a non-permuted demagnetization where we only used one of the three remanence measurements made at each step level. For the example shown in figure 1a and 1e, the AF was applied sequentially along the y, x, and then z sample axes before remanence was measured for each peak AF step. For this procedure, GRM is not acquired along the z sample axis during demagnetization, and increases along the x and y sample axes. This causes a deflection of remanence away from the NRM direction and the illusion of a high-coercivity component of magnetization that cannot be removed.

3.2 Permuted Demagnetization

This procedure has the beneficial effect of permuting the direction in which the GRM is acquired with each subsequent AF step level. Therefore, the sum of the acquired GRM during the entire demagnetization approaches zero with increased number of steps used, which minimizes the effect of GRM on the resultant line fits to the NRM components (Table 1; Figure 2). The more AF steps used in a demagnetization, the more effective the PCA will be in averaging out the oscillatory GRM component. In contrast to the non-permuted AF routine, the presence of the oscillatory component in a permuted demagnetization can uniquely be identified as GRM. This feature can appear as small high frequency perturbations to the demagnetization data if the GRM is relatively small, or as the large spiral pattern in figure 1b and 1f if the GRM is relatively large.

Another benefit of permuted demagnetization is that the mean angular deviation (MAD) can be used as a relative measure of the amount of GRM that is acquired within the AF range in which the line fit was made. The MAD value will only take into account the amount of GRM that is perpendicular to the line fit. This easy evaluation of the GRM for large numbers of samples may help reveal possible relationships with other magnetic variables such as NRM intensity, magnetic anisotropy, remanence direction, coercivity, minerology and ultimately, the

underlying physical processes. In addition, the MAD may be used as a gauge of whether the subsequent SI method proposed here is required.

3.3 Smoothing-Interpolation Method

The major advantage of permuted demagnetization is that a subsequent analysis (e.g. SI method) can be used to greatly reduce GRM (Figures 1c , 1f, and 2). The Smoothing-Interpolation (SI) method involves repeated calculation of a three-step running mean for each measured component (x, y, and z) and subsequent restoration of GRM-free measurements (see section 4 below). This method effectively removes the oscillatory GRM component in a progressive three-axis demagnetization with permuted AF axes. Having the option for using the SI method allows for large batches of paleomagnetic samples to be demagnetized without the need for extra measurements. The SI method could be used to remove GRM if it is shown to be a problem after the measurements have already been made. Furthermore, smoothing demagnetization data with the SI method may dramatically reduce the relatively large effect that even a small oscillatory GRM component may have on partial remanence vectors.

3.4 Exclusion Method

The method of excluding GRM effected measurements proposed by Dankers and Zjiderveld (1981) greatly reduces the amount of GRM acquired during the AF demagnetization (see section 1). Results from this method provide the correct answer that we use to evaluate the effectiveness of the SI method (Figures 1c, 1d, 1g, 1h, and 2). Both the exclusion method and SI method rely on the assumption that after application of three orthogonal alternating fields, there will be no GRM along the last AF direction. This assumption is generally true for samples that contain fine-grained magnetite, but may be invalid for samples containing iron sulfides such as greigite [Hu et al 1998].

3.5 How well does the SI method work?

The remanence directions calculated using PCA on the permuted demagnetization with and without use of the SI method, are .8° and 5.5° from that of the exclusion method, respectively (Table 1; Figure 2). In this case, the additional use of the SI method was required to successfully remove the GRM effect on the line fit. Measurements made at AF levels below 15 mT were excluded due to a small overprint and the 140 mT step has error from the correction method applied to the last measurement (See Step 4a in section 4.3 below). There is a very small high coercivity normal overprint (Figure 1g and 1h), so we do not force the PCA through the origin for any line fit except that of the unsmoothed permuted demagnetization. Forcing the line fit through the origin of the unsmoothed permuted demagnetization reduces the

unwanted influence of the most GRM affected high AF steps.. Without forcing the line fit through the origin, the direction found through PCA will have considerably more error and is partly dependent on the order of AF axes.

4. Application of the Smoothing-Interpolation Method

4.1 Laboratory Procedure

To create a permuted demagnetization from the full laboratory routine required for the exclusion method (see section 3), we kept only the first measurement from the lowest peak AF step, second measurement from the second peak AF step, third measurement from the third AF step, first measurement from the fourth AF step, second measurement from the fifth AF step, etc [Supporting Information]. The beginning steps for the typical, much shorter laboratory procedure that would produce permuted demagnetization results are listed below as an example.

1. Measure remanence
2. Apply 5mT AF along Z, then Y, then X
3. Measure remanence
4. Apply 10mT AF along X, then Z, then Y
5. Measure remanence
6. Apply 15mT AF along Y, then X, then Z
7. Measure remanence
8. Apply 20mT AF along Z, then Y, then X

>8. Continue permutation at higher fields

4.2 Benefits and Pitfalls of the Three-Step Running Mean

The GRM that is acquired during a demagnetization with permuted axes has a periodic form in each of the three measured components of magnetization (x, y, & z), and which is repetitive in steps of three (Figure 3a). Ideally, the average GRM for any given 3-step segment should be close to zero, with one of the three measurements having no GRM (measurement along the last AF direction), and the other two measurements should have GRM components close to equal and opposite of each other (see figure 3 from Stephenson 1993). Therefore, a simple 3-step running mean may be used as a very effective means of removing GRM. Use of the running mean, however, won't perfectly correct GRM affected measurements, and will have the unwanted effect of altering measurements that are known to be GRM free. In addition, the running mean will not correct that last measurement of the demagnetization, which is needed for two of the three measured components (i.e. x, y, z).

4.3 Detailed Description of the Smoothing-Interpolation Method

A simple iterative procedure can be used to overcome the pitfalls of the three-step running mean described above in section 4.2. In the description that follows, the term 'series' will be used to refer to the component of magnetization being analyzed (i.e. x, y or z), but it should be known that this analyses needs to be done on all three components.

Step 1: Choose how many measurements from the early steps of the series that should be kept fixed (Figure 3a). Measurements made at peak AF values below which GRM becomes visibly evident should be kept fixed, particularly if they contain a low coercivity overprint of interest. For the NRM analysis presented here, we fixed all measurements that following AF applications of 9 mT or less (Figure 3a).

Step 2: Take the 3-step running mean of the series.

Step 3: Restore all measurements in the series that are known to be GRM free (e.g. low AF values and any measurement along last AF axis) to the original measured value.

Step 4: Apply a correction to the last measurement that is equal and opposite to the correction made on the previous measurement affected by GRM. The closer the GRM is to saturation over the last three AF steps the better this correction will be (Figures 3b, 3c).

Step 5: Repeat steps 2-4 along each component of magnetization until the oscillatory GRM component has been removed and the demagnetization curve is optimally smoothed (Figures 3c-3e).

5. Demagnetization of a Two-Component Anhysteretic Remanence

To conduct a more rigorous test of the SI method, we demagnetized a sample that had two orthogonal laboratory applied anhysteretic remanences (ARM) of known

direction (Figure 4). Using a 0.1 mT direct field (DF), we imparted the high coercivity ARM in the +y sample direction and lower coercivity ARM in the –x direction following the procedure below. The AF values at the peak ramp up, and when the DF turns on and off, are shown with this shorthand with units in mT (peak AF, DF turn on, DF turn off).

1. AF of 160 mT along x, z, and then along y
2. Measure Remanence
3. Apply ARM along +y (160, 150, 80)
4. Measure remanence
5. AF of 83 mT along z, y, and then along x
6. Measure Remanence
7. Apply ARM along -x (83, 80, 0)
8. Measure Remanence

The two remanence measurements before and after the ARM applications have the same hard NRM component that could not be removed and have the same GRM components. Therefor subtraction of the first measurement from the second yields the laboratory applied ARM direction (Table 2). The magnetization acquired from application of the higher coercivity ARM is ~5% of the lower coercivity ARM. The hard NRM component that could not be demagnetized by a150 mT field was subtracted from each remanence measurement made during the ARM demagnetization. The two ARMs that the sample acquired were not exactly parallel to the applied DF directions. The difference in direction is mainly a result of a moderate degree of magnetic anisotropy, though there are smaller contributions from GRM and other instrumental errors.

Without use of the SI method, the high coercivity ARM is almost completely masked by the large GRM and cannot be determined (Figures 4a, 4c, and 4e). The change in the direction of the partial remanence vector from the low coercivity component in the –x direction to the high coercivity component in the +y direction is unclear. After removing GRM with the SI method, however, the sharp bend connecting the two ARM directions can clearly be seen at the 80mT AF step, as expected (Figures 4b, 4d, and 4f). The demagnetization of the high coercivity ARM shows a smooth linear decay toward the origin of the zjiderveld plot. We calculated the line fits for the low and high ARMs with and without using the SI method, and compared these directions to the known ARM directions (Table 2; Figure 4e-f). For this analysis, we used step 4b instead of step 4a from section 4.3 above. The SI method improved the closeness of the line fit to the known high coercivity ARM direction from 5.3° to 1.5° (Table 2). The additional use of the SI method was not needed for the much stronger low coercivity ARM, which was only 1.4° from the known direction without any smoothing. Our instrumentation error for applying ARMs is ~1° at best.

6. Final Remarks

1: We recommend permutation of demagnetization axes be implemented as a standard protocol for 3-axis static AF demagnetization. This procedure allows for detection and elimination of GRM, when its effects are significant, without the need

for the many extra AF and measurement steps required for the method of Dankers and Zjiderveld [1981]. The SI method demonstrated here on an NRM and a two component ARM, can be used as an optional step to improve the demagnetization results of samples strongly affected by GRM.

2: There are many other potentially effective analyses for removing the GRM from a permuted demagnetization besides the SI method. One method we have found useful is based on singular spectrum analysis [Vautard et al., 1992], which yields better results if there is significant non-GRM related error in the measurements. For most cases, however, the simpler SI method is just as effective.

3: The SI and exclusion methods rely on the assumption that no GRM remains along the last AF axes after three orthogonal AF applications. This assumption, however, has been shown to fail for some greigite bearing samples [Hu et al., 1998] and for a troilite bearing meteorite sample measured in our lab [W. Schillinger, In Review]. The SI method will still significantly improve the results, though may have a small error from a GRM in the measurements that are kept fixed. A better approach for demagnetizing these types of samples will be a topic of a future paper.

4: Stephenson (1993) presented a method for measuring GRM anisotropy shape and orientation using only 3 demagnetization axes and assuming an anisotropy shape that is one of revolution. Using the assumptions of Stephenson, GRM anisotropy can be estimated from analysis of the GRM obtained using the SI method. This will be the topic of a future paper.

5: An Excel workbook for application of the SI method can be found in the Supporting Information. This workbook will be added to the Demagnetization Analysis in Excel workbook [Sagnotti 2013], which is available by email request to leonardo.sagnotti@ingv.it.

6: Both the unsmoothed and smoothed data should be made available for any publication that uses the SI method so that the results may be reproduced.

7. Acknowledgements

Field expenses for this work were covered by the Natural Environment Research Council (NERC) Grant NE/G005372/1 awarded to Michael Branney. The salary and school fees for the first author were covered in part by a National Science Foundation (NSF) grant (EAR 1250444) awarded to X. Zhao. Please contact the first author via email at dfinn@ucsc.edu for data requests and other questions. We also would like to thank Andrew Pike for his suggestion and assistance in the use of singular spectral analysis for removing GRM from a permuted demagnetization.

8. References

Bonnichsen, B., & Citron, G. P. (1982). The Cougar Point tuff, southwestern Idaho and vicinity. Cenozoic Geology of Idaho: Idaho Bureau of Mines and Geology Bulletin, 26, 255-281.

Dankers, P. H. M., & Zijderveld, J. D. A. (1981). Alternating field demagnetization of rocks, and the problem of gyromagnetic remanence. Earth and Planetary Science Letters, 53(1), 89-92.

Finn, D. R., Coe, R. S., Kelly, H., Branney, M., Knott, T., & Reichow, M. (2015). Magnetic anisotropy in rhyolitic ignimbrite, Snake River Plain: implications for using remanent magnetism of volcanic rocks for correlation, paleomagnetic studies and geological reconstructions. Journal of Geophysical Research: Solid Earth.

Hu, S., Appel, E., Hoffmann, V., Schmahl, W. W., & Wang, S. (1998). Gyromagnetic remanence acquired by greigite (Fe3S4) during static three-axis alternating field demagnetization. Geophysical Journal International, 134(3), 831-842.

Morris, E. R., W. Schillinger, R. S. Coe, C. J. Pluhar, and N. A. Jarboe (2009), Automating the 2G superconducting rock magnetometer for single-solenoid alternating field demagnetization, Geochem. Geophys. Geosyst., 10, Q05Y05, doi:10.1029/2008GC002289.

Sagnotti, L. (2013). Demagnetization Analysis in Excel (DAIE). An open source workbook in Excel for viewing and analyzing demagnetization data from paleomagnetic discrete samples and u-channels. Annals of Geophysics, 56(1), D0114.

Stephenson, A. (1980). A gyroremanent magnetisation in anisotropic magnetic material. Nature, 284(5751), 49-51.

Stephenson, A. (1993). Three-axis static alternating field demagnetization of rocks and the identification of natural remanent magnetization, gyroremanent magnetization, and anisotropy. Journal of Geophysical Research: Solid Earth (1978–2012), 98(B1), 373-381.

Vautard, R., Yiou, P., & Ghil, M. (1992). Singular-spectrum analysis: A toolkit for short, noisy chaotic signals. Physica D: Nonlinear Phenomena, 58(1), 95-126.

9. Table Captions

Table 1: Results from principal component analyses (PCA) are shown for a 3-axis static AF demagnetization of an NRM. Line fits were calculated over a 15-80mT range before and after use of the Smoothing-Interpolation (SI) method, and with the use of the full exclusion method. Only the PCA on the unsmoothed data was forced through the origin. The table contains declination, inclination, mean angular deviation (MAD°), and angle made with the direction found using the exclusion method (Error(°)).

Table 2: Results from principal component analyses on a 3-axis static AF demagnetization of a two component ARM are shown for the unsmoothed and smoothed (SI method) data and compared to the known ARM direction. The table contains declination, inclination, mean angular deviation (MAD°), and angle made with the known ARM direction (Error(°)). The PCA analyses were calculated over the 5-80mT and 80-140mT range

10. Figure Captions

Figure 1: Zjiderveld plots (a-d) and associated stereonets are shown demonstrating the usefulness of the SI method. These plots show results from a demagnetization that does not permute the order of AF axes (1a, 1e), does permute AF axes (1b, 1f), permutes axes and implements the SI method to remove GRM (1c, 1g), and the exclusion method of Dankers and Zjiderveld (1981) with the repeated AF applications and measurements at each peak AF step.

Figure 2: Stereonet plot shows the direction of thermal remanence determined for a welded tuff sample using permuted AF axes, the SI method, and using all the extra measurements required for the exclusion method (Dankers and Zjiderveld 1981).

Figure 3: The Y-component of magnetization is shown to demonstrate the SI method (a-c). This method was applied to each axis and the results are shown in zjiderveld plots (d, e). The unsmoothed data are shown in 'a' with the GRM affected and GRM free measurements indicated. The smoothed results have been added to this plot after one (b) and six (c) iterations of the SI method. The dashed black lines in plots 'b' and 'c' are of equal length and show one of the suggested methods (step 4a in text) of correcting for GRM in the last measurement. Most of the GRM is removed by one iteration (b, d), but in this case it takes several more iterations before the SI method produces smooth results (c, e).

Figure 4: Demagnetization of a two component ARM using permuted AF axes is shown with (b, d, f) and without (a, c, e) using the additional SI method. The ARM is in the –x direction from 0-80mT and in the y direction from 80-150mT. The SI method was needed to accurately get the high coercivity ARM but not the low ARM (Table 2). The ARMs are not perfectly along the axes, which primarily results from a moderate degree of magnetic anisotropy.

Table 1. Line fit results from demagnetization of a NRM

Method	Dec.	Inc.	MAD (°)	Error (°)
Unsmoothed	137.0	51.2	24.6	5.50
SI method	144.6	49.2	2.0	0.80
Exclusion	145.3	49.9	1.8	0.00

*Results from principal component analyses (PCA) are shown for a 3-axis static AF demagnetization of an NRM. Line fits were calculated over a 15-80mT range before and after use of the Smoothing-Interpolation (SI) method, and with the use of the full exclusion method. Only the PCA on the unsmoothed data was not forced through the origin. The table contains declination, inclination, mean angular deviation (MAD°), and angle made with the direction found using the exclusion method (Error(°)).

Table 2. Line fit results from demagnetization of a two-component ARM

High Coercivity ARM (80-140mT)

Method	Dec.	Inc.	MAD (°)	Error (°)
Known	89.4	4.3	-	-
SI	90.4	3.2	0.7	1.48
Unsmoothed	93.8	7.3	18.0	5.25

Low Coercivity ARM (5-80mT)

Method	Dec.	Inc.	MAD (°)	Error (°)
Known	179.3	-7.9	-	-
SI	177.7	-8.1	0.7	1.53
Unsmoothed	177.8	-8.2	1.0	1.44

*Results from principal component analyses on a 3-axis static AF demagnetization of a two component ARM are shown for the unsmoothed and smoothed (SI method) data and compared to the known ARM direction. The table contains declination, inclination, mean angular deviation (MAD°), and angle made with the known ARM direction (Error(°)). The PCA analyses were calculated over the 5-80mT and 80-140mT range for ARMs that were applied over the 0-80mT and 80-150mT ranges, respectively.

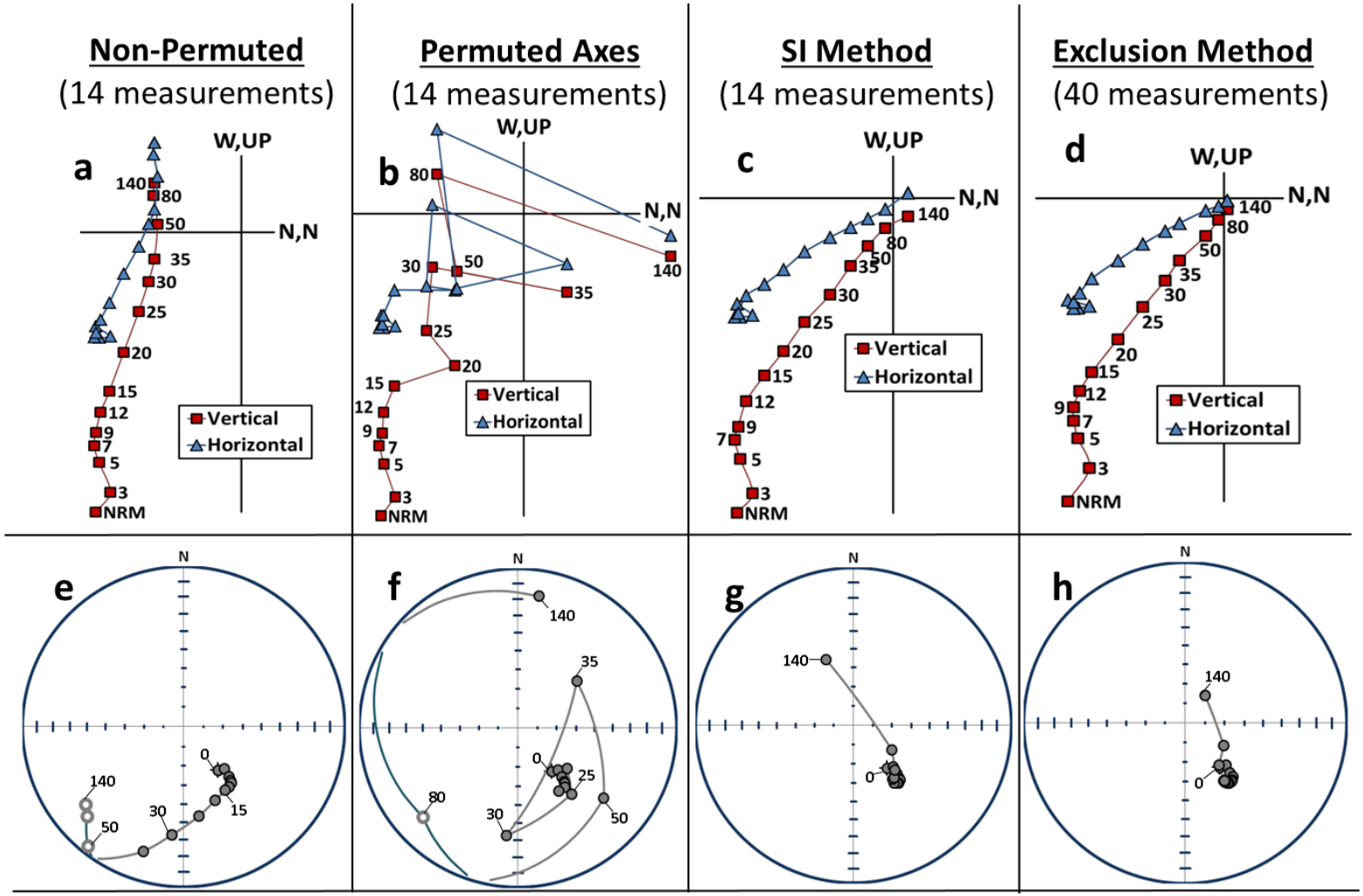
Non-Permuted
(14 measurements)
Permuted Axes
(14 measurements)
SI Method
(14 measurements)
Exclusion Method
(40 measurements)
a
b
c
d
W,UP
N,N
Vertical
Horizontal
NRM
e
f
g
h
N

Figure 1. (Previous Page) Zijderveld plots (a-d) and associated stereonets are shown demonstrating the usefulness of the SI method. These plots show results from a demagnetization that does not permute the order of AF axes (1a, 1e), does permute AF axes (1b, 1f), permutes axes and implements the SI method to remove GRM (1c, 1g), and using the Exclusion method of Dankers and Zjiderveld (1981) requiring repeated AF applications and measurements at each peak AF step. The permuted and non-permuted demagnetizations were created by selectively choosing from the three measurements made at each peak AF step

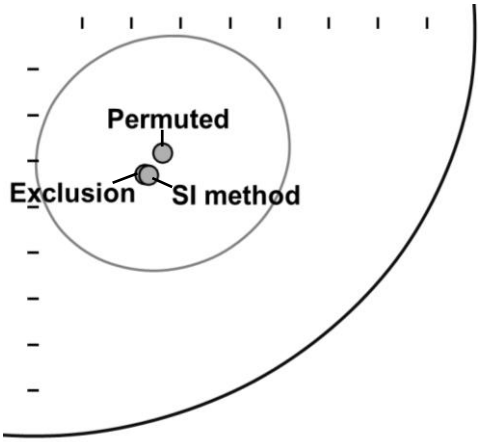

Figure 2. Stereonet plot shows the direction of thermal remanence determined for a welded tuff sample using permuted AF axes, the SI method, and using all the extra measurements required for the exclusion method (Dankers and Zijderveld 1981).

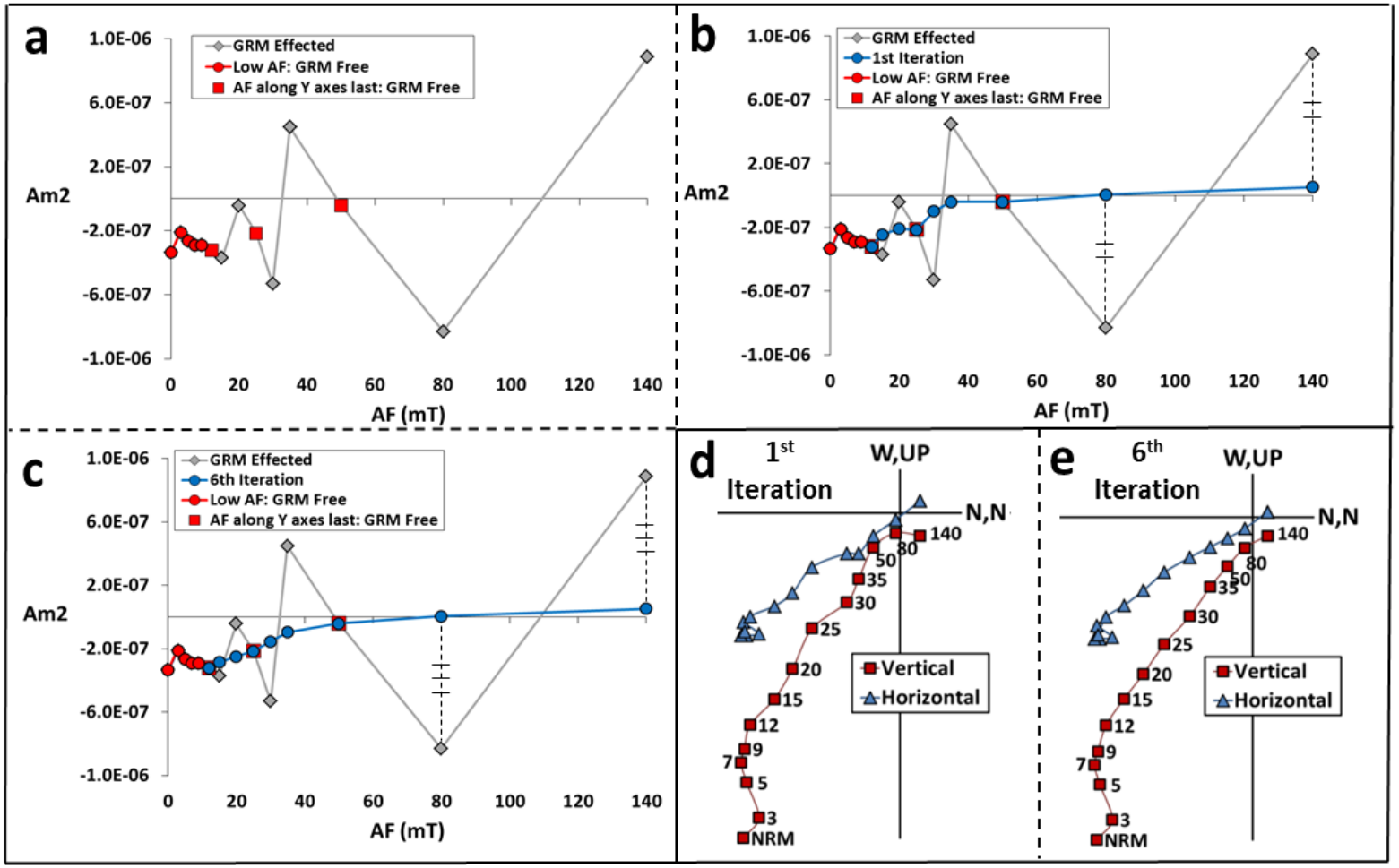
a
GRM Effected
Low AF: GRM Free
AF along Y axes last: GRM Free
Am2
AF (mT)
b
GRM Effected
1st Iteration
Low AF: GRM Free
AF along Y axes last: GRM Free
Am2
AF (mT)
c
GRM Effected
6th Iteration
Low AF: GRM Free
AF along Y axes last: GRM Free
Am2
AF (mT)
d
1st Iteration
W,UP
N,N
Vertical
Horizontal
NRM
e
6th Iteration
W,UP
N,N
Vertical
Horizontal
NRM

Figure 3. (Previous Page) The Y-component of magnetization is shown demonstrating the SI method (a-c). This method was applied to each axis and the results are shown in zijderveld plots (d, e). The unsmoothed data are shown in 'a' with the GRM effected and GRM free measurements indicated. The smoothed results have been added to this plot after one (b) and six (c) iterations of the SI method. The dashed black lines in plots 'b' and 'c' are of equal length and show one of the suggested methods (step 4a in text) of correcting for GRM in the last measurement. Most of the GRM is removed by one iteration (b, d), but in this case, it takes several more iterations before the SI method produces smooth results (c, e).

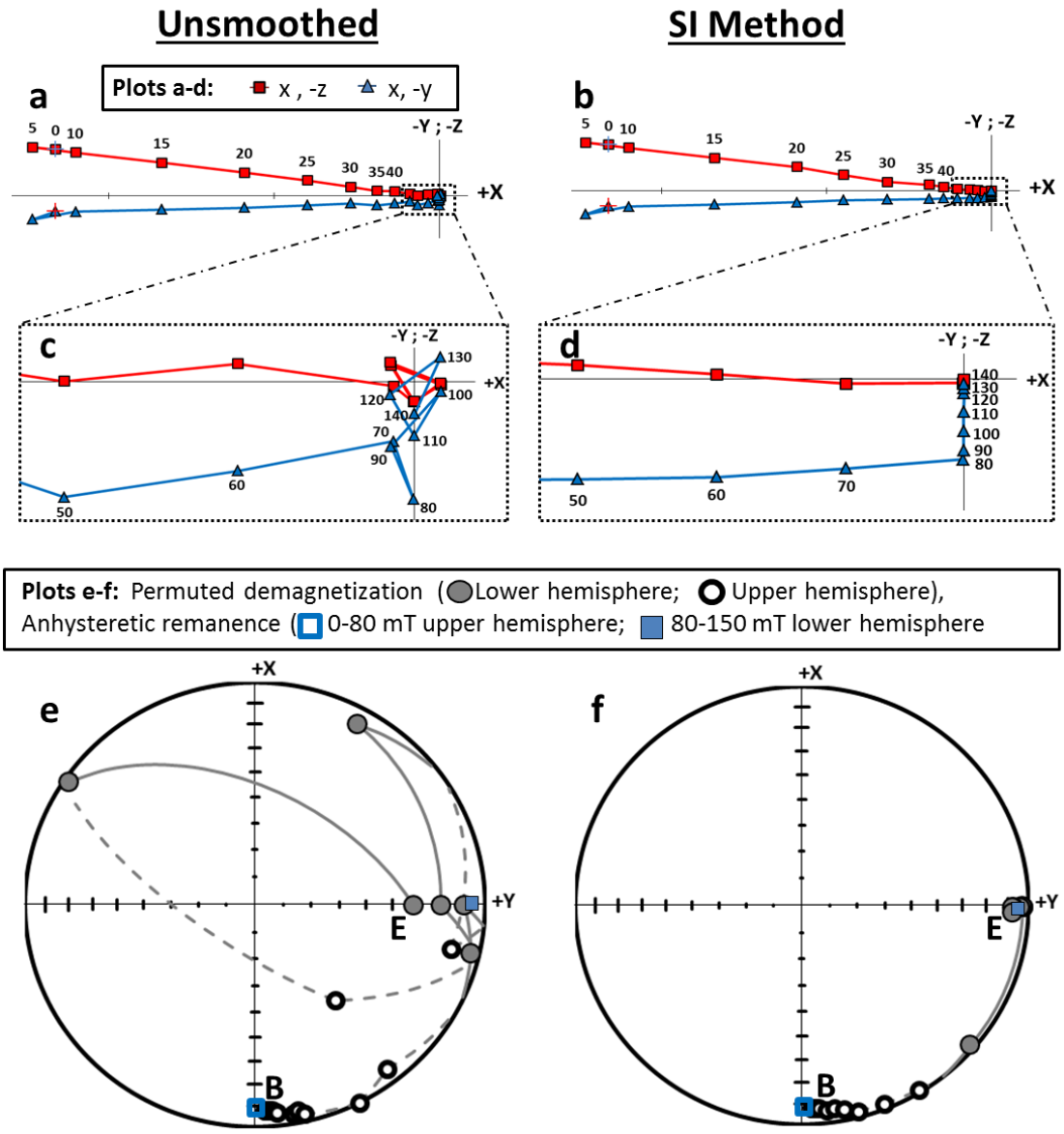

Figure 4. Demagnetization of a two component ARM using permuted AF axes is shown with (b, d, f) and without (a, c, e) using the additional SI method. The ARM is in the –x direction from 0-80mT and in the y direction from 80-150mT. The SI method was needed to accurately get the high coercivity ARM but not the low ARM (Table 2). The ARMs are not perfectly along the axes, which primarily results from a moderate degree of magnetic anisotropy.

Chapter 3

Distinguishing and Correlating deposits from large Ignimbrite Eruptions Using Paleomagnetism: The Cougar Point Tuffs (Mid-Miocene), Southern Snake River Plain, Idaho, USA

Chapter 3

Distinguishing and Correlating deposits from large Ignimbrite Eruptions Using Paleomagnetism: The Cougar Point Tuffs (Mid-Miocene), Southern Snake River Plain, Idaho, USA

1. Introduction

Migration of the Yellowstone Hotspot across continental USA during the Miocene has left a trail of time-transgressive bimodal rhyolitic to basaltic volcanism in the Snake River Plain (SRP) of Idaho (Fig. 1 Map). Along the axis of the SRP younger basalt lavas overlie voluminous rhyolitic ignimbrites and lavas, whereas in hills flanking the SRP successions of outflow rhyolitic ignimbrites are well exposed [Armstrong and others 1975; 1980; Bonnichsen and Citron 1982; Pierce and Morgan 1992; Manley and McIntosh 2002; Morgan and McIntosh 2005; Knott et al. 2016a]. The ignimbrites are intensely welded and rheomorphic outflow sheets from large, environmentally catastrophic explosive Yellowstone Hotspot eruptions (Branney and others, 2008). Development of a regional ignimbrite stratigraphy (Figure 2 Correlations) by correlation of individual eruption-units (e.g. cooling units) is essential to constrain the eruption volumes, eruption frequencies, and to better understand the causal relationship between magma productivity, tectonics, and climate change.

In this contribution, we use paleomagnetism, geochronology, and whole rock and mineral chemistry for stratigraphic correlation of the well-recognized (e.g. Bonnichsen and Citron, 1982) Cougar Point Tuff (CPT) units with other eruption-units exposed in the nearby Brown's Bench (Fig. 3 pictures) escarpment and the Cassia Mountains regions of southern Idaho (Fig. 1 map). Description of the local successions at the Black Rock (Cougar Point Tuffs) and Brown's Bench (Rogerson

Formation) escarpments, and Cassia Mountains (Cassia Formation) can be found in Bonnichsen and Citron [1982], Knott and others [2016a], and Knott and others [2016b], respectively.

Of the various techniques we have employed for identification and correlation of eruption units, paleomagnetism has proved exceptionally useful. The method proposed by Bogue and Coe [1981] was used to quantify the paleomagnetic correlation between individual eruptions and sequences of eruptions. There are, however, several pitfalls that can hinder determination of the primary paleomagnetic remanence direction of rheomorphic rhyolitic ignimbrites, such as in the SRP. These pitfalls include, but are not limited to, magnetic overprinting during growth or alteration of magnetic minerals at low temperatures, large magnetic anisotropy, and acquisition of gyroremanence magnetization during AF demagnetization. Therefore it is important that paleomagnetic correlations are also supported by field, mineralogical, geochemical and radiometric data.

1.1. Snake River (SR)–Type Ignimbrites

Pyroclastic deposits along the margins of the central Snake River Plain exemplify a newly defined class of volcanism, known as SR-type volcanism [Branney and others, 2008]. The most impressive sections of ignimbrites of this type in the Snake River Plain is the ~450 meter tall Black Rock Escarpment [Bonnichsen and Citron, 1982]

along the Bruneau River Canyon, Idaho, with eight individual eruption-units (Figures 1 map, 3 picture, and 4 GVS). Many of the same CPT eruption-units have been identified in the Jarbidge Canyons a little over 20 km east [Bonnichsen and Citron, 1982]. The Brown's Bench escarpment, ~70 km east of Black Rock Escarpment (Figure 1 map), exposes 10 individual ignimbrite eruption-units [Knott and others, 2016b], but with thinner representatives of the correlative units. The Cassia Mountains, which lies ~100 km east (Figure 1 map), exposes ten individual ignimbrite eruption-units [Knott and others 2016a], with as many as six in a single unfaulted stratigraphic section. Successively younger units are exposed towards the East.

SR-type ignimbrites are characteristically large-volume, rhyolitic, metaluminous and ferroan, emplaced at high temperature, and have low $\delta^{18}O$ [Branney and others, 2008; Bindeman and Simakin, 2014]. They are intensely welded and devitrified, strongly rheomorphic, lack obvious glass shards and vitroclastic textures, and have upper autobreccias and associated laminated ashfall layers. Several SR-type ignimbrites are of a lithology that resembles massive or flow-laminated rhyolitic lavas [Branney and Kokelaar 1992] and are primarily distinguishable in the field from lavas by their thinly tapering distal margins and the absence of significant basal autobreccia. Most SR-Type ignimbrites have a thick central crystallized (lithoidal) zone and thinner upper and lower glassy (vitrophyre) marginal zones. The central

lithoidal zones typically pinch out distally towards the distal ignimbrite margins where the deposit is thin and so chilled rapidly.

Finn and others [2015] presented hysteresis, temperature-susceptibility, low-field induced magnetic anisotropy, thermal remanence anisotropy, and magnetic remanence measurements on a set of samples collected in a vertical profile through a typical SR-type ignimbrite (the Grey's Landing ignimbrite). From their results and a review of the literature, Finn and others [2015] concluded the magnetic remanence of SR-type strongly welded ignimbrites to be carried by large magmatic titanium-rich magnetite grains, post-magmatic small titanium-poor magnetite grains, as well as minor amounts of secondary titanohematite grains. The magnetic remanence and remanence anisotropy are dominantly carried by the titanium-poor magnetite grains, which nucleated in the volcanic glass at high temperatures after, and possibly during emplacement [Geissman and others, 1983; Wolff and others, 1989; Pioli and others, 2008; Finn and others, 2015]. The preferential nucleation of fine-grained magnetite along the margins of highly strained glass shards is thought to have caused the magnetic fabric to inherit the pre-existing strain fabric in the glass, a process largely dependent on cooling time. This is indicated by systematic variation of magnetic properties, including anisotropy, susceptibility, coercivity, dominant unblocking temperature, and remanence direction and strength, from the quickly chilled ignimbrite base to the more slowly cooled interior [Schlinger and others, 1988; Pioli and others, 2008; Finn and others, 2015]. Chemical alteration of magnetic minerals

during and possibly shortly after initial cooling may also have contributed to acquisition of remanence sub-parallel to the paleofield direction. In contrast, alteration and growth of new minerals long after emplacement will produce a detectable magnetic overprint in a different paleofield direction.

2. Paleomagnetism

2.1. Paleomagnetic Methods

Paleomagnetic cores were collected with a gasoline powered hand drill and oriented with a magnetic compass. Correction for the local magnetic field anomaly was made individually for each core using the observed azimuth of the sun. The central rheomorphic folded zone and devitrified interior was the preferred choice for collection of paleomagnetic samples. Stratigraphic sections containing multiple cooling units were sampled at the Black Rock and Brown's Bench escarpments and Cassia Mountains. At the Black Rock Escarpment sampling the entire stratigraphic succession entitled collecting from two locations that were less than 1 km apart (see supporting information Figures S1 and S2), but strata in the intervening exposed ground are non-faulted and lack any detectable changes in dip. Paleomagnetic sites from CPT III, V, VII, IX were collected at the western section (southern Black Rock escarpment), and those from CPT VII, IX, XII, XIII, and XVb were from the eastern section, which is a tributary drainage known as Hole in the Ground, used to access the Bruneau Canyon at the southern end of the Black Rock Escarpment.

Laboratory work was conducted at the University of California, Santa Cruz. Magnetic remanence measurement, automated progressive 3-axis static alternating field demagnetization up to 200 mT, and anhysteretic remanence magnetization (ARM) acquisition were performed on a 2G cryogenic magnetometer and Sapphire Instruments demagnetizer, respectively. ARM acquisition was performed for the purpose of measuring anhysteretic remanence anisotropy (AARM) using a 3 position approach similar to Gattacceca and Rochette [2002]. This method is also similar to the method of measuring the anisotropy of thermoremanent magnetization taken by Finn and others [2015] and the anisotropies of TRM and isothermal remanence taken by Stephenson and others [1986]. A detailed description of our AARM method can be found in the supporting information Document S1. For most samples we used the same AF range in which the best fit line to the demagnetization was determined (see column 3 from Table S2). Theoretically, this seems to be the most reasonable approach to measuring AARM with the intent of correcting remanence. However, we do not have any results that demonstrate this approach is best, and for at least one site we found this not to work well (CPT VII western sampling section). Discussion of remanence anisotropy and methods for correction of remanence, particularly with regard to CPT VII, will be the topic of a future paper. In this paper, we consider the AARM correction to improve the clustering of directions, but this does not necessarily fully restore them.

A customized sample handler and software (Morris et al., 2009) was used for automated progressive AF demagnetization. The 3-axis static alternating field demagnetization routine proposed by Finn and Coe [In Review] was used to efficiently remove remanence from samples whilst accounting for gyroremanence acquisition (See section 2.2.4). Fisher and McFadden Statistics (Fisher, 1953; McFadden and McElhinny, 1988) were used to calculate flow means, and principal component analysis (Kirschvink, 1980) was used to calculate the best-fit lines to demagnetization data. The paleomagnetic results from the Cassia Mountains region [Knott and others 2016a] and those for Brown's Bench were presented by [Knott and others 2016b]. We have reevaluated their flow mean directions (Table 1). Sample mean directions used for calculating flow mean directions can be found in the supporting information Tables S1-S3.

2.2. Mitigating pitfalls of the Paleomagnetic Analyses

2.2.1. Tectonic Rotation after Emplacement and Cooling

Any tectonic and volcano-tectonic rotation of ignimbrites after emplacement will rotate the TRM directions at that site. If a tectonic rotation of a single cooling unit differed between two locations it introduces a discrepancy for paleomagnetic correlation. Ignimbrites, however, may be deposited on gently sloping surfaces [Branney and Kokelaar 2002], and therefore 'correcting' a TRM direction simply by rotating the dip of bedding to horizontal may be inappropriate in some cases.

Fortunately, at the Black Rock, Brown's Bench and Cassia collection sections the dips of bedding are less than 5°. If the post-emplacement tilting at these sections was similar to each other (see Knott 2016a, b), then the discrepancy in directions between correlative units will be even less. Thus the potential tectonic discrepancy is usually substantially less than the angular separation between TRM directions of stratigraphically supradjacent flow-units. In addition, structural accounts [Knott et al. 2016a, b] report no strike-slip faults that would cause local vertical axis rotations.

To best avoid the potential distorting effects of tectonic rotations, we collected samples from structurally coherent (non-faulted) stratigraphic sections. Nonetheless, the potential for differential tilting of individual eruption-units within each unfaulted sections exists, and may have arisen by rotation of older units prior to deposition of younger units, as recently reported [Knott and others 2016a,b]. However, the excellent correlations of eruption-units near the base and top of each section suggest the effects of bedding rotations and tilting were minimal. We therefore make no attempt to correct for post-emplacement tectonic disturbance of the measured paleomagnetic direction.

2.2.2. Overprint of Primary Magnetization

SR-type ignimbrites commonly contain one or more distinguishable magnetic overprints, likely from chemical, thermal and viscous remagnetization long after initial cooling [see examples in non-SR-type ignimbrites; Reynolds 1977; Ellwood

and others, 1989]. Magnetic overprints are generally more pronounced in weakly magnetized samples, such as those from ignimbrites with transitional polarity, and in lithoidal rather than vitrophyre sub-lithologies. In addition, our results from numerous cooling units show that the ignimbrite top is more susceptible to magnetic overprinting then the center and base. Preferential chemical remagnetization of the upper parts of ignimbrites elsewhere has been demonstrated and explained in detail for the Huckleberry Ridge Tuff [Reynolds, 1977] and Fish Canyon Tuff [Ellwood and others, 1989]. For this reason, it is best to sample the basal vitrophyre and lithoidal center, although the basal vitrophyre is the most susceptible to large magnetic anisotropy, and so the lower part of the lithoidal zone should also be sampled (see section 2.2.3 below).

Figure 5 (overprint fig) shows zjiderveld and normalized magnetization plots, as well as equal area plots of the remanence vector difference directions for samples from CPT V, CPT IX, and CPT XII. Plotting remanence vector difference directions is useful to show the individual components of a progressive demagnetization containing multiple magnetic components. A common magnetic overprint direction seen in many ignimbrites (Fig.4) is coincident with the southern Idaho dipole direction (Dec=0°; Inc=60°); this suggests that it was acquired over a relatively long period of time. In addition, at least a couple of ignimbrites have acquired a thermochemical overprint direction close to the primary remanence direction of the overlying eruption-unit. This suggests that emplacement of the overlying ignimbrite

caused some reheating of and, possibly, mobilization of fluids within the upper part of the underlying ignimbrite. The magnetic remanence of CPT V and the upper part of CPT IX is complex, composed of 3 different magnetic components: (1) a high coercivity primary TRM, (2) a low coercivity overprint close to the dipole direction, and (3) an intermediate overprint close to the TRM direction of the overlying ignimbrite. Nonetheless, with careful demagnetization and component analysis, the direction of remanence acquired during primary cooling can almost always be found.

2.2.3. Anisotropy of Thermoremanent Magnetization

SR-type ignimbrites experience compaction strain and intense flow-related simple shear during emplacement, agglutination and rheomorphism [Branney and others, 2002]. This results in development of an intense mylonite-like flow fabric with associated isoclinal sheath folds [Branney and others, 2003; Andrews and Branney, 2011]. These fabrics are developed at temperatures above the glass transition and, therefore, prior to cooling below magnetic blocking temperatures of the magnetic minerals. This process produces large remanence anisotropy, and as a result, SR-type ignimbrites commonly have discrepant (often shallow) remanence directions rotated closer to the orientation of the shear (rheomorphic flow) direction or flattening compaction fabric [Gattacceca and Rochette, 2002; Finn and others, 2015]. After emplacement, devitrification begins in the ignimbrite center, and migrates toward the upper and lower margins. Finn and others [2015] show that crystal growth during

devitrification contributes to annealing of the magnetic fabric. In general, the lithoidal center is less anisotropic and a more reliable recorder of the paleofield direction than the glassy margins, although it is still capable of having magnetic anisotropy large enough to affect the remanence. Sampling variably oriented limbs of rheomorphic folds in the lithoidal zone of the ignimbrite, typically in the upper half of thick ignimbrite sheets, may help randomize the overall effect of anisotropy on the site mean remanence direction [Finn and others, 2015].

Measurement of the anisotropy of anhysteretic remanence (AARM) anisotropy was helpful in correcting for large TRM anisotropy in CPT VII and CPT XI (Figure 6. sample means). Correction using the AARM measurement improves the anisotropy-affected TRM direction, but does not guarantee complete correction back to the paleofield orientation. See the supporting information Document S1 for detailed description of the AARM method and results. Sub-blocking temperature rotation of magnetic grains has been proposed as a mechanism for shallowing remanence directions in 300 m-thick welded tuff in Nevada, as indicated by curvilinear demagnetization trends [Rosenbaum, 1986]. However, the curvilinear demagnetization trends in the SR-type ignimbrites in the present study appear to result from a strong relationship between unblocking temperature, coercivity, remanence anisotropy, and deflection of remanence (Figure 7, CPT VII sample) [Finn and others, In Prep]. Sub-blocking temperature rotation of grains probably does not occur in the more intensely welded and rheomorphic SR-type ignimbrites since the

remanence has no relationship with the steeper rheomorphic (F2) folds that develop after the compaction and flow fabric has already formed [Andrews and Branney, 2011; Giessman and others, 2010].

2.2.4. Gyroremanence

In addition to anisotropy of TRM, the fine grained magnetite in SR-type ignimbrites often suffers from acquisition of gyroremanence (GRM) during application of an alternating magnetic field (AF). GRM is a spurious component of magnetization that is acquired from application of an AF, and can hamper attempts to demagnetize rock samples with standard 3-axis static AF methods. We have found that detectable GRM is produced in most ignimbrite we have sampled, though it is more pronounced and problematic in weakly magnetized ignimbrite that cooled while the geomagnetic field was transitional (Figure 8 GRM).

The effect of GRM acquisition on a 3-axis AF demagnetization is dependent on the order of axes in which the AF is applied. Finn and Coe [In Review] present a new method for removing GRM that involves permutation of the AF axes order with progressively higher AF steps, and subsequent smoothing of the resultant demagnetization data. This laboratory procedure involves no extra remanence measurements or AF applications than a typical 3-axis demagnetization, and therefore, can be implemented with significant advantage as standard practice for

demagnetization of rocks. In contrast, the currently accepted method for excluding GRM [Dankers and Zijderveld 1981] requires two extra remanence measurements and AF applications at each progressively larger AF step, and thus is rarely performed on large batches of samples. We used the permuted demagnetization routine for all samples presented in this paper, and used the subsequent smoothing analysis to better component analyses for CPT XII and BBU-1. Using this method to remove GRM in BBU-1 improves the correlation with CPT V (Figure 9 site means; Table 1). We present the unsmoothed and smoothed demagnetization data and GRM corrected sample mean directions for both eruptive units in the supporting section Tables S3 and S4.

3. Stratigraphic Correlations

3.1 Introduction

SR-type ignimbrites in the central and southwestern Snake River Plain have limited variation in major element geochemistry, and their physical features observed in the field can vary more along strike than between subsequent eruptive units (e.g. compare ignimbrites CPT XI and the China Hill Member in Figure 3). The explosive mid-Miocene volcanism that produced the Cougar Point Tuff, however, captured reversed, normal, and transitional geomagnetic field polarities (Figure 10 CPT directions). For this reason, characterization of the stable thermoremanence of individual cooling units can be used as a powerful correlation tool [Grommé and others, 1972; Bogue and Coe, 1981; Hildreth and Mahood, 1985; Speranza and others, 2012; Ort and

others, 2013]. In addition to polarity, volcanic rocks typically record distinct directional changes in the geomagnetic secular field with a resolution of several hundred years [Hagstrum and Champion, 2002; Coe and others 2005], which is far better than the 1,000's to 100,000's of years resolution achieved with radiometric dating techniques for rocks of this age. Moreover, when the field is intermediate between normal and reversed polarity during excursions and reversals, the resolution can be as little as a century or less.

The diverse remanence directions measured in the Black Rock escarpment confirm that there are at least eight separate eruption units (Figure 10). Paleomagnetic evidence for distinguishing eruption units is robust even where intervening paleosols are not exposed (e.g. CPT XI and CPT XII). In some cases (e.g. the case of CPT XIII and CPT XVb), however, magnetic remanance was not able to distinguish between what have been considered to be separate eruption-units, because both units share a common field direction. In such cases, other evidence (e.g. field evidence such as intervening non-welded zones, vitrophyres, paleosols and sediments) should be assembled to provide the basis for an interpretation.

This powerful paleomagnetic technique has been an exceptionally useful aid in correlation of the CPT beyond the Bruneau Jarbidge region for two reasons (Figure 2 correlations). First, the CPT record a pattern of magnetic field directions that is uncommon in Earth's history (Figures 11 and 12 Direction and VGP). The directions

and corresponding virtual geomagnetic poles (Table 1) in stratigraphically adjacent flows are seldom repeated and include reversed and normal polarities and even intermediate states in two of the correlations. Second, there are multiple correlations between each ignimbrite section, and the probability that two eruption units are the same is greatly increased if other stratigraphically correlative units also correlate paleomagnetically because the probability that they could be different multiplies [Bogue and Coe, 1981]. The new stratigraphic correlations are supported by geochronologic dates (Table 2) and geochemistry (Figure 13 Geochem). Paleomagnetic sample mean directions are available in the supporting information Tables S1-S3, description of laboratory methods, results, and plots supporting our five new 40Ar-39Ar dates are presented in supporting information Figures S4-S8, Document S2, and Table S5, and description of the geochemical laboratory procedure is described in Document S3 and results shown in Table S6.

The CPT correlations proposed here are only from units exposed in the Black Rock escarpment, and do not include CPT X and CPT XVj which have been reported in the Jarbidge canyons farther to the east. CPT XV was originally mapped as one eruption-unit [Bonnichsen and Citron, 1982] and later divided into CPT XVb and CPT XVj for their exposures in the Bruneau (Black Rock escarpment) and Jarbidge Canyons, respectively [Perkins and others, 1995]. Several younger ignimbrites at Brown's Bench escarpment and in the Cassia Hills [Knott et al. 2016a,b]do not have correlatives within the CPT and so are not discussed in this paper.

3.2 Application of the Paleomagnetic Correlation Method of Bogue and Coe (1981)

We used a statistical paleomagnetic correlation method described by Bogue and Coe [1981] to evaluate the probabilities of whether the magnetic directions of potentially correlative deposits and sequences of deposits were obtained by simultaneous (Ps) or random (Pr) samplings of the magnetic field. Ps is the probability that the site mean directions could be as different as they are and still be erupted at the same time. Pr is the probability that the site mean directions could be as close to each other as they are and still be 'random' samplings of the geomagnetic field. The ratio of Ps to Pr is the most direct measure of whether two ignimbrites were emplaced at the same instant (Table 3). For example, a Ps/Pr ratio of 10 indicates a 10 times larger probability that the magnetic directions of the two ignimbrites were acquired at the same time rather than being spaced apart over a timespan that is long compared to secular variation. The Ps/Pr ratios for individual pairs of correlations are multiplied when considering the cumulative probability that two sections are correlative. The cumulative ratio of probabilities (Ps/Pr) for correlation between the Black Rock and Brown's Bench escarpments, and between the Black Rock Escarpment and Cassia Mountains are 3.8x109 and 4.1x104, respectively. These extremely large values demonstrate the remarkable strength of the paleomagnetic correlations.

The angular standard deviation of the mean due to within-site scatter of sample directions, and uncertainty estimates for systematic sources of error are needed to evaluate the true uncertianty in the ignimbrite mean directions (Table 4). Potential sources of systematic error that don't appear in the scattering of sample-mean directions include effects from magnetic field anomalies, post-emplacement tilting, uncorrected effects of anisotropy, and any unremoved overprint component. The angular standard deviation of the site-mean direction (S) used for estimating correlation probabilities is the square root of the sum of the squares of the estimated values from all the potential systematic errors, Si, and from the scatter of sample directions within the site (Table 4). The appropriate precision parameter (k) that best describes secular variation of Earth's paleomagnetic direction at the time and region of the eruptions is 22.6. This value was obtained from averaging paleomagnetic directions from 108 mid to early Miocene basalt lavas in the nearby Oregon Plateau [Jarboe and others, 2011]. The uniform distribution (k = 0), however, was used for ignimbrites CPT V and CPT IX since the magnetic field does not fit a fisher distribution while in a transitional direction

3.3 Discussion of Paleomagnetic Site-Mean Directions and Correlations

3.3.1 'CPT V' and 'BBU-1' units

The stratigraphically lowest correlation proposed here, is between ignimbrite cooling unit CPT V at Black Rock escarpment (Figure 3 pictures), with a rather poorly

exposed, silicified, lava-like lithoidal rhyolite seen at the base of Brown's Bench escarpment, 70 km further East (Figure 1 map), referred to as 'BBU-1' by Bonnichsen and others [2008]. Both units record transitional geomagnetic polarity with a virtual geomagnetic pole (VGP) position located 55° from the rotation axis (Figure 12 VGPs). This is a very unusual orientation for the geomagnetic field, yet the directions are only 4.8° apart extremely unlikely to be this close together if they were erupted independently at different times - a chance of about one in a thousand by the method of Bogue and Coe (1981). In addition, the field direction differs from those of most other ignimbrites in the central Snake River area (Knott et al. 2016a,b). Their Ps/Pr ratio is over 400 (Table 3).

Ignimbrite CPT V is a thin (~5 m) vitrophyric massive tuff at the sample locality on the south end of the Black Rock escarpment. Because it is thin, it probably does not have a large magnetic anisotropy, and because it lacks steep flow-banding or upright folds, any significant magnetic anisotropy would be sub-horizontal and at a high angle to the steep remanence direction. Because of this angle, the anisotropy could affect the intensity of remanence, but not its direction. The vitrophyric lithology is more resistant to magnetic overprinting and GRM than is the lithoidal lithology because SR-type vitrophyres are generally more strongly magnetic than SR-type lithoidal tuffs [Finn et al. 2015], a significant advantage in this case because the geomagnetic field is unusually weak during polarity transitions. CPT V has two overprint directions that are successfully removed with magnetic cleaning (Figure 5

Overprint). The low coercivity overprint is coincident with the expected direction of the dipole field, and the intermediate coercivity overprint matches the magnetic direction of the overlying CPT VII, which indicates that it acquired a thermochemical overprint during the subsequent eruption.

Samples from ignimbrite 'BBU-1' are weakly magnetized and experience significant GRM acquisition during 3-axis AF demagnetization. Corrections for GRM were undertaken using the laboratory method and subsequent analysis proposed by Finn and Coe [In Review]. The corrected flow mean remanence direction had reduced error and was closer to the CPT V remanence direction after GRM correction (Figure 9 GRM site means). The correlation is further supported by XRF whole-rock compositions, in that ignimbrites 'CPT V' and the Brown's Bench Member both are characterized by higher silica contents (>76 wt.%) compared to many other central Snake River Plain ignimbrites, and low TiO2 (≤0.3 wt.%) and Sr (≤40 ppm). On a Th/Nb vs. Rb/Sr plot samples of CPT V and 'BBU-1' fall in a separate field that does not overlap with the fields of other units (purple, on Figure 13A)

3.3.2. CPT VII and Brown's Bench Member of the Rogerson Formation

The large rhyolitic explosive eruption that deposited the 11.852 ± 0.009 Ma Brown's Bench Member, Idaho, happened while Earth's magnetic field was reversed [Knott and others, 2016b]. The Brown's Bench Member (formerly 'BBU-3' of Bonnichsen

et al. 2008) is a 90 m-thick lava-like outflow ignimbrite cooling-unit in the Rogerson Formation characterized by a stepped erosional profile and compositionally distinct population of augites and two pigeonites [Knott and others, 2016b].

The site-mean magnetic directions for CPT VII at Black Rock Escarpment, and for the Brown's Bench Member, ~70 km to the East, are just 7.9° apart and the Ps/Pr ratio is 3.8 (Table 3). The Corral Creek Member, an ignimbrite cooling unit that directly underlies the Brown's Bench Member, also records a reversed magnetic pole position, but its site-mean direction is more than twice as far from that of CPT VII, and the resulting Ps/Pr ratio is 200 times smaller. Moreover, our new high precision geochronologic dates (Figure 2 Correlation and Table 2) for CPT VII (11.855 ± 0.006 Ma) and the Brown's Bench Member (11.852 ± 0.009 Ma) strongly support the correlation we propose. This interpretation is also supported by whole-rock geochemistry, in that both CPT VII and the Brown's Bench Member share some distinctive features: Rb/Sr ratios are low (<4), and the SiO2 (72.4-73.0 wt.%) and TiO2 values (~0.52 wt.%) are lower than in many other central Snake River Plain ignimbrites (Orange in Figure 13A). In terms of mineralogy, both CPT VII and Brown's Bench Member contain three fairly distinctive pigeonite populations (Figure 13B). Two of these three pyroxene compositions also occur in CPT III, and the pyroxene population differs significantly from that of CPT IV.

Ignimbrite cooling unit CPT VII was sampled at two locations (<1 km apart) at the Black Rock Escarpment (Figure 1 map) and there is a moderate discrepancy between the two remanence directions (Figure 6 sample means). The magnetic anisotropy was generally large for many samples and the anhysteretic remanence anisotropy (AARM) corrections only partly resolved this discrepancy. The magnetic anisotropy and remanence in the lithoidal samples are held by grains that have a low coercivity. This is particularly true for the westernmost sampling location on the southern end of the Black Rock escarpment. Having so much of the remanence focused in this highly anisotropic low coercivity range (Figure 7 CPT VII) complicates the AARM correction. Since this correction is only partly successful for this ignimbrite, we excluded the most anisotropic samples and calculated a flow mean direction using just the samples that have a P (K1/K3) value of less than 1.5. In contrast to CPT VII, samples of the Brown's Bench Member have well clustered paleomagnetic directions and low remanence anisotropy, suggesting the site mean magnetic direction is of high quality.

3.3.3. CPT IX and the Black Canyon Member of the Rogerson Formation

The CPT IX and the Black Canyon Member (Knott and others, 2016a; formerly 'BBU-4 & BBU-5' of Bonnichsen et al. 2008) erupted while Earth's magnetic field had a transitional direction with VGP almost 65° from the rotation axis (Figure 12 VGPs). Yet their site-mean directions are not significantly different (only 2° apart),

which when combined with their unusual direction, makes for a very strong paleomagnetic correlation (Ps/Pr ratio = 3085.5, Table 3). Supporting this correlation, CPT IX and the Black Canyon Member also have similar trace-element chemistry (Figure 13A geochem) and indistinguishable pigeonite compositions (Figure 13B), although the compositionally distinct augites present in the Black Canyon Member were not reported from CPT IX.

We have not measured magnetic anisotropy of CPT IX and the Black Canyon Member, we suspect that it has had little effect because the sample directions are tightly clustered and the site means agree well. CPT IX and the Black Canyon Member both have significantly more magnetic overprinting in their upper parts (Figure 5 Overprint). In consideration of these properties indicating remagnetization problems, we do not present any results from samples collected from the tops of CPT IX and the Black Canyon Member, nor use them for determination of the ignimbrite mean directions. We have collected paleomagnetic sites stratigraphically lower within each ignimbrite that are far less affected by magnetic overprinting.

3.3.4. CPT XI, the China Hill Member (Rogerson Formation), and the Magpie Basin Member (Cassia Formation)

The CPT XI eruption occurred during a time when Earth's magnetic field was reversed, and its VGP~30° away from the rotation axis is relatively unusual. The

magnetic directions of the China Hill Member of the Rogerson Formation at Brown's Bench (Figure 1; former BBU-6 of Bonnichsen 2008), and of the Magpie Basin Member of the Cassia Formation, are 8.6° and 4.4° from that of CPT XI, respectively, and 9.4 degrees from each other. The Ps/Pr ratios describing the correlation of CPT XI with Magpie and China Hill are 100.1 and 4.6, respectively (Table 3). Available 40Ar-39Ar geochronologic dates of sanidine crystals from CPT XI (11.35 ± 0.07 Ma; Bonnichsen and others 2008) and from the Magpie Basin Member (11.337 ± 0.008 Ma; Knott and others, 2016a] agree within error. We present a new weighted mean sanidine 40Ar-39Ar age of 11.305 ± 0.016 Ma for the China Hill Member (Table 2). Although this age is slightly younger the correlating inverse isochron age of 11.324 ± 0.020 Ma is indistinguishable from the published ages for the Magpie Basin Member and CPT XI unit.

This newly correlated ignimbrite is thickest at the Black Rock Escarpment (CPT XI), and where we also have measured the largest AARM. In contrast to CPT VII, many of the anisotropic samples from this location have remanence contained at higher coercivities, and the AARM corrections (as described above) work very well in improving the paleomagnetic correlation. This is likely because the remanence resides in a coercivity range where the AARM is easily measured. The AARM of CPT XI samples, in contrast to that of CPT VII, seems to be able to completely correct the most anisotropic samples from this flow and so we do not exclude samples based on P.

The China Hill and Magpie Basin members have a much smaller, though not insignificant degree of anisotropy. We measured anisotropy for most samples from the two locations but not all samples. Unfortunately, we destroyed many samples for geochemical analysis before realizing that magnetic anisotropy would present a problem. However, to be consistent we include all samples in calculation of the ignimbrite mean directions for each location. These ignimbrite mean directions do not change too much if uncorrected samples are excluded since they probably had only moderate to low anisotropy.

Whole-rock geochemistry lends support to the correlation between CPT XI, the China Hill Member, and the Magpie Basin Member all have unusually low TiO2 contents (<0.26 wt%) and they occupy the same field on the Th/Nb vs. Rb/Rr plot (Figure 13A Geochem), with Rb/Sr ratios lying in the range of 5.2 – 9.5. In contrast to this, the underlying Black Canyon Member dsiplays Rb/Sr ratios ≤5.2. Pyroxene compositions are also distinct from those of underlying units, with higher (>38 wt.%) FeO (pigeonites >38wt.%; augites >24wt.%) and lower MgO contents (6-7 wt.%; Figure 13B Geochem).

A correlation between CPT XI and the Black Canyon Member of the Rogerson Formation (former BBU-5 of Bonnichsen 2008) has been proposed [Ellis and others, 2012]. However, this proposed correlation is inconsistent with our results that show

the paleomagnetic directions of CPT XI and the Black Canyon Member to be very far apart from each other. This is in contrast to the close proximity of magnetic directions between our proposed correlatives CPT XI, and the China Hill and Magpie Basin members. Moreover, the compositions of both pigeonites and augites within the Magpie Basin Member are significantly different to those in the Black Canyon Member (Figure 13B Geochem). At Brown's Bench Escarpment, the China Hill Member underlies the Black Canyon Member (Figures 2 Correlations and 3 Pictures), for which Ellis and others [2012] report an 40Ar-39Ar date of 11.41 ± 0.08 Ma (recalculated to Rivera et al., 2011). This age is much closer to our new China Hill Member 40Ar-39Ar date of 11.305 ± 0.016 Ma than it is to ages derived from samples collected from the base and top of the Black Canyon Member. It's possible that Ellis and others [2012] unknowingly sampled the China Hill Member instead of the Black Canyon Member.

3.3.5. Correlations to CPT XIII and CPT XVb

CPT XIII and CPT XVb share a similar steep normal polarity magnetic direction, though they are generally regarded to be separate eruption-units (e.g. Bonnichsen and Citron 1982; Ellis and others 2012]. We know from radiometric dating that the correlatives at Brown's Bench and the Cassia mountains are separate cooling units spaced in time by ~0.35 my (Bonnichsen and others 2008; Ellis and others 2012; Figure 2 Correlations and Table 2). Similar to CPT V, the steep remanence direction

is probably not greatly affected by anisotropy because of the high angle with the sub-horizontal fabric.

Although the direction they share is not particularly unlikely for the geomagnetic field, the repetition of it twice spaced out so far in time is very unlikely. The Ps/Pr ratios from the cumulative correlation of CPT XIII and CPT XVb to the Browns Bench escarpment and the Cassia Mountains are 172 and 413, respectively. CPT XIII and its correlatives also share similarities in plagioclase and augite compositions [Ellis and others 2012] and all have radiometric dates that are indistinguishable within error (Figure 2). CPT XVb and its correlatives share similar clinopyroxene and whole rock compositions, as well as physical characteristics (Perkins and others 1995; Ellis and others 2012]. Although CPT XVb has not been dated directly, it's correlatives at the Brown's Bench escarpment and Cassia Mountains have indistinguishable radiometric dates (Figure 2 Correlations). The combined paleomagnetic, geochronologic, and geochemical evidence, physical characteristics, and relative stratigraphic positions adjacent to other correlative ignimbrite, support the previous suggestion by Ellis and others [2012] that these six widely spaced deposits represent two eruptions.

4. New Cougar Point Tuff Eruption Area and Volume Estimates

4.1. Cougar Point Tuff Volume Estimation Methods and Results

Individual CPT ignimbrite sheets thicken northward toward their inferred source in the southern Snake River Plain where they are concealed by younger basalts [Bonnichsen and Citron 1982]. They also likely extend farther south beyond the Snake River Plain along paleovalleys, have thick caldera fills of unknown dimensions and widely dispersed ash fall components. CPT thickness distributions are poorly known as they are primarily exposed in widely spaced canyons and escarpments. For the reasons listed above, individual CPT eruption volumes can only be estimated with an accuracy slightly better than an order of magnitude. Method 2 from Ellis and others [2012] is used here for volume estimation. This procedure involves: 1) Estimation of the areal extent; 2) Multiply the area by the average thickness; 3) Double the volume to account for caldera infill; 4) Ignore the ash fall component.

Figure 14 shows the general areas of deposition for CPT units exposed in the Black Rock and Brown's Bench escarpments (CPT V, VII, and IX) and those that occur farther east to the Cassia Mountains (CPT XI, XIII, and XVb). These areal extents of 5,000 km2 and 10,000 km2, respectively, are rough estimates and should be treated as tentative. The average thicknesses used for each CPT is taken as the average of the minimum and maximum observed thicknesses (min.-max., avg.); CPT V (10-40 m, 30 m); CPT VII (40-100 m, 70 m), CPT XI (20-100 m, 60m), CPT XIII (20-100 m, 60), CPT XVb (20-100 m, 60 m). Following the method of Ellis and others [2012],

minimum volume estimates of CPT V is 300 km3, CPT VII is 700 km3, CPT IX is 400 km3, and CPT XI, XIII, and XVb are 1200 km3.

4.2. Areal Extent of the Newly Expanded Cougar Point Tuff

South of the towns of Jackpot, Jarbidge, and Rowland Nevada, the SRP Miocene welded tuffs are discontinuously covered by late Miocene sediments [Sharp 1939; Bushnell 1967] and onlap the 15-17 Ma pre-Snake River Plain Jarbidge Rhyolite, Jurassic to Cretaceous granites, as well as marine strata of mostly Permian and Pennsylvanian age [Bonnichsen and Citron 1982; Coats et al., 1987]. The southern extent of the CPT and its correlatives are drawn conservatively in figure 14 (areas) along the southern most continuous exposure of SRP Tuffs [Coats et al., 1987]. There are discontinuous exposures of SRP tuffs farther south in northern Nevada, but there are fewer individual cooling units and direct correlations are unknown. The western margin of the Bruneau-Jarbidge eruptive center is thought to be marked by the Grasmere escarpment, where at least three Cougar Point Tuffs are exposed (Figure 14 areas). The youngest of the three, the Grasmere escarpment ignimbrite, is thought to be correlative to CPT XI based on age, geochemistry, and magnetic polarity [Bonnichsen et al., 2008]. However, there is not enough evidence to include this deposit as part of the same eruption that produced the CPT XI, and for this reason the Grasmere escarpment is used here as a western border of all the CPT units.

The CPT units that are exposed in Brown's Bench escarpment are also inferred to underlay the immediately adjacent low lying Rogerson Graben to the east, and those that occur even farther east are inferred to be present throughout the Cassia Mountains. This may be a small over estimate for CPT XI, which likely only occur as an ash fall deposit in the far eastern Cassia Mountains. The extent of the CPT units to the north in the Snake River, where they are concealed by younger basalt flows, is by far the boundary with the largest uncertainty. The northern margin is conservatively extended into the plain in figure 14 (areas), though the exact location of the northern extent of most CPT eruptions is entirely unknown. It is likely that some of the CPT units are present on the far northern margin of the Snake River Plain, which will be the focus of a future paper. This present paper should be considered more of an update of our continued effort to correlate and expand the eight individual CPT eruptions exposed in the Black Rock escarpment.

5. Discussion and Conclusion

The magnetic remanence preserved in strongly welded and rheomorphic ignimbrites is a powerful tool for (A) distinguishing between the products of separate explosive volcanic eruptions, and (B) for stratigraphic correlation of defined eruption-units. The technique is best employed together with field data, whole-rock and mineral chemistry, and radiometric dating. However, because the time-spans represented by error-bars in even high-resolution radiometric dating, as presented in this paper, is of sufficient duration to host more than one large explosive eruption, radiometric dating

can be more readily employed to disprove a volcano-stratigraphic correlation, rather than to establish one. Thus, characterizing of geomagnetic secular variation through remanence studies is the only method with temporal resolution (1-3 centuries) capable of determining with confidence if multiple ignimbrite deposits were simultaneously emplaced. The combined use of these temporal constraints with geochemical characterization addresses the two fundamental criteria used for correlating deposits from individual eruption events: They share the same magma source, and were emplaced simultaneously. Using these techniques we have demonstrated, with confidence, that most of the Cougar Point Tuff extends occur in the Brown's Bench escarpment and some even farther east to the Cassia Mountains. The correlations presented here demonstrate that mid-Miocene Yellowstone Hotspot eruptions were much larger and infrequent than previously thought.

We propose a new protocol to mitigate potential pitfalls that could yield incorrect determinations of magnetic remanence directions in SR-type ignimbrites, and which we expect will be helpful in paleomagnetic studies of partly glassy silicic lavas and rheomorphic ignimbrites elsewhere. We recommend collecting paleomagnetic samples at two sites from each cooling unit: one from the stable and more strongly magnetized basal vitrophyre, which is more resistant to chemical overprinting, and the other from the rheomorphically folded devitrified central part of the ignimbrite, as this is least effected by magnetic anisotropy and relatively far from the CRM prone ignimbrite top. The measurement of anhysteretic remanence anisotropy can be used to

detect and at least partly correct the effects of large thermal remanence anisotropy, and a new protocol for 3-axis AF demagnetization [Finn and Coe, In Review] can be used to avoid potentially interfering effects of gyroremanence (GRM). This protocol takes no extra time or effort, and therefore should be implemented as a matter of course. If GRM is then found to be problematic after the demagnetization experiment, a subsequent smoothing analysis may be used to remove the unwanted GRM effects (e.g. as was applied to BBU-1 and CPT XII).

6. Acknowledgements

Expenses for this work were covered by the Natural Environment Research Council (NERC) Grant NE/G005372/1 awarded to Michael Branney. The salary and school fees for the first author were covered in part by a National Science Foundation (NSF) grant (EAR 1250444) awarded to X. Zhao. Please contact the first author via email at dfinn@ucsc.edu for data requests and other questions. We also would like to thank Grant Rhea-Downing for his assistance with paleomagnetic field sampling and discussion on magnetic anisotropy.

7. References

Andrews, G. D., & Branney, M. J. (2011). Emplacement and rheomorphic deformation of a large, lava-like rhyolitic ignimbrite: Grey's Landing, southern Idaho. Geological Society of America Bulletin, 123(3-4), 725-743.

Armstrong, R. H. L., Leeman, W. P., & Malde, H. E. (1975). K-Ar dating quaternary and Neogene volcanic rocks of the Snake River Plain, Idaho. Am. J. Sci.;(United States), 275(3).

Armstrong, R. L., Harakal, J. E., & Neill, W. M. (1980). K-Ar dating of Snake River Plain (Idaho) volcanic rocks—new results: Isochron.

Bindeman I.N., & Simakin, A.G. (2014). Rhyolites–Hard to produce, but easy to recycle and sequester: Integrating microgeochemical observations and numerical models. Geospohere 10 doi 10.1130/GESOO969.1

Branney, M. J., & Kokelaar, P. (1992). A reappraisal of ignimbrite emplacement: progressive aggradation and changes from particulate to non-particulate flow during emplacement of high-grade ignimbrite. Bulletin of Volcanology, 54(6), 504-520.

Branney, M.J., Barry T.L., Godcheaux, M. 2004. Sheathfolds in rheomorphic ignimbrites. Bulletin Volcanology, 66: 485-491

Branney, M. J., Bonnichsen, B., Andrews, G. D. M., Ellis, B., Barry, T. L., & McCurry, M. (2008). 'Snake River (SR)-type'volcanism at the Yellowstone hotspot track: distinctive products from unusual, high-temperature silicic super-eruptions. Bulletin of Volcanology, 70(3), 293-314.

Bonnichsen, B., & Citron, G. P. (1982). The Cougar Point tuff, southwestern idaho and vicinity. Cenozoic Geology of Idaho: Idaho Bureau of Mines and Geology Bulletin, 26, 255-281.

Bonnichsen, B., Leeman, W. P., Honjo, N., McIntosh, W. C., & Godchaux, M. M. (2008). Miocene silicic volcanism in southwestern Idaho: geochronology, geochemistry, and evolution of the central Snake River Plain. Bulletin of Volcanology, 70(3), 315-342.

Bogue, S. W., & Coe, R. S. (1981). Paleomagnetic correlation of Columbia River Basalt flows using secular variation. J. Geophys. Res, 86, 11883-11897.

Coe, R. S., Stock, G. M., Lyons, J. J., Beitler, B., & Bowen, G. J. (2005). Yellowstone hotspot volcanism in California? A paleomagnetic test of the Lovejoy flood basalt hypothesis. Geology, 33(9), 697-700.

Dankers, P. H. M., & Zijderveld, J. D. A. (1981). Alternating field demagnetization of rocks, and the problem of gyromagnetic remanence. Earth and Planetary Science Letters, 53(1), 89-92.

Ellis, B. S., Branney, M. J., Barry, T. L., Barfod, D., Bindeman, I., Wolff, J. A., & Bonnichsen, B. (2012). Geochemical correlation of three large-volume ignimbrites from the Yellowstone hotspot track, Idaho, USA. Bulletin of volcanology, 74(1), 261-277.

Ellwood, B. B., Stormer, J. C., & Whitney, J. A. (1989). Fish Canyon Tuff, Colorado: the problem of two magnetic polarities in a single tuff. Physics of the earth and planetary interiors, 56(3), 329-336.

Finn, D. R., Coe, R. S., Kelly, H., Branney, M., Knott, T., & Reichow, M. (2015). Magnetic anisotropy in rhyolitic ignimbrite, Snake River Plain: implications for using remanent magnetism of volcanic rocks for correlation, paleomagnetic studies and geological reconstructions. Journal of Geophysical Research: Solid Earth.

Fisher, R.A (1953), Dispersion on a sphere: Royal Society of London Proceedings, v. 217, ser. A, p. 295–305.

Gattacceca, J., & P. Rochette (2002). Pseudopaleosecular variation due to remanence anisotropy in a pyroclastic flow succession. Geophysical research letters, 29(8), doi:10.1029/2002GL014697.

Geissman, J. W., N. G. Newberry, and D. R. Peacor (1983). Discrete single-domain and pseudo-single-domain titanomagnetite particles in silicic glass of an ash-flow tuff. Canadian Journal of Earth Sciences, 20(2), 334-338.

Geissman, J. W., D. Holm, S. S. Harlan, and G. F. Embree (2010), Rapid, high-temperature formation of large-scale rheomorphic structures in the 2.06 Ma Huckleberry Ridge Tuff, Idaho, USA, Geology, 38, 263–266, doi:10.1130/ G30492.1.

Grommé, C. S., E. H. McKee, M. C. & Blake Jr. (1972), Paleomagnetic correlations and potassium argon dating of middle Tertiary ashflow sheets in the eastern Great Basin, Nevada and Utah, Geol. Soc. Am. Bull., 83(6), 1619-1638

Hagstrum, J. T., & Champion, D. E. (2002). A Holocene paleosecular variation record from 14C-dated volcanic rocks in western North America. Journal of Geophysical Research: Solid Earth (1978–2012), 107(B1), EPM-8.

Hildreth, W., & Mahood, G.A. (1985), Correlation of ash-flow tuffs: Geological Society of America Bulletin, v. 96, p. 968-974.

Kirschvink, J. L. (1980). The least-squares line and plane and the analysis of palaeomagnetic data. Geophysical Journal International, 62(3), 699-718.

Knott, T. R., Branney, M. J., Reichow, M. K., Finn, D. R., Coe, R. S., Storey, M., ... & McCurry, M. (2016a). Mid-Miocene record of large-scale Snake River− type explosive volcanism and associated subsidence on the Yellowstone hotspot track: The Cassia Formation of Idaho, USA. Geological Society of America Bulletin, B31324-1.

Knott, T.R., Reichow, M.K., Branney, M.J., Finn, D.R., Coe, R.S., Storey, M., Bonnichsen, B. (2016b) Rhyolitic explosive eruptions and related crustal subsidence on the Yellowstone hotspot-track: The Rogerson Formation (Mid-Miocene), central Snake River Plain, USA. Bulletin of Volcanology (in press).

Manley, C. R., & McIntosh, W. C. (2002). The Juniper Mountain volcanic center, Owyhee County, southwestern Idaho: Age relations and physical volcanology. Tectonic and magmatic evolution of the Snake River plain volcanic province: Idaho Geological Survey Bulletin, 30, 205-227.

McFadden, P. L., & McElhinny, M. W. (1988). The combined analysis of remagnetization circles and direct observations in palaeomagnetism. Earth and Planetary Science Letters, 87(1), 161-172.

Morgan, L. A., & McIntosh, W. C. (2005). Timing and development of the Heise volcanic field, Snake River Plain, Idaho, western USA. Geological Society of America Bulletin, 117(3-4), 288-306.

Morris, E.R., W. Schillinger, R. S. Coe, C. J. Pluhar, N. A. Jarboe (2009), Automating the 2G superconducting rock magnetometer for single-solenoid alternating field demagnetization. G-cubed, 10. doi:10.1029/2008GC002289.

Ort, M. H., S. L. de Silva, N. Jiménez C., B. R. Jicha, and B. S. Singer (2013), Correlation of ignimbrites using characteristic remanent magnetization and anisotropy of magnetic susceptibility, Central Andes, Bolivia, Geochem. Geophys. Geosyst., 14, 141–157, doi:10.1029/2012GC004276.

Perkins, M. E., Nash, W. P., Brown, F. H., & Fleck, R. J. (1995). Fallout tuffs of Trapper Creek, Idaho—a record of Miocene explosive volcanism in the Snake River Plain volcanic province. Geological Society of America Bulletin, 107(12), 1484-1506.

Pierce, K. L., & Morgan, L. A. (1992). The track of the Yellowstone hot spot: Volcanism, faulting, and uplift. Geological Society of America Memoirs, 179, 1-54.

Pioli, L., Lanza, R., Ort, M., and Rosi, M. (2008). Magnetic fabric, welding texture and strain fabric in the Nuraxi Tuff, Sardinia, Italy. Bulletin of Volcanology, 70(9), 1123-1137.

Reynolds, R. L. (1977), Paleomagnetism of the welded tuffs of the Yellowstone group, J. Geophys. Res.., 82, 3677-3693

Rosenbaum, J. G. (1986). Paleomagnetic directional dispersion produced by plastic deformation in a thick Miocene welded tuff, southern Nevada: implications for welding temperatures. Journal of Geophysical Research: Solid Earth (1978–2012), 91(B12), 12817-12834.

Speranza F., A. Di Chiara, and S. G. Rotolo (2012), Correlation of welded ignimbrites on Pantelleria (Strait of Sicily) using paleomagnetism, Bull. Volcanol., 74, 341–357, doi:10.1007/s00445-011-0521-9.

Stephenson, A., Sadikun, S., & Potter, D. K. (1986). A theoretical and experimental comparison of the anisotropies of magnetic susceptibility and remanence in rocks and minerals. Geophysical Journal International, 84(1), 185-200.

Wolff, J. A., B. B. Ellwood, and S. D. Sachs (1989). Anisotropy of magnetic susceptibility in welded tuffs: application to a welded-tuff dyke in the Tertiary Trans-Pecos Texas volcanic province, USA. Bulletin of volcanology, 51(4), 299-310.

Table Captions

Table 1: shows the ignimbrite flow mean paleomagnetic directions for the Black Rock and Brown's Bench escarpments and Cassia Mountains regions of the southern Snake River Plain. The first column shows the ignimbrite name (e.g. CPT XI). An "a-" and "g-" in front of the name (e.g. ac-CPT XI) indicates the direction was corrected using the anhysteretic remanence anisotropy (AARM) tensor and had gyroremanence removed using the SI method, respectively. An "-E", "-W", and "-B" at the end of the Cougar Point Tuff names indicate if the flow mean was obtained from the eastern (Hole in the Ground) or westernmost (southern Black Rock escarpment) subsections of the Black Rock escarpment, or from both combined, respectively (e.g. CPT IX-E). For the correlation shown in Figure 2, we always use the anisotropy and gyroremanence corrected direction if available, as well as the directions that combine results from both subsections. The second column (n/N) shows the number of sample directions used for the site mean calculation (n) over the number of samples we considered using (N). Sample directions did not count toward the total number considered (N) if they were excluded because they were vitrophyre samples that are more likely to be anisotropic. Columns 3-6 show the declination (Dec), inclination (Inc), precision parameter (k), and radius of the 95% confidence cone (a95) calculated for each flow mean , respectively. Columns 7 and 8 show the latitude and longitude of the sampling site and columns 9-11 show the latitude, longitude, and 95% confidence cone of the virtual geomagnetic pole (VGP). East is positive for all longitude values.

Table 2: Summary of radio-isotopic dates for members of the Cougar Point Tuff, Rogerson and Cassia Formations with sample locations, material type, and method used. Note: All argon ages are relative to sanidine feldspar standard FCs at 28.172 Ma ± 0.028 Ma (Rivera et al., 2011), and reported with 2s uncertainties.

Table 3: Ignimbrite by ignimbrite correlation statistics of the Cougar Point Tuffs, following the method of Bogue and Coe (1981); k is the precision parameter for the estimated uncertainty in the ignimbrite mean direction from table 4. δ is the angular distance between the paleomagnetic and axial dipole direction; α is the angle between the two paleomagnetic directions; Pr is the probability of the random hypothesis – that the two ignimbrites could have been erupted independently at times far apart compared to the time scale of paleomagnetic secular variation and yet have directions as close to each other as they are; Ps is the probability of the simultaneous hypothesis – that the two ignimbrites could have been emplaced at the same time and yet have directions that are as far apart from each other as they are; Ps/Pr is the probability ratio indicates most directly the relative likelihood that the two ignimbrites erupted at the same time rather than have similar directions by chance; 'Cum Ps/Pr' is the cumulative probability for considerations of multiple correlations, starting with the youngest and sequentially including older ignimbrites.

Table 4: Errors are shown related to the uncertainty involved in determination on flow mean remanence directions. k is the Fisher (1953) precision parameter describing the within-site dispersion of sample directions and S_W is the associated angular standard deviation of the mean; S_T, S_A, and S_O are the assigned angular standard deviations of the flow mean direction due to post-emplacement tectonic tilts and rotations, magnetic field anomalies, uncorrected magnetic anisotropy, and unremoved magnetic overprints, respectively, and S_B is the combined error due to the four uncertainties assuming they are independent; k_B is the precision parameter associated with S_B.

Figure Captions

Figure 1: Map of the Snake River Plain showing the sampling locations. The inset map shows the southern 2/3 of Idaho with the approximate locations of putative eruptive centers (red dashed circles) and location of the enlarged area (black rectangle) indicated. The shaded red overlay shows the currently known extent of the Cougar Point Tuff (CPT) eruptions. The Grasmere Escarpment ignimbrite was included in this areal extent because it is thought to be part of the CPT, though the exact correlation to CPT units with designated roman numerals remains uncertain.

Figure 2: Correlations between the Black Rock and Brown's Bench escarpments, and the Cassia Mountains in southern Idaho. Thin black connecting lines highlight proposed correlations by Ellis and others [2012]. Radiometric age data: 1 this study, 2

Bonnichsen and others [2008], 3 Knott and others [2016a], 4 Knott and others [2016b], and 5 Ellis and others [2012]. All argon ages have been recalculated to an age of 28.172 Ma for the Fish Canyon Tuff standard age [Rivera and others 2011]. Note: We consider remanence directions that are pointed southward and down to be transitional.

Figure 3: Photo of the Brown's Bench and Black Rock Escarpment sampling locations (see figure 1 map) with the units labeled and color coded based on the proposed correlations. Note: two names are given for each unit in the Brown's Bench escarpment following the new nomenclature by Knott and others [2016b] and that initially proposed by Bonnichsen and others [2008] (e.g. BBU-6).

Figure 4: Generalized vertical stratigraphy of the Cougar Point Tuff Formation showing the physical features of each of the eight members at the Black Rock Escarpment in southern Idaho. Argon ages: 1this study; 2Bonnichsen and others 2008; all recalculated to Rivera and others 2011.

Figure 5: (previous page) Examples of magnetic overprints are shown in samples collected from the CPT V, IX, and XII ignimbrites. Zijderveld, normalized magnetization, and partial vector (i.e., vector difference) equal area equatorial net plots are shown for each sample. An AF demagnetization of a CPT XII sample has a low and high coercivity overprint that are both close the dipole field direction. AF

demagnetization of a CPT V sample and thermal demagnetization of a CPT IX contain a low coercivity/unblocking temperature overprint close to the dipole field direction, and an intermediate overprint close to the direction of the overlying flow. In all three examples, the primary remanence is successfully obtained through progressive demagnetization. Solid symbols and solid lines are lower hemisphere, and dashed lines and hollow symbols are upper hemisphere. The red squares indicate the mean remanence direction of the ignimbrite which the sample was collected. The blue square shows the mean direction of the overlying ignimbrite. Error circles are too small to be shown for the ignimbrite mean directions. The yellow star indicates the dipole field direction for southern Idaho. The 'B' indicates the first measurement of the progressive demagnetization.

Figure 6: Equal area plots show sample and flow mean directions for select Cougar Point Tuff (CPT) units exposed in the Black Rock escarpment. Correlative ignimbrite flow mean directions from Brown's Bench escarpment and the Cassia Mountains are plotted along with CPT VII and CPT XI sample directions that have anhysteretic remanence anisotropy (AARM) corrections. There is both tighter grouping of CPT VII sample mean directions, and better agreement in between CPT XI and its correlative units after AARM corrections. The imperfect correlation between CPT VII and Brown's Bench (BBU-3) may result from one or more factors, such as magnetic anisotropy, magnetic overprinting, secular variation, and tectonic tilting.

Figure 7: Magnetic remanence and partial anhysteretic anisotropy results are shown for a typical CPT VII paleomagnetic sample collected from the westernmost sampling locality at the Black Rock escarpment. The magnetic remanence was removed with very low alternating magnetic fields, and has clearly been effected by a magnetic anisotropy that is particularly large and prolate at low AF levels. (a) A zijdereld plot shows that the demagnetization trajectory is increasingly eastward and shallow with lower AF values (i.e. 0-6 mT). (b) An equal area plot shows the maximum (K1), intermediate (K2), and minimum (K3) principal anhysteretic remanence susceptibility directions measured in the 0-6 mT range and the vector difference remanence directions determined from 0-6 mT and 15-24 mT. The remanence and anisotropy directions are plotted on the upper and lower hemispheres, respectively. (c-f) Plots show the dependence of several variables on AF level, including the anisotropy degree (P=K1/K2), shape factor (T), and the declination and inclination of the partial remanence. The horizontal bars show the AF range in which the variable on the Y axis was measured. T is an anisotropy shape parameter that describes the susceptibility ellipse shape and varies from -1 (prolate) to 1 (oblate).

Figure 8: Zijderveld and equal area plots show uncorrected and corrected AF demagnetization results from a sample that has a particularly large effect from gyroremanence (GRM) acquisition. The method for GRM correction is described in Finn and Coe [In Review].

Figure 9: Equal area plots show flow mean remanence directions determined from samples that have and have not been corrected for gyroremanence acquired during AF demagnetization. In the case of BBU-1, using the corrected samples improves the proposed correlation. In both cases the error on the site mean is reduced. The method used for correction is described in Finn and Coe [In Review].

Figure 10: Paleomagnetic directions are shown for the Cougar Point Tuff (CPT) exposed at the Black Rock Escarpment. Individual CPT (e.g. CPT XI) are indicated by their roman numeral. Solid and hollow circles indicate lower and upper hemisphere, respectively. Colors match those used in figures 2 and 3. Most error circles are covered by the large marker points

Figure 11: Equal area plots showing the paleomagnetic correlations that are color coded to match figures 2 and 3. Grey symbols show the magnetic directions of ignimbrite which do not correlate. Hollow symbols and dashed error circles indicate upper hemisphere. Triangles are from the Cassia Mountains, and squares and circles are from the Browns Bench and Black Rock escarpments, respectively. Lines connect stratigraphically adjacent eruption units from the Black Rock escarpment.

Figure 12: Plot of the Earth showing the virtual geomagnetic poles (VGP) that are color coded to match figures 2, 3 and 11. Lines connect stratigraphically adjacent eruption units from the Black Rock escarpment. The solid, dashed, and dotted black

lines connect stratigraphically adjacent eruptive units in the Black Rock and Brown's Bench escarpments and Cassia Mountains, respectively. Several of the correlating VGPs have magnetic pole positions that are uncommon in Earth's history (i.e. Far from the north and south poles), and therefore, make for very strong paleomagnetic correlations.

Figure 13: a) Rb/Sr versus Th/Nb whole rock element ratios. b) FeO versus MgO (wt.%) in SRP pigeonite and augite showing overlapping augite and pigeonite composition of the proposed correlation. Modal pigeonite composition P1-4 and P6, and CPT XI pyroxene data are after Cathey and Nash (2004).

Figure 14: Estimates of the extent of deposition of eruptions that correlate between the Black Rock escarpment (BE), Brown's Bench (BB) and Cassia Mountains (CM). The estimated area for CPT V, VII, and IX are shown in 'a' and areas for CPT XI, XIII, and XVb are shown in 'b'. The Grasmere Escarpment (GE) ignimbrite is considered part of the CPT, although because of the uncertainty in how it correlates with the CPT units with roman numerals, it is not included in the areal extent.

Table 1: Flow mean paleomagnetic directions

	Cougar Point Tuff					Sampling Location		Paleomagnetic Pole		
Ignimbrite Name	n/N	Dec	Inc	k	a96	Lat.	Long. [East (+)]	Lat	Long	a95
CPT XVb-E	10/10	10.3	70.0	320.9	2.7	42° 0.504'	-115° 37.420'	76.245	270.7	4.309
CPT XIII-E	10/10	346.3	64.8	32.5	8.6	42° 0.484'	-115° 37.440'	79.145	184.9	12.42
CPT XII-E	10/10	146.0	58.6	133.0	4.2	42° 0.439'	-115° 37.488'			
g-CPT XII-E	10/10	147.6	52.3	369.7	2.5	42° 0.439'	-115° 37.488'	-9.4	271.5	2.8
CPT XI-E	16/16	147.5	-34.9	162.7	2.9	42° 0.292'	-115° 37.716'			
a-CPT XI-E	16/16	140.4	-46.5	223.6	2.5	42° 0.292'	-115° 37.716'	-54.9	323.3	2.6
CPT IX-W	8/8	215.8	19.0	225.0	3.7	42° 0.430'	-115° 38.205'			
CPT IX-E	10/10	220.9	25.5	243.7	3.1	42° 0.285'	-115° 37.787'			
CPT IX_B	18/18	218.6	22.6	369.6	1.8	-	-	-25.605	201.8	1.39
CPT VII_W	8/8	170.6	-50.9	266.4	3.4	42° 0.474'	-115° 38.115'			
a-CPT VII-W	8/8	177.2	-52.1	282.0	3.3	42° 0.474'	-115° 38.115'			
CPT VII_E	13/14	196.0	-48.0	122.0	3.8	42° 0.250'	-115° 38.000'			
a-CPT VII-E	13/14	191.3	-47.7	297.9	2.4	42° 0.250'	-115° 38.000'			
a-CPT VII-B	9/22	189.2	-50.0	344.2	2.8	-	-	-76.6	208.1	3.1
CPT V-W	8/8	241.0	81.2	415.2	2.7	42° 0.555'	-115° 38.124'	32.2	226.6	5.1
CPT III-W	7/7	206.1	-35.8	173.1	4.6	42° 0.555'	-115° 38.124'	-58.7	191.5	4.1

	Brown's Bench Escarpment					Sampling Location		Paleomagnetic Pole		
Ignimbrite Name	n/N	Dec	Inc	k	a96	Lat.	Long. (Positive = East)	Lat	Long	a95
Rabbit Springs	9/10	1.7	70.6	88.6	5.5	42° 7.693'	-115° 47.898'	77.2	248.6	8.9
Jackpot	8/8	359.9	68.5	190.4	4.0	42° 7.6386'	-115° 47.826'	80.3	243.8	6.2
China Hill	10/10	149.7	-50.9	65.8	6.1	42° 7.5996'	-115° 47.741'			
a-China Hill	10/10	146.1	-54.3	132.0	4.4	42° 7.5996'	-115° 47.741'	-62.7	331.2	4.2
Black Canyon	12/13	216.7	23.5	131.4	3.8	42° 7.476'	-115° 47.716'	-26.3	203.7	2.9
Brown's Bench	14/16	198.6	-42.6	204.6	2.8	42° 7.284'	-115° 47.644'			
a-Brown's Bench	14/16	198.4	-45.1	260.7	2.7	42° 7.284'	-115° 47.644'	-68.4	194.1	2.7
Corral Creek	10/10	167.9	-37.1	89.2	5.1	42° 7.207'	-115° 47.628'	-66.3	273.4	4.6
BBU-1	9/9	267.3	73.6	91.7	5.4	42° 15.202'	-114° 15.920'			
g-BBU-1	9/9	260.4	77.9	148.3	4.2	42° 15.202'	-114° 15.920'	34.6	216	7.7

	Cassia Hills					Sampling Location		Paleomagnetic Pole		
Ignimbrite Name	n/N	Dec	Inc	k	a96	Lat.	Long. (Positive = East)	Lat	Long	a95
Steer Basin	10/10	356.3	69.5	911.5	1.6	42° 15.202'	-114° 15.920'	78.8	234.3	2.5
Big Bluff	9/9	344.7	67.4	442.7	2.4	42° 15.197'	-114° 15.766'	76.8	197.9	3.6
Magpie	13/13	148.5	-43.8	117.7	3.8	42° 15.057'	-114° 15.843'			
a-Magpie	13/13	146.2	-44.9	133.3	3.6	42° 15.057'	-114° 15.843'	-58.2	316.8	3.6

Table 2: Summary of single sanidine grain laser-fusion argon dates for Cougar Point Tuff, Rogerson and Cassia Formations. All argon ages are relative to sanidine feldspar standard FCs at 28.172 Ma ± 0.028 Ma (Rivera et al., 2011), and reported with 2s uncertainties.

Member	Sample Location	Weighted mean age (Ma)	Inverse Isochron age (Ma)
Cougar Point Tuff XVb	Black Rock Escarpment	-	-
Rabbit Springs	Brown's Bench Escarpment	[5]10.66 ± 0.09	
Steer Basin	Cassia Mountains	[5]10.63 ± 0.08	
Cougar Point Tuff XIII	Bruneau Canyon	[2]10.92 ± 0.06	-
Jackpot	Brown's Bench Escarpment	[4]10.960 ± 0.009	[4]10.960 ± 0.013
Big Bluff	Cassia Mountains	[5]10.97 ± 0.07	-
Cougar Point Tuff XI	Jarbidge Canyon	[2]11.35 ± 0.07	-
China Hill Member	Brown's Bench Escarpment	[1]11.305 ± 0.016	[1]11.324 ± 0.020
Magpie Basin	Cassia Mountains	[3]11.337 ± 0.008	[3]11.336 ± 0.009
Cougar Point Tuff IX	Bruneau Canyon	[2]11.70 ± 0.07	-
Black Canyon	Corral Creek (upper vitrophyre)	[4]11.667 ± 0.017	[4]11.66 ± 0.02
Black Canyon	Corral Creek (basal vitrophyre)	[1]11.662 ± 0.009	[1]11.658 ± 0.016
Cougar Point Tuff VII	Deer Creek Grade	[1]11.852 ± 0.007	[1]11.851 ± 0.007
Browns Bench	Brown's Bench Escarpment	[1]11.852 ± 0.009	[1]11.837 ± 0.013
Cougar Point Tuff V	Murphey Hotsprings	[1]12.288 ± 0.014	[1]12.287 ± 0.018
Cougar Point Tuff III	Bruneau Canyon	[2]12.81 ± 0.08	-

[1]This study (Table S5), [2]Bonnichsen et al., 2008; [3]Knott et al., 2016a; [4]2016b; [5]Ellis et al., 2012

Table 3: Flow by Flow Correlations

Site Pairs	k	δ	α	Pr	Ps	Ps/Pr	cum Ps/Pr
CPT XVb-E	335.9	9.7	3.0	2.24E-02	0.83	37.1	3.71E+01
Rabbit Springs	234.6	9.4					
CPT XIII-E	165.4	7.2	6.5	1.14E-01	0.53	4.6	1.72E+02
Jackpot	244.9	7.3					
a-CPT XI-E	408.2	27.0	8.6	5.02E-02	0.23	4.6	7.90E+02
a-China Hill	194.7	19.1					
CPT IX_B	245.6	89.4	2.0	3.04E-4*	0.94	3085.5	2.44E+06
Black Canyon	195.0	90.3					
a-CPT VII-B	207.7	12.3	7.9	9.12E-02	0.35	3.8	9.28E+06
a-Brown's Bench	240.5	19.4					
CPT V-W	239.0	33.9	4.8	1.8E-3*	0.73	417.6	3.87E+09
g-BBU-1	141.4	32.9					
CPT XVb-E	335.9	9.7	4.9	6.05E-02	0.55	9.2	9.16E+00
Steer Basin	320.8	8.4					
CPT XIII-E	165.4	7.2	2.7	1.98E-02	0.89	45.1	4.13E+02
Big Bluff	271.9	9.0					
a-CPT XI-E	245.6	27.0	4.4	6.73E-03	0.67	100.1	4.14E+04
a-Magpie	308.4	25.6					

*Uniform distribution (k=0) used because full-polarity Fisher distribution does not apply for transitional directions. Cum Ps/Pr would be ~30 times greater if Fisher distribution with k=22.6 were used.

Table 4: Paleomagnetic Data and Uncertainties

Site	k	s_W	s_F	s_T	s_A	s_O	s	k
Cougar Point Tuff								
CPT XVb-E	320.9	1.4	0.5	2.0	3.5	1.0	4.4	335.9
CPT XIII-E	32.5	4.5	0.5	2.5	3.0	2.0	6.3	165.4
a-CPT XI-E	223.6	1.4	0.5	3.0	2.0	1.0	4.0	408.2
CPT IX_B	369.6	1.0	0.5	3.5	3.5	1.0	5.2	245.6
a-CPT VII-B	344.2	1.5	0.5	4.0	3.5	1.0	5.6	207.7
CPT V-W	415.2	1.4	0.5	4.5	2.0	1.0	5.2	239.0
Brown's Bench Escarpment								
Rabbit Springs	88.6	2.9	0.5	2.5	3.5	1.0	5.3	234.6
Jackpot	190.4	2.1	0.5	3.0	3.5	1.0	5.2	244.9
a-China Hill	132.0	2.2	0.5	3.5	3.5	2.0	5.8	194.7
Black Canyon	131.4	2.0	0.5	4.0	3.5	1.0	5.8	195.0
a-Brown's Bench	260.7	1.3	0.5	4.5	2.0	1.0	5.2	240.5
g-BBU-1	148.3	2.2	0.5	5.0	3.5	2.0	6.8	141.4
Cassia Hills								
Steer Basin	911.5	0.8	0.5	2.5	3.5	1.0	4.5	320.8
Big Bluff	442.7	1.3	0.5	3.0	3.5	1.0	4.9	271.9
a-Magpie	133.3	1.9	0.5	3.5	2.0	1.0	4.6	308.4

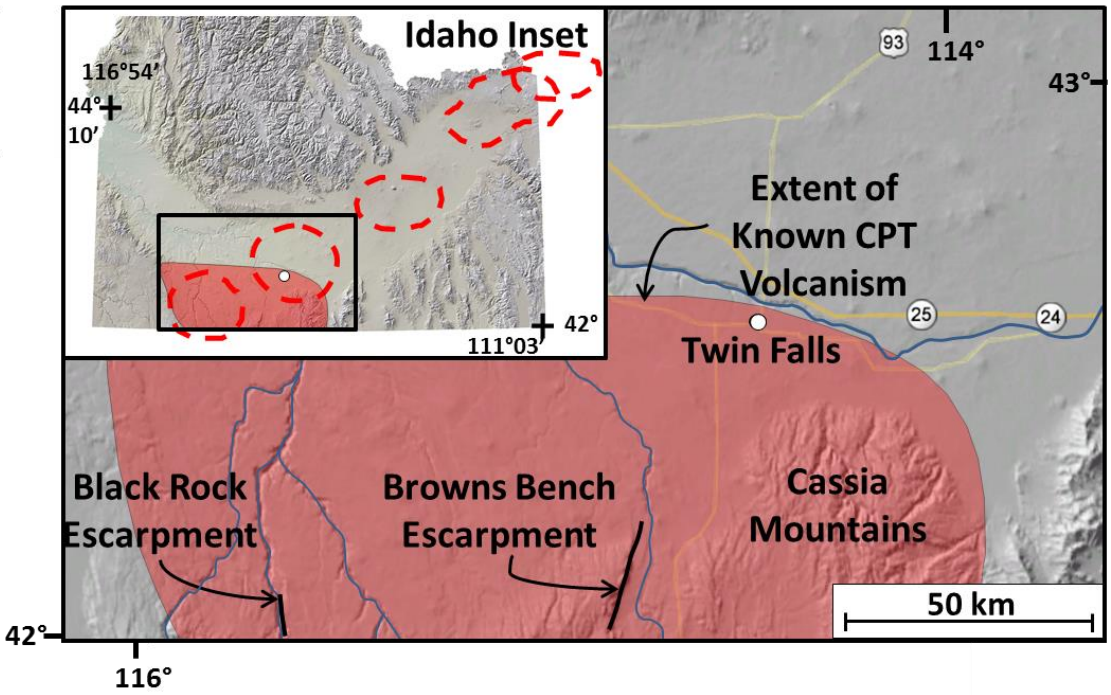

Figure 1: Map of the Snake River Plain showing the sampling locations. The inset map shows the southern 2/3 of Idaho with the approximate locations of eruptive centers (red dashed circles) and location of the enlarged area (black rectangle) indicated. The shaded red overlay shows the currently known extent of the Cougar Point Tuff (CPT) eruptions. The Grasmere Escarpment ignimbrite was included in this areal extent because it is thought to be part of the CPT, though the exact correlation to CPT units with designated roman numerals remains uncertain.

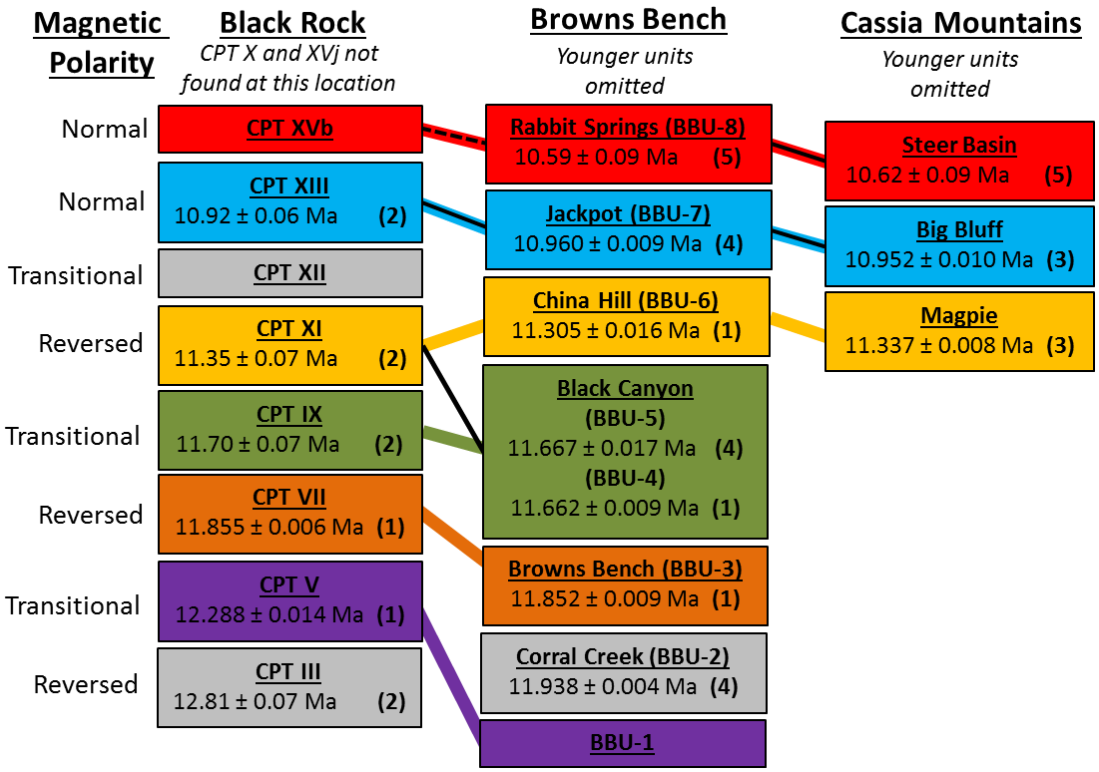

Figure 2: Correlations between the Black Rock and Brown's Bench escarpments, and the Cassia Mountains in southern Idaho. The colors are coded to match figure 2. Connecting lines that are thin and black were proposed by Ellis and others [2012]. The 1, 2, 3, 4, and 5 next to each age indicate the radiometric date was presented in this paper, Bonnichsen and others [2008], Knott and others [2016a], Knott and others [2016b], and Ellis and others [2012], respectively. The dates we present from published papers have been revised for a Fish Canyon Tuff standard age. We consider remanence directions that are pointed southward and down to be transitional.

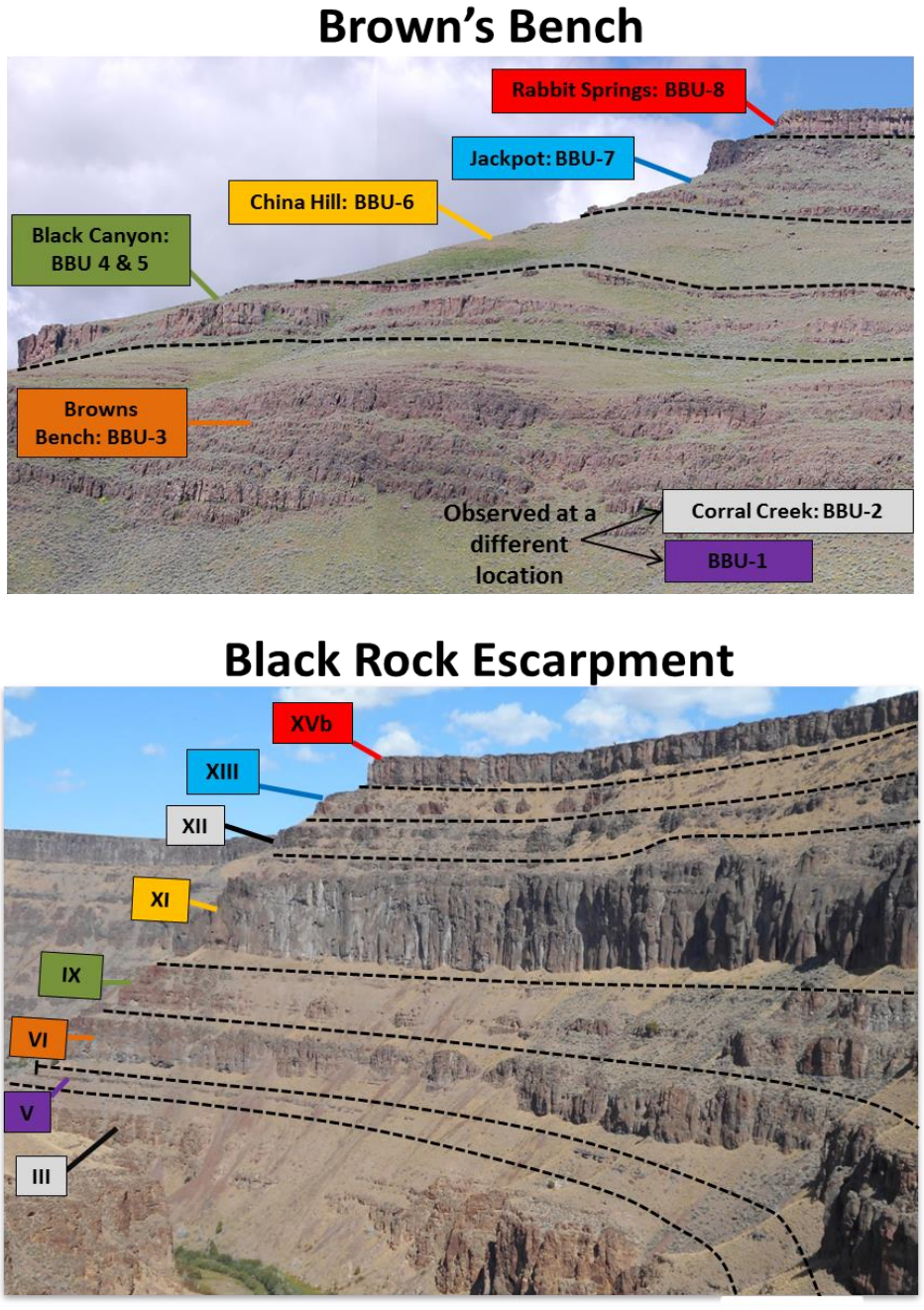

Figure 3: Photo of the Brown's Bench and Black Rock Escarpment sampling locations (see figure 1 map) with the units labeled and color coded based on the proposed correlations. There are two names given for each unit in the Brown's Bench escarpment because Knott and others [2016b] renamed each eruptive unit. The name on the left of the colon is from Knott and others [2016b] (e.g. China Hill) and the right is from Bonnichsen and others [2008] (e.g. BBU-6).

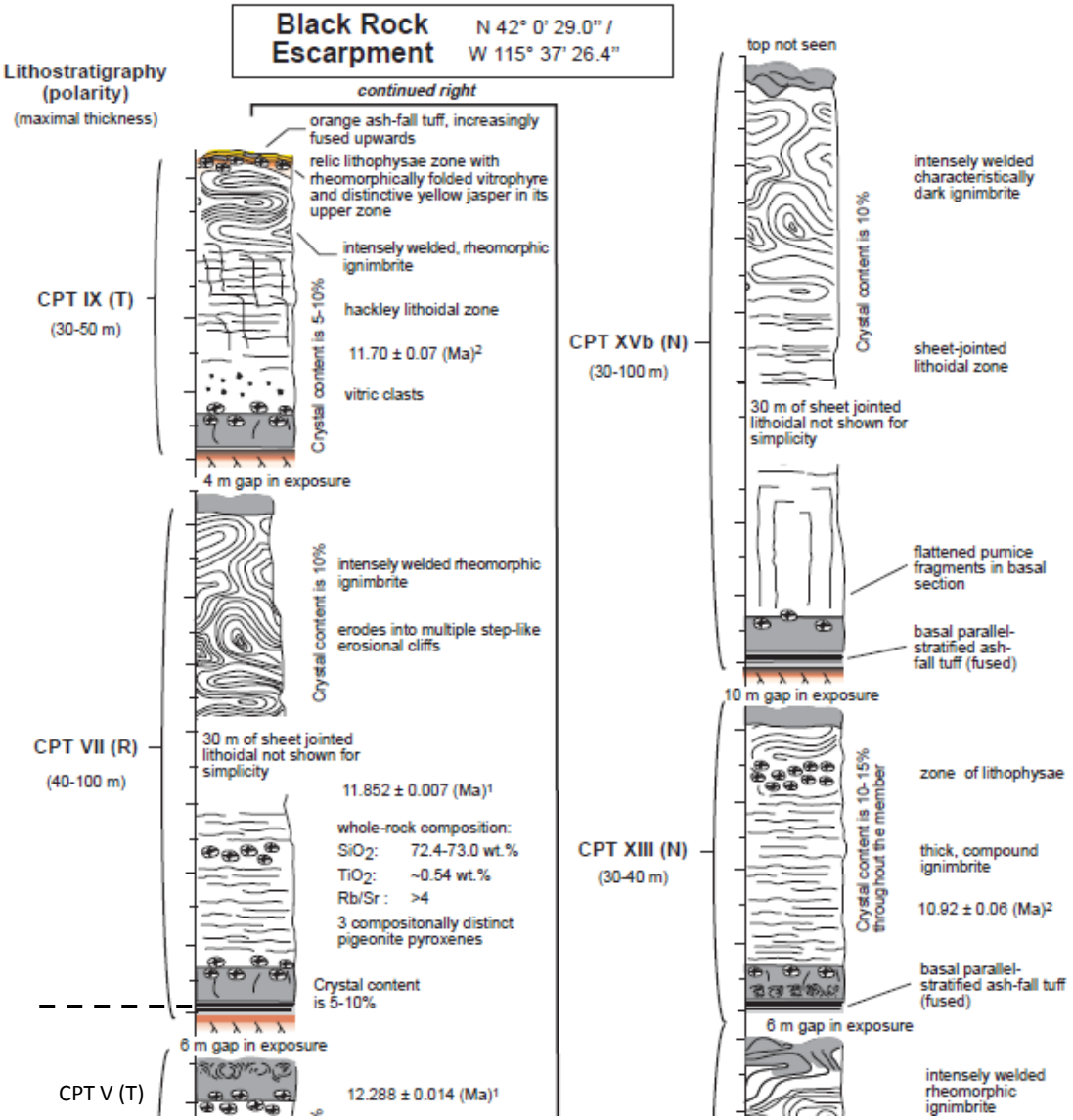

Continued on next page

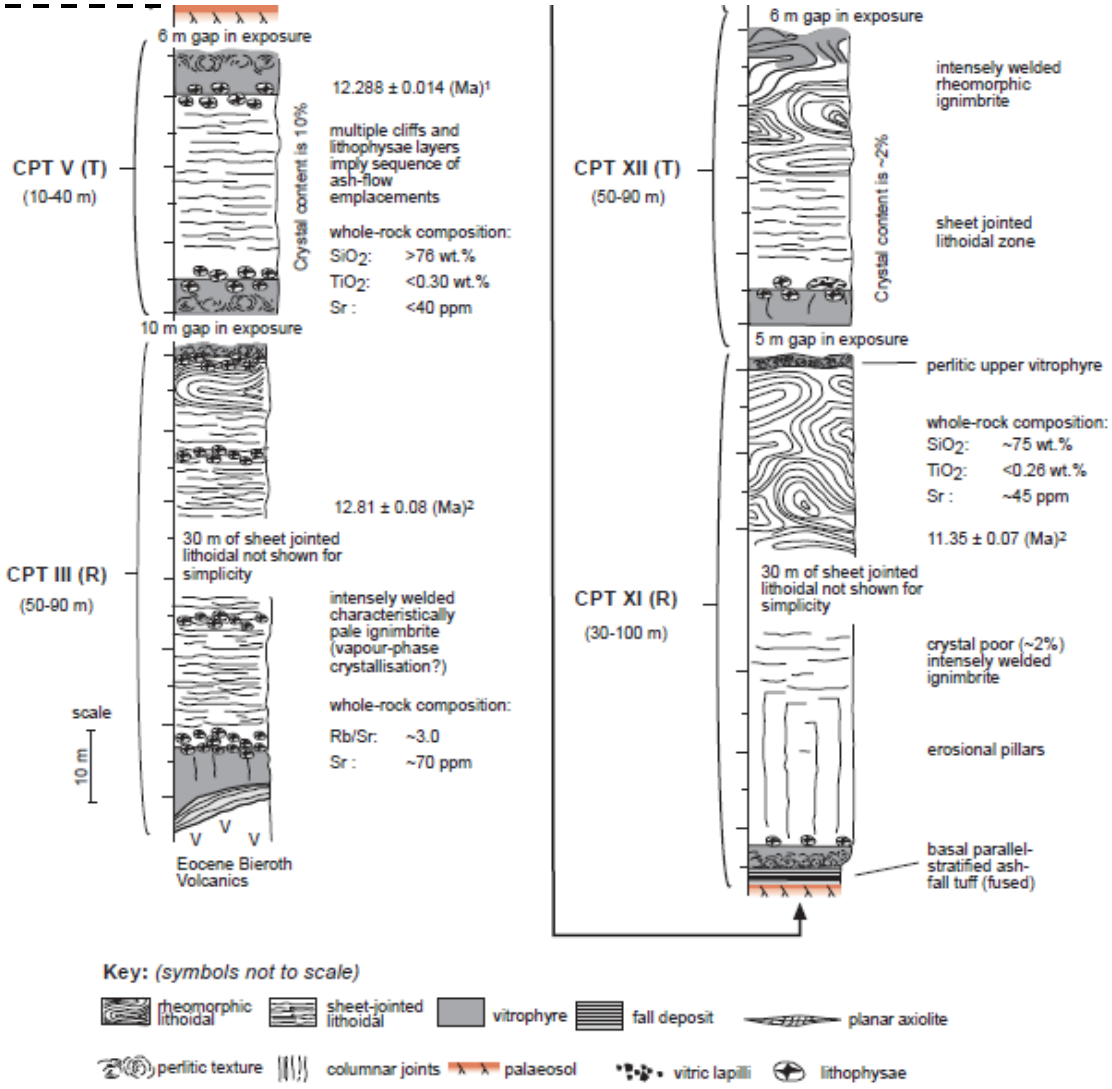

Figure 4: (Continued From previous page) Generalized vertical stratigraphy of the Cougar Point Tuff Formation showing the physical features of each of the eight members at the Black Rock Escarpment in southern Idaho. Argon ages: [1]this study; [2]Bonnichsen et al. (2008; recalculated to Rivera et al., 2011).

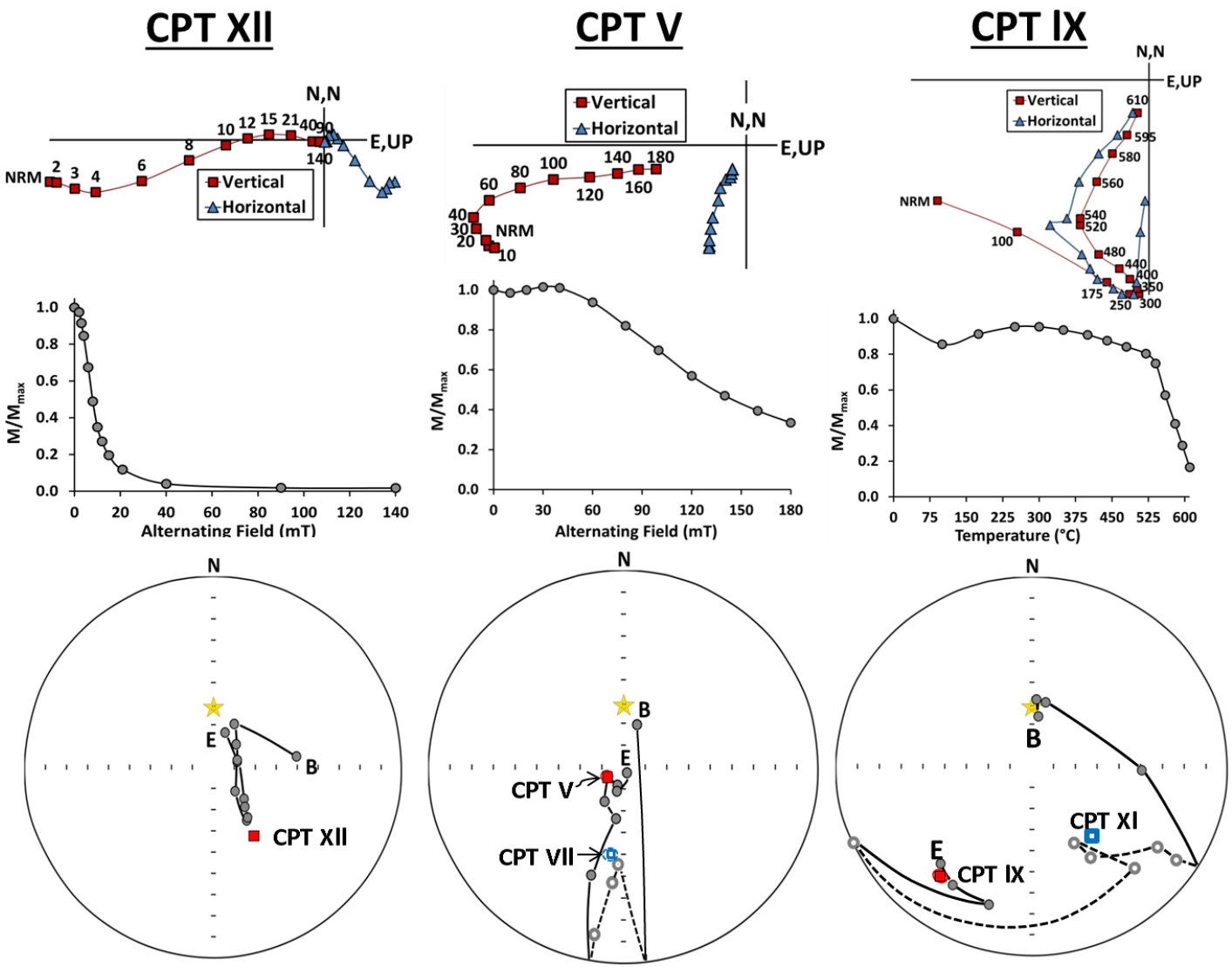
CPT XII
N,N
E,UP
NRM
2
3
4
6
8
10
12
15
21
40
90
140
Vertical
Horizontal
M/M_max
Alternating Field (mT)
CPT V
Vertical
Horizontal
N,N
E,UP
40
30
20
NRM
10
60
80
100
120
140
160
180
M/M_max
Alternating Field (mT)
CPT IX
N,N
E,UP
Vertical
Horizontal
NRM
100
175
250
300
350
400
440
480
520
540
560
580
595
610
M/M_max
Temperature (°C)
N
E
B
CPT XII
N
B
E
CPT V
CPT VII
N
B
CPT XI
E
CPT IX

Figure 5: (previous page) Examples of magnetic overprints are shown in samples collected from the CPT V, IX, and XII ignimbrites. Zijderveld, normalized magnetization, and partial vector (i.e., vector difference) equal area equatorial net plots are shown for each sample. An AF demagnetization of a CPT XII sample has a low and high coercivity overprint that are both close the dipole field direction. AF demagnetization of a CPT V sample and thermal demagnetization of a CPT IX contain a low coercivity/unblocking temperature overprint close to the dipole field direction, and an intermediate overprint close to the direction of the overlying flow. In all three examples, the primary remanence is successfully obtained through progressive demagnetization. Solid symbols and solid lines are lower hemisphere, and dashed lines and hollow symbols are upper hemisphere. The red squares indicate the mean remanence direction of the ignimbrite which the sample was collected. The blue square shows the mean direction of the overlying ignimbrite. Error circles are too small to be shown for the ignimbrite mean directions. The yellow star indicates the dipole field direction for southern Idaho. The 'B' indicates the first measurement of the progressive demagnetization.

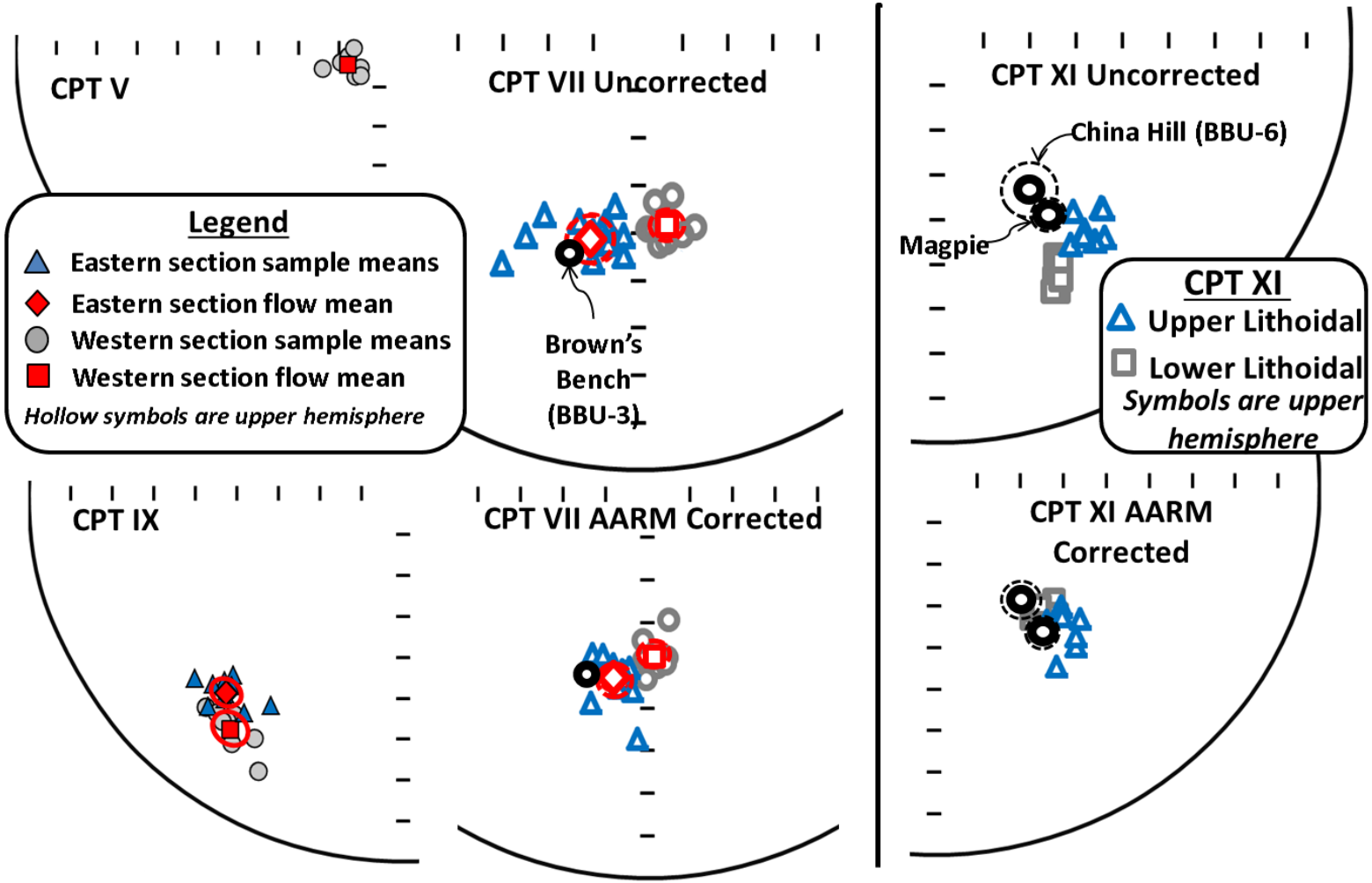
CPT V
CPT VII Uncorrected
Legend
Eastern section sample means
Eastern section flow mean
Western section sample means
Western section flow mean
Hollow symbols are upper hemisphere
Brown's Bench (BBU-3)
CPT XI Uncorrected
China Hill (BBU-6)
Magpie
CPT XI
Upper Lithoidal
Lower Lithoidal
Symbols are upper hemisphere
CPT IX
CPT VII AARM Corrected
CPT XI AARM Corrected

Figure 6: (Previous Page) Equal area plots show sample and flow mean directions for select Cougar Point Tuff (CPT) units exposed in the Black Rock escarpment. Correlative ignimbrite flow mean directions from Brown's Bench escarpment and the Cassia Mountains are plotted along with CPT VII and CPT XI sample directions that have anhysteretic remanence anisotropy (AARM) corrections. There is both tighter grouping of CPT VII sample mean directions, and better agreement in between CPT XI and its correlative units after AARM corrections. The imperfect correlation between CPT VII and Brown's Bench (BBU-3) may result from one or more factors, such as magnetic anisotropy, magnetic overprinting, secular variation, and tectonic tilting.

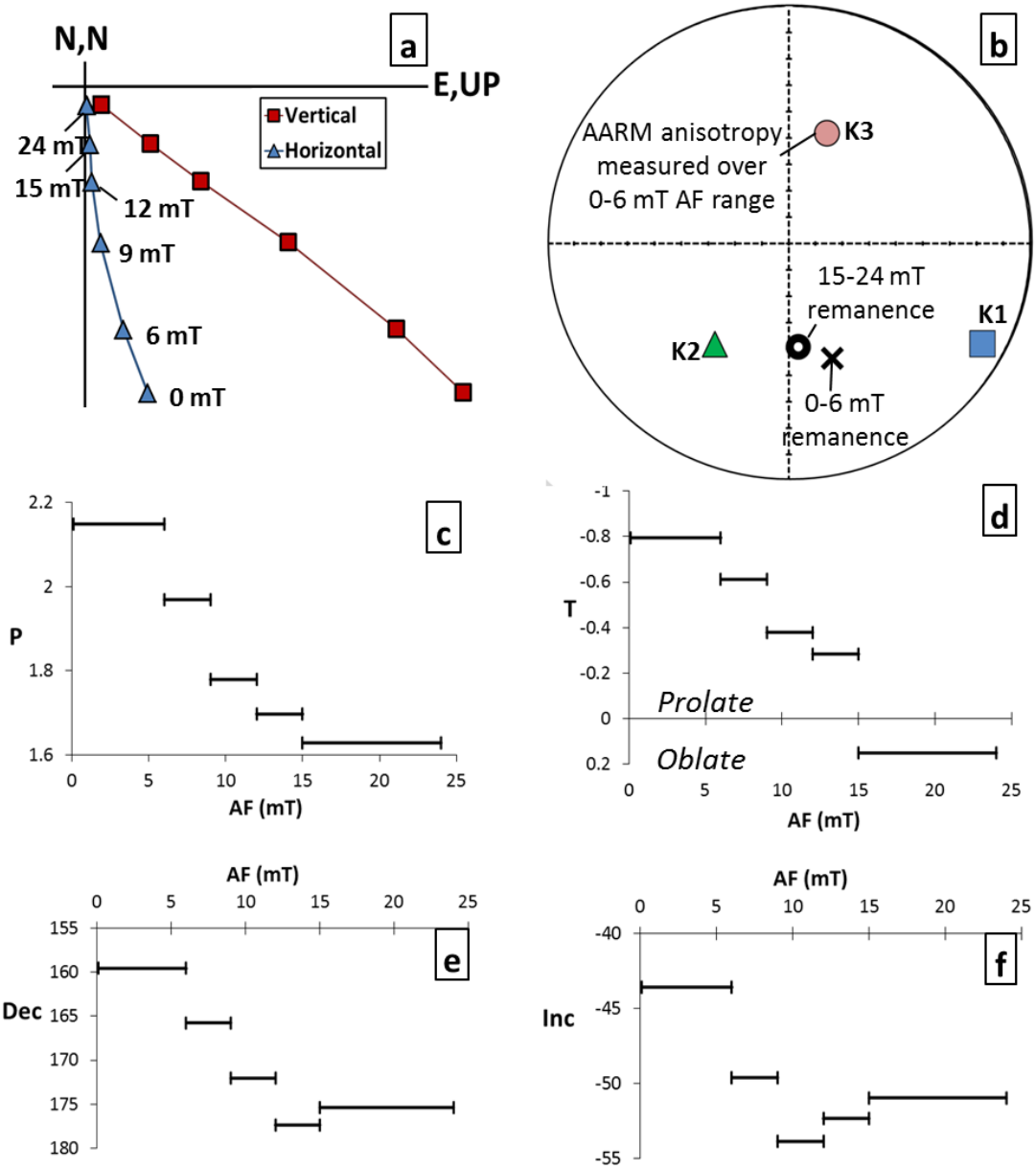
a
N,N
E,UP
Vertical
Horizontal
24 mT
15 mT
12 mT
9 mT
6 mT
0 mT
b
AARM anisotropy
measured over
0-6 mT AF range
K3
15-24 mT
remanence
K1
K2
0-6 mT
remanence
c
P
AF (mT)
d
T
Prolate
Oblate
AF (mT)
e
Dec
AF (mT)
f
Inc
AF (mT)

Figure 7: (Previous Page) Magnetic remanence and partial anhysteretic anisotropy results are shown for a typical CPT VII paleomagnetic sample collected from the westernmost sampling locality at the Black Rock escarpment. The magnetic remanence was removed with very low alternating magnetic fields, and has clearly been effected by a magnetic anisotropy that is particularly large and prolate at low AF levels. (a) A zijdereld plot shows that the demagnetization trajectory is increasingly eastward and shallow with lower AF values (i.e. 0-6 mT). (b) An equal area plot shows the maximum (K1), intermediate (K2), and minimum (K3) principal anhysteretic remanence susceptibility directions measured in the 0-6 mT range and the vector difference remanence directions determined from 0-6 mT and 15-24 mT. The remanence and anisotropy directions are plotted on the upper and lower hemispheres, respectively. (c-f) Plots show the dependence of several variables on AF level, including the anisotropy degree (P=K1/K2), shape factor (T), and the declination and inclination of the partial remanence. The horizontal bars show the AF range in which the variable on the Y axis was measured. T is an anisotropy shape parameter that describes the susceptibility ellipse shape and varies from -1 (prolate) to 1 (oblate).

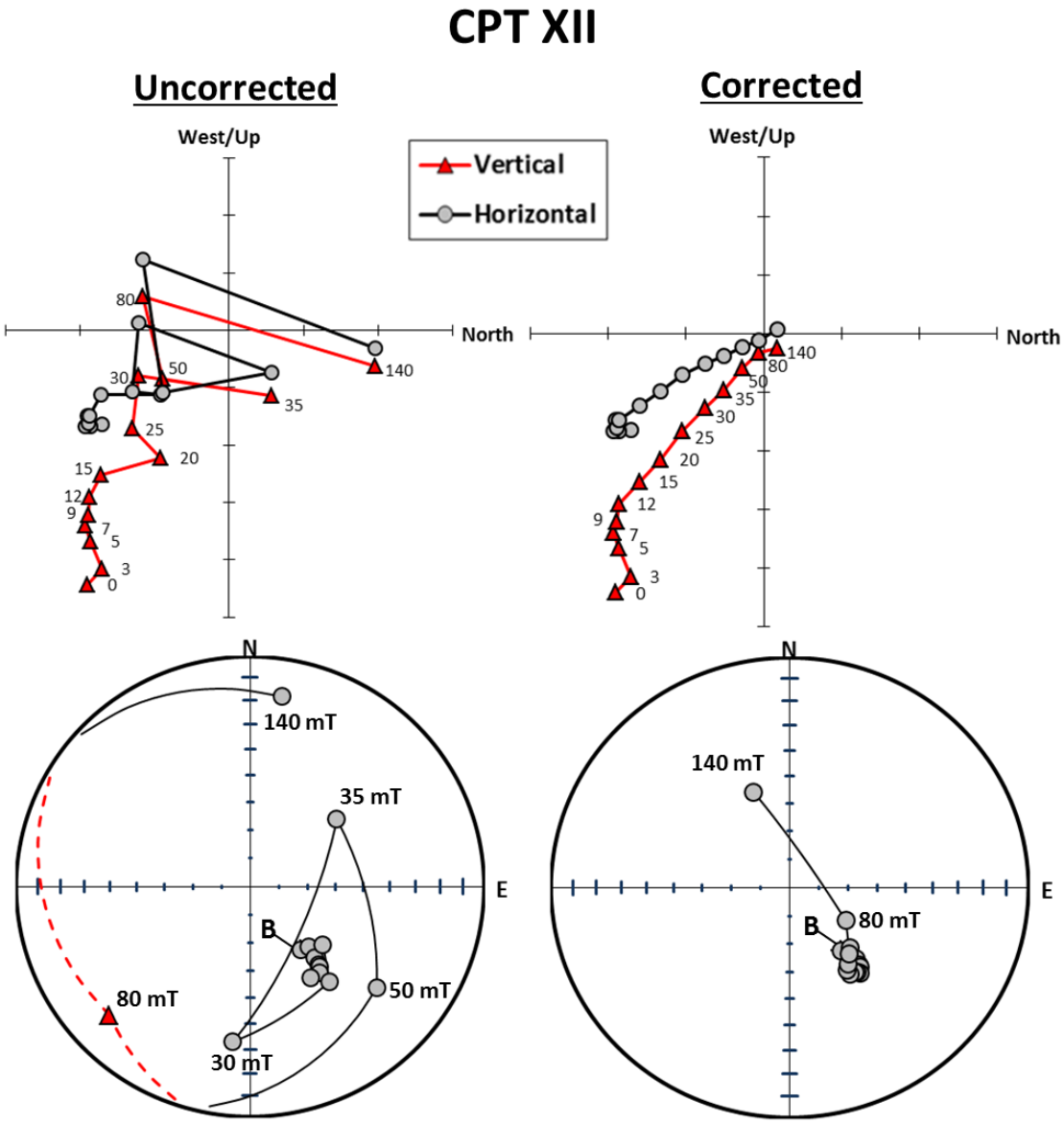

Figure 8: Zijderveld and equal area plots show uncorrected and corrected AF demagnetization results from a sample that has a particularly large effect from gyroremanence (GRM) acquisition. The method for GRM correction is described in Finn and Coe [In Review].

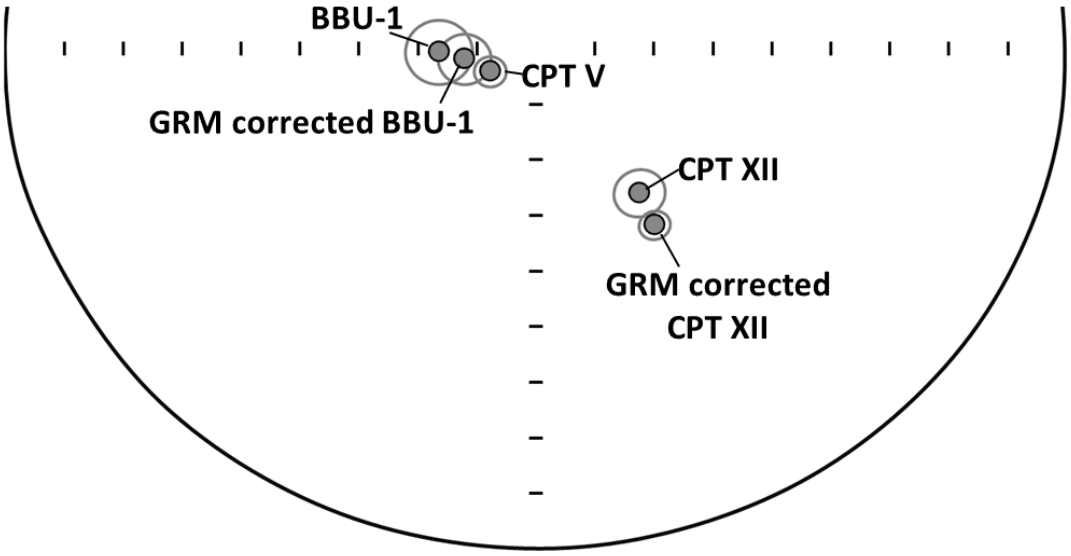

Figure 9: Equal area plots show flow mean remanence directions determined from samples that have and have not been corrected for gyroremanence acquired during AF demagnetization. In the case of BBU-1, using the corrected samples improves the proposed correlation. In both cases the error on the site mean is reduced. The method used for correction is described in Finn and Coe [In Review].

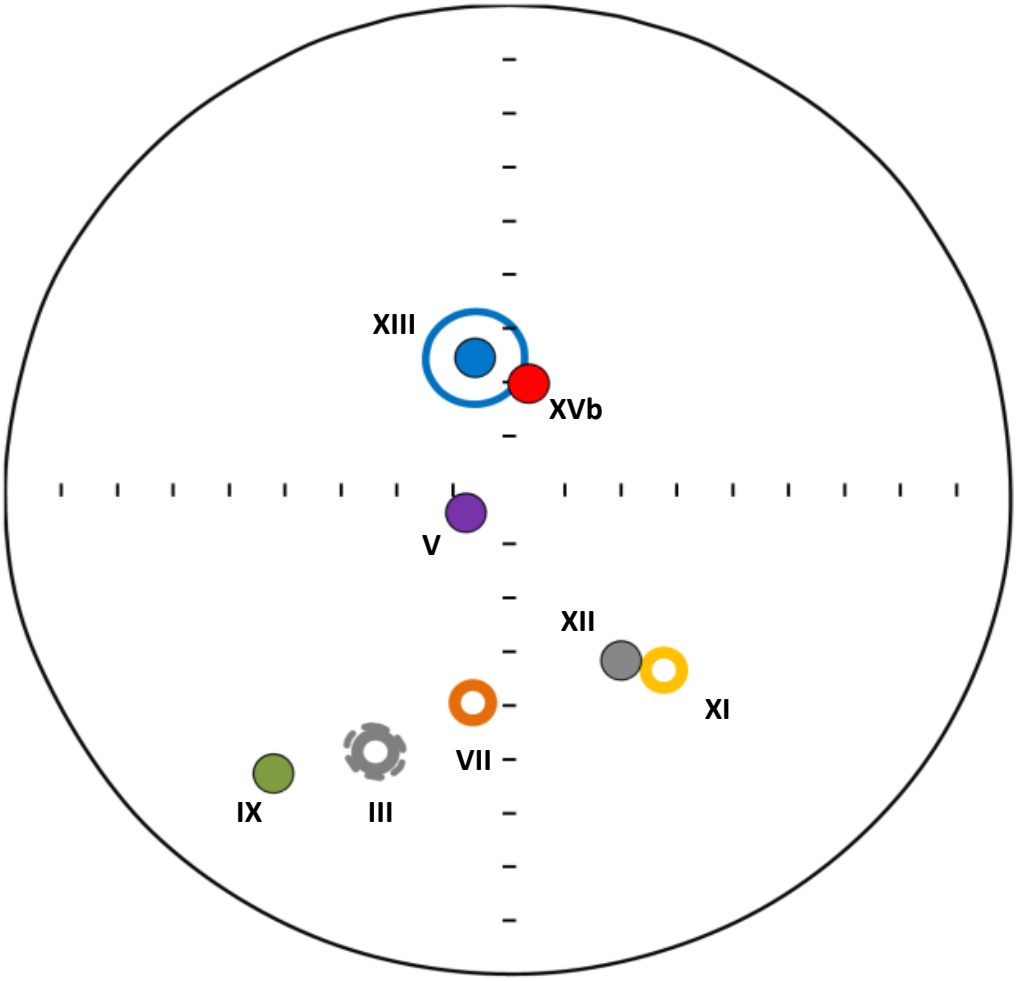

Figure 10: Paleomagnetic directions are shown for the Cougar Point Tuff (CPT) exposed at the Black Rock Escarpment. Individual CPT (e.g. CPT XI) are indicated by their roman numeral. Solid and hollow circles indicate lower and upper hemisphere, respectively. Colors match those used in figures 2 and 3. Most error circles are covered by the large marker points

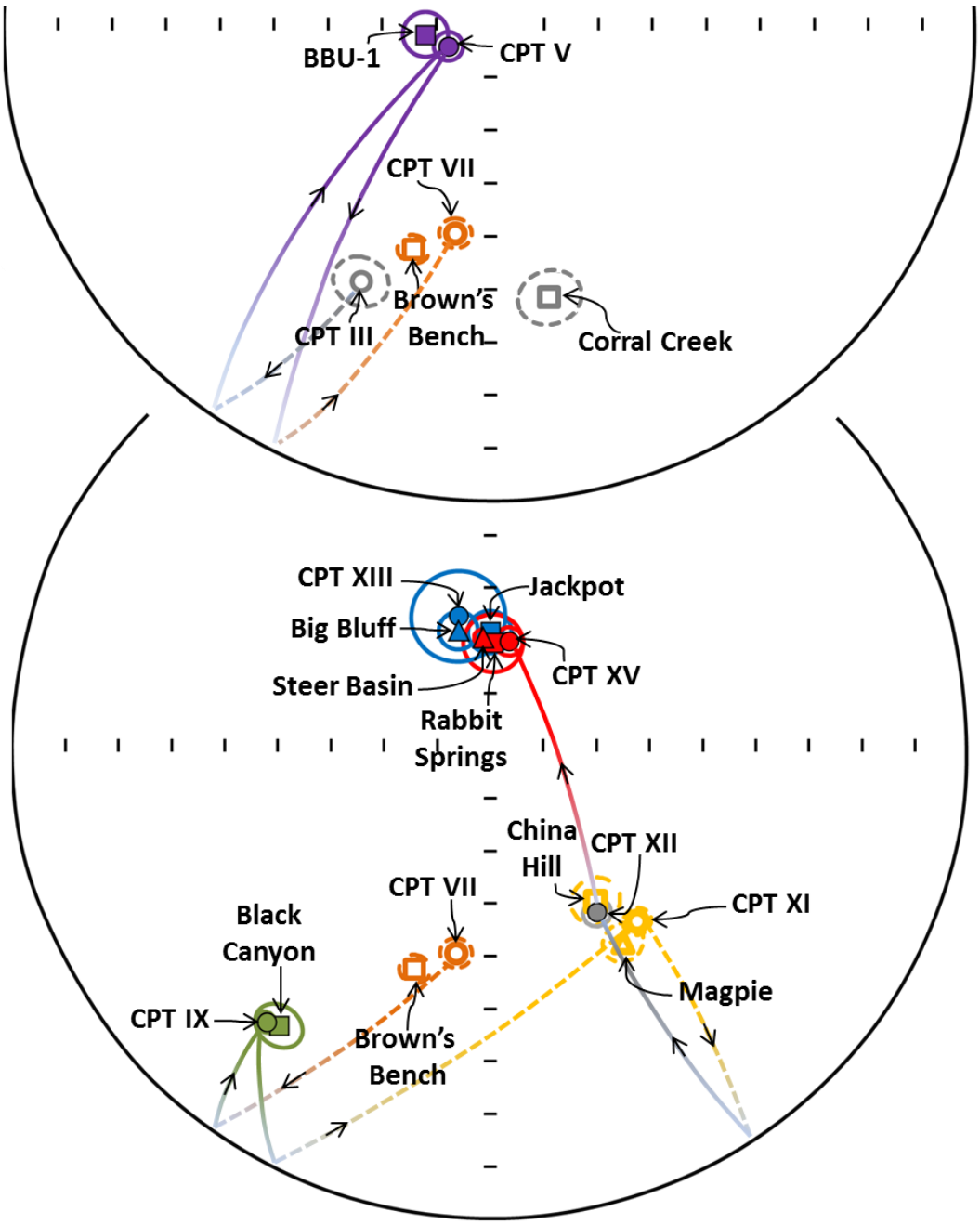

Figure 11: Equal area plots showing the paleomagnetic correlations that are color coded to match figures 2 and 3. Grey symbols show the magnetic directions of ignimbrite which do not correlate. Hollow symbols and dashed error circles indicate upper hemisphere. Triangles are from the Cassia Mountains, and squares and circles are from the Browns Bench and Black Rock escarpments, respectively. Lines connect stratigraphically adjacent eruption units from the Black Rock escarpment.

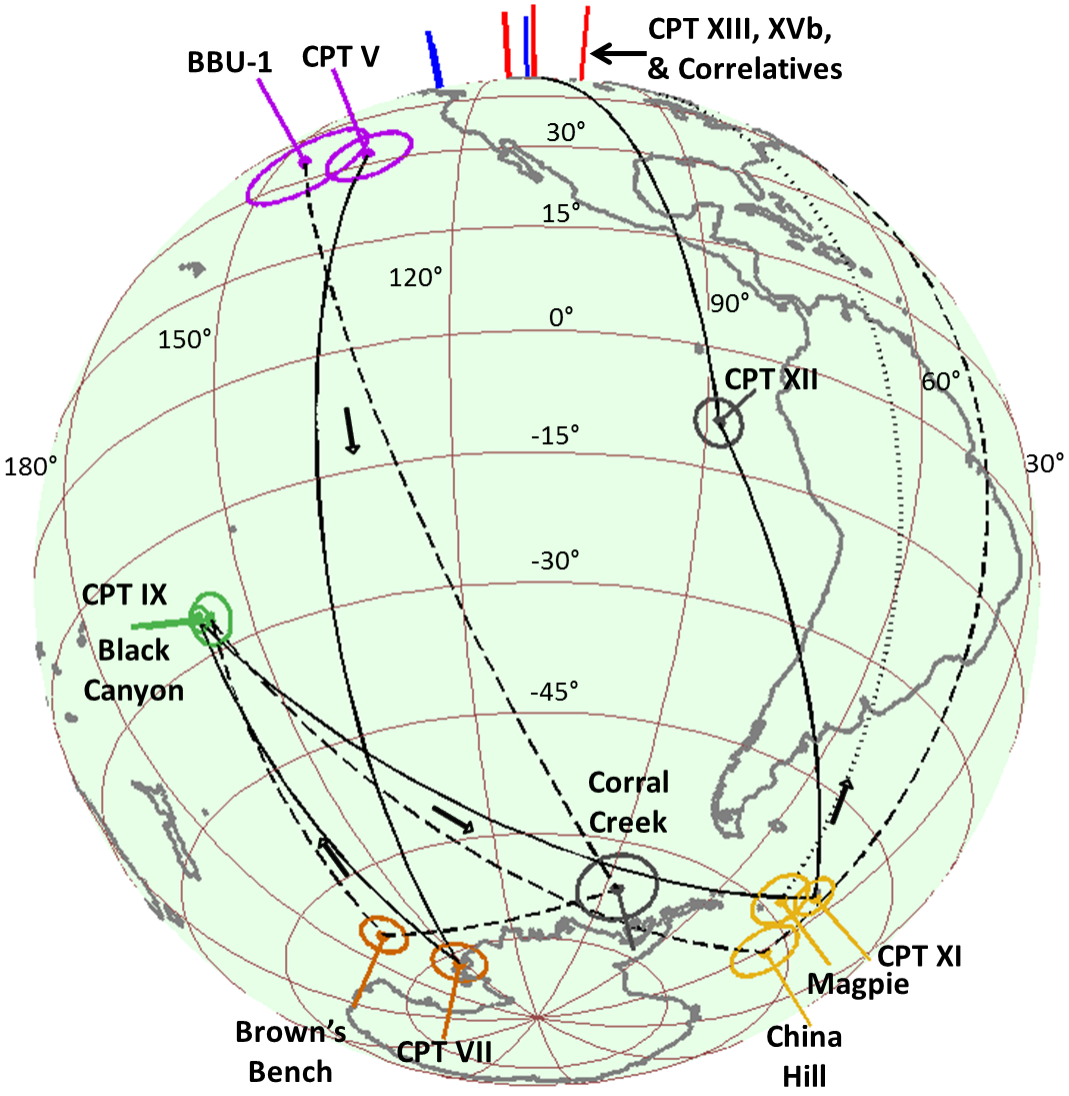

Figure 12: Plot of the Earth showing the virtual geomagnetic poles (VGP) that are color coded to match figures 2, 3 and 11. Lines connect stratigraphically adjacent eruption units from the Black Rock escarpment. The solid, dashed, and dotted black lines connect stratigraphically adjacent eruptive units in the Black Rock and Brown's Bench escarpments and Cassia Mountains, respectively. Several of the correlating VGPs have magnetic pole positions that are uncommon in Earth's history (i.e. Far from the north and south poles), and therefore, make for very strong paleomagnetic correlations.

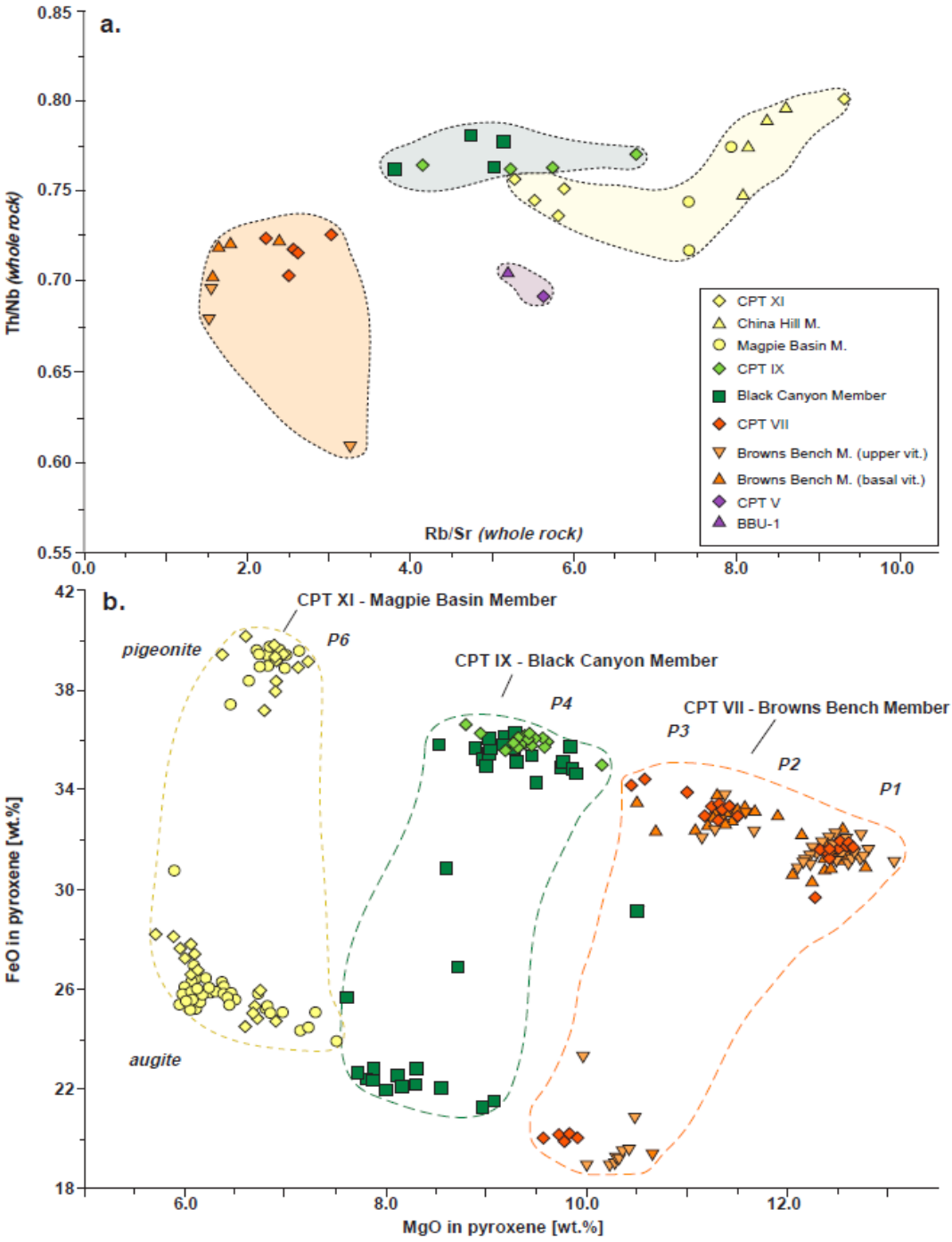

Figure 13: a) Rb/Sr versus Th/Nb whole rock element ratios. b) FeO versus MgO (wt.%) in SRP pigeonite and augite showing overlapping augite and pigeonite composition of the proposed correlation. Modal pigeonite composition P1-4 and P6, and CPT XI pyroxene data are after Cathey and Nash (2004).

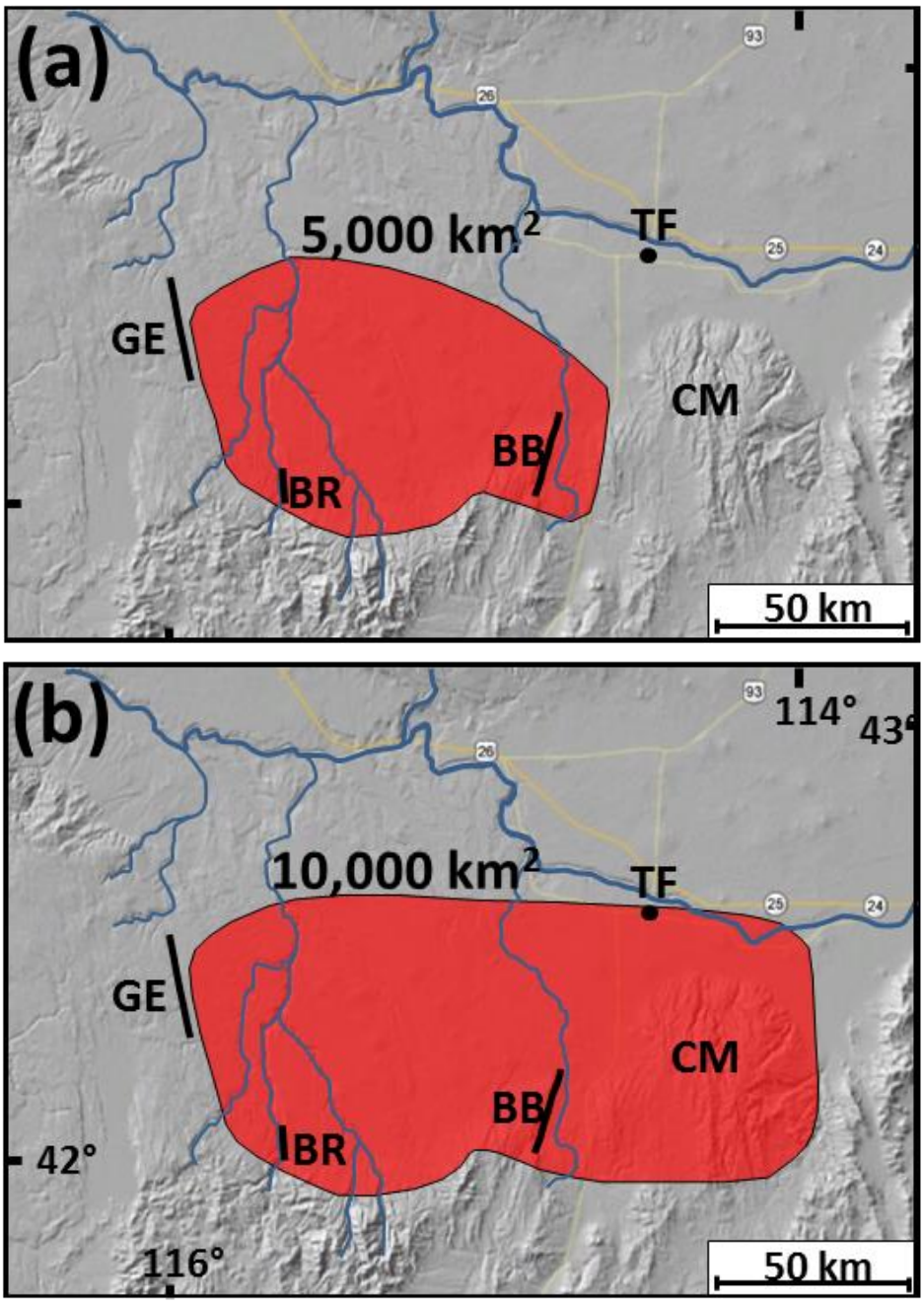

Figure 14: Estimates of the extent of deposition of eruptions that correlate between the Black Rock escarpment (BE), Brown's Bench (BB) and Cassia Mountains (CM). The estimated area for CPT V, VII, and IX are shown in 'a' and areas for CPT XI, XIII, and XVb are shown in 'b'. The Grasmere Escarpment (GE) ignimbrite is considered part of the CPT, although because of the uncertainty in how it correlates with the CPT units with roman numerals, it is not included in the areal extent.

Thesis Conclusion

The magnetic remanence recorded by strongly welded and rheomorphic ignimbrites can be used as an effective tool for distinguishing and correlating deposits from individual explosive rhyolitic eruptions. Characterization of geomagnetic secular variation through measurement of magnetic remanence has a temporal resolution (1-3 centuries) capable of determining if multiple ignimbrite deposits were simultaneously emplaced. More specifically, a ratio (Ps/Pr) of the probability that two magnetic directions are the same given their respective errors (Ps), to the probability of the magnetic direction being randomly repeated (Pr), may be used as an indicator of likelihood of two deposits or two sections being emplaced simultaneously [Bogue and Coe, 1981]. The example of a strong correlation between two magnetic directions presented in Bogue and Coe [1981] had a Ps/Pr ratio of 200, and their example of a strong correlation between sections had a cumulative Ps/Pr ratio of 1000. For comparison the CPT IX- Black Canyon correlation has a Ps/Pr ratio over 3000, which is a considerable underestimate (by a factor of 30) since a uniform distribution is used for Earth's Field (k=0). In addition, the cumulative Ps/Pr between the Brown's Bench and Black Rock escarpments is almost 4×10^9! This paleomagnetic technique was combined with field data, whole-rock and mineral chemistry, and radiometric dating to establish robust stratigraphic correlations. These correlations demonstrate that mid-Miocene eruptions were much larger and infrequent than previously thought, and that super-eruptions have been the common mode of volcanism at the leading edge of the Yellowstone Hotspot track for most of its existence.

In addition to correlations, one of the main topics of this thesis is addressing the complications that may produce error in determination of the paleofield direction in welded ignimbrite. There is a common misconception in the scientific community that volcanic rocks are excellent recorders of the paleofield direction. However, I have found there to be several issues that affect the magnetic remanence of strongly welded and rheomorphic ignimbrites that could lead to significant error in the measurement of a paleofield direction: 1. Large deflection of stable natural remanent direction (observed up to 38°) results from large anisotropy of thermoremanent magnetization. 2. Preferential overprinting of the upper part of ignimbrites may partially to completely destroy the original thermochemical remanence obtained during initial cooling. 3. Significant acquisition of gyroremanence during alternating field demagnetization may obscure measurement of the natural remanence.

I propose a new protocol to mitigate these potential pitfalls that could yield incorrect determinations of magnetic remanence directions in SR-type ignimbrites. Paleomagnetic samples should be collected from two sites in each cooling unit: one from the stable and more strongly magnetized basal vitrophyre, which is more resistant to chemical overprinting, and the other from the rheomorphically folded devitrified central part of the ignimbrite, as this is least effected by magnetic anisotropy and relatively far from the CRM prone ignimbrite top. The measurement of anhysteretic remanence anisotropy can be used to detect and at least partly correct

the effects of large thermal remanence anisotropy, and a new protocol for 3-axis AF demagnetization [Finn and Coe, In Review] can be used to avoid potentially destructive effects of gyroremanence (GRM). This protocol takes no extra time or effort, and therefore should be implemented as a standard alternating field demagnetization procedure.

Description of the Chapter 3 Supporting Information

Introduction

The data are available in the supporting information to better describe our anhysteretic anisotropy analysis (Document S1) and measurement results (Table S1 and Figure S3), report sample mean directions for each site (Table S2), report SI method (GRM removal) analysis and results (Tables S3-S4), and provide more information on the Black Rock escarpment and Hole in the Ground sampling localities (Figures S1-S2).

Document S1.

This document provides a detailed description of the laboratory procedure and calculations that produced the CPT VII and CPT XI anhysteretic remanence anisotropy results in Table S1.

Document S2.

This document provides a description of the Argon laboratory methods, analysis, and a description of the results from each new date.

Document S3.

This document provides a description of the X-ray fluorescence and electron microprobe laboratory procedures used to measure whole rock and pyroxene chemistries

Figure S1.

Annotated Google Earth image shows the Hole in the Ground - Black Rock Canyon sampling location on the south end of the Black Rock escarpment, as well as nearby normal faults.

Figure S2.

An annotated photograph shows the sampling sites on the north wall of the Hole in the Ground tributary canyon on the southern end of the Black Rock escarpment. The CPT units are labeled and a large fold in CPT XI is indicated with a dashed red line.

Figure S3.

Image of the Cassia Mountains sampling section with red stars indicating the drilling locations.

Figures S4-S8.

$^{40}Ar/^{39}Ar$ single sanidine age probability distribution and percent $^{40}Ar^*$ (radiogenic) of the China Hill, Black Canyon, Browns Bench, Cougar Point Tuff VII and Cougar Point Tuff V members. Open symbols indicate outliers, and solid and dashed lines probability distribution excluding and including outliers, respectively. Individual analyses are shown with one-sigma errors and the weighted mean age with two-sigma uncertainty is indicated by gray bar. $^{39}Ar/^{40}Ar$ inverse isochron diagram (inset).

Table S1.

Anhyesteretic remanence anisotropy and remanence correction results are shown for CPT XI (S1a), China Hill (S1b), Magpie (S1c), CPT VII at the Hole in the Ground sub-section (S1e), CPT VII at Black Rock escarpment sub-section (S1f), and the Brown's Bench Ignimbrite (Sig). From left to right the column headings represent:

Column 1 ("Sample ID"): Sample identification number

Column 2 ("Lithology"): Information about lithology (e.g. lithoidal, upper lithoidal, basal vitrophyre, etc.)

Column 3 ("AF Range (mT)"): AF range in milliTesla (mT) in which the .1 mT DC bias was applied for the three orthogonal ARM applications. For most samples we used the same AF range in which the best fit line to the demagnetization was determined (see column 3 from Table S2). For these samples we put "(same)" after

the AF range. Theoretically, this seems to be the most reasonable approach to measuring AARM with the intent of correcting remanence. However, we don't have any results that demonstrate this approach is best and instead found this not to work well for at least one site (Table S1f). Discussion of remanence anisotropy and methods for correction of remanence, particularly with regard to CPT VII, will be the topic of a future paper. For now this paper, we consider the AARM correction to improve results, but not fully restore them.

Columns 4-7 ("L, F, P, T"): These parameters describe the shape and degree of anisotropy. The maximum (K1), intermediate (K2), and minimum (K3) principal susceptibility magnitudes are found by computing the eigenvalues of the susceptibility tensor. The lineation (L), foliation (F) anisotropy (P), and Shape parameter (T) used in this paper are defined by, L = K1/K2, F = K2/K3, P = K1/K3, T = (log(F) - log(L)) / (log(L) + log(F)), respectively.

Columns 8-11 ("Dg, Ig, Dgk, Igk"): These columns report the declination and inclination of the remanence vector before (Dg, Ig) and after (Dgk, Igk) correction using the measured AARM tensor. All directions are in geographic coordinates.

Columns 12-17 (Dg1, Ig1. Dg2, Ig2, Dg3, Ig3"): The maximum (K1), intermediate (K2), and minimum (K3) principal susceptibility directions are found by computing

the eigenvectors of the susceptibility tensor. These columns report the direction of K1 (Dg1, Ig1), K2 (Dg2, Ig2), and K3 (Dg3, Ig3) in geographic coordinates.

Table S2.

Sample mean directions are shown for all flow means presented in Table 1. Tables S2a-S2j, S2k-S2q, S2r-S2t show results from Black Rock (CPT) and Brown's Bench escarpments, and Cassia Hills. The AARM corrected directions are not shown. CPT XII and BBU-1 required use of the SI method [Finn and Coe, 2015] to remove gyroremanence and therefor also presented in Table S3. Line and great circle fits were calculated with using the PMGSC software developed by Randy Enkin (Geological Survey of Canada). In general, line fits were not forced through the origin unless it was clearly beneficial to do so. For example, if there was only a small number of measurements in a demagnetization in which the primary magnetization was obtained and not forcing through the origin produced obvious large departure in remanence direction from that of the site mean (i.e. the average direction of all other samples from the same site). Columns headings represent:

Column 1 ("ID"): Sample identification number

Column 2 ("Code"): Type of fit to the demagnetization data

Dir PCA = Line fit not fit through the origin

DirOPCA = Line fit forced through origin

GC PCA = Great circle fit

GCnPCA = Great circle fit normalized, points given equal weight

Column 3 (“STEPRANGE”): The alternating field range in which the line and great circle fits were calculated. NRM means no AF has been applied, remaining numbers are in mT (e.g. H020 = 20 mT)

Column 4 (“n/N”) : Number of measurements used in the samples line or great circle fits relative to the total number we planned to use in the site mean analysis (note: this excludes vitrophyre samples with the comment “No AARM measured , sample excluded” (n/N).

Columns 5, 7, 8 (“Dg, Ig, MAD°”): Declination, inclination, and maximum angular deviation of the best fit line or plane, respectively.

Column 9 (“Lithology”): This column gives information about lithology (e.g. lithoidal, upper lithoidal, basal vitrophyre, etc.)

Column 10 (“Comment”): This column comments on whether the sample was used in the flow mean calculation and why. Unfortunately we destroyed some samples for geochemical analysis before realizing magnetic anisotropy was a problem (China Hill, Magpie, BBU-3). For consistency, we included all sample directions in the site mean analysis. We sampled both vitrophyre and lithoidal for many flows. Since

vitrophyre is thought to be more anisotropic, we generally exclude these samples from site mean calculations. Regardless, these samples often carry the same remanence direction as the lithoidal and are likely not very anisotropic. We do keep vitrophyre samples for the Black Canyon because it is weakly magnetized with a potentially large overprint. Vitrophyre samples have a stronger and more stable remanence that is resistant to overprinting. We also keep vitrophyre samples for the Magpie ignimbrite because we don't have many samples and the vitrophyre has generally low anisotropy and the remanence has been corrected.

Table S3.

Line and great circle fits for progressive 3-axis static demagnetization where the order of the AF axes was permuted and the subsequent data smoothed to remove effects from gyroremanence acquisition [SI Method from Finn and Coe, In Review]. Line and great circle fits were done using the Demagnetization Analysis In Excel (DAIE) Microsoft Excel workbook [Sagnotti, 2013]. The SI method was calculated using a Microsoft Excel file made available by [Finn and Coe, In Review]. From left to right the column headers indicate

Column 1 ("Sample ID"): Sample identification label

Column 2 ("Fit Type"): L* = Line fit not forced through origin; C = Great circle fit.

Column 3, 4, 5 (“Dec, Inc, MAD°”): Declination, inclination, and mean angular deviation of the sample fit, respectively.

Column 6, 7, 8 (“Min Step, Max Step, Number of Steps”): Minimum and maximum alternating magnetic field (milliTesla) values used in the fit, and the mean angular deviation in degrees, respectively.

Columns 9, 10 (“Fixed Steps(X), Iterations(X)): The number of low AF measurements in the beginning steps of the progressive demagnetization that are kept fixed, and number of smoothing iterations are shown from use of the SI method on the X axis.

Columns 11, 12 (“Fixed Steps(Y), Iterations(Y)): The number of low AF measurements in the beginning steps of the progressive demagnetization that are kept fixed, and number of smoothing iterations are shown from use of the SI method on the Y axis.

Columns 13, 14 (“Fixed Steps (Z), Iterations (Z)): The number of low AF measurements in the beginning steps of the progressive demagnetization that are kept

fixed, and number of smoothing iterations are shown from use of the SI method on the Z axis.

Table S4.

Unsmoothed and smoothed demagnetization data are shown for all samples collected from the BBU-1 and CPT XII ignimbrite. The smoothing analysis proposed by Finn and Coe (In Review) is used to remove the effects of gyroremanence magnetization from a 3-axis AF demagnetizations. From left to right the columns indicate

Column 1: The first row of this column has the sample ID. The other rows show labels for adjacent cells in Column 2.

Column 2 ("SI Parameters"): This column shows the parameters that record the calculations made using of the SI method. These values correspond to columns 9-14 from Table S3. Cells are left blank when no smoothing analysis was used.

Column 3 ("AF"): Alternating magnetic field values in milliTesla.

Column 4 ("Axes"): Key that indicates the order in which the AF was applied to the sample coordinates during the 3-axis static AF demagnetization. "8" = No AF's have been applied; "1" = AF axes order was z, y, then x; "2" = AF axes order was x, z, then y; "3" = AF axes order was y, x, then z;

Column 5-10: The smoothed and unsmoothed x, y, and z demagnetization results are shown in amps per meter squared (Am^2).

Column 11 ("Intensity"): The magnetization is shown in Amps per meter (A/m)

Columns 12-15: Declination and inclination of the remanence vector in core and geographic coordinates

Table S5: Argon isotope data.

Table S6: Whole rock major and trace element data for the China Hill, Black Canyon, and Magpie Basin members, and the Cougar Point Tuff III, V, VII, IX and XI units.

References

Brumm, A., Jensen, G.M., van den Bergh, G.D., Morwood, M.J., Kurniawan, I., Aziz, F., and Storey, M., 2010, Hominins on Flores, Indonesia, by one million years ago: Nature, v. 464, p. 748–752, doi:10.1038/nature08844.

Finn, D. and Coe, R. S. (In Review). A New Protocol for 3-Axis Static Alternating Field Demagnetization of Rocks

Govindaraju, K., 1994, 1994 compilation of working values and sample description for 383 geostandards: Geostandards Newsletter, v. 18, p. 1–158, doi:10.1111/j.1751-908X.1994.tb00502.x.

Honjo, N., McElwee, K.R., Duncan, R.A., Leeman, W.P., 1986, K-Ar ages of volcanic rocks from the Magic Reservoir eruptive centre, Snake River Plain, Idaho. Isochron/West, v. 46, p. 15–17.

Imai, N., Terashima, S., Itoh, S., and Ando, A., 1995, 1994 compilation of analytical data for minor and trace elements in seventeen GSJ geochemical reference samples, "Igneous rock series: Geostandards Newsletter, v. 19, p. 135–213, doi:10.1111/j.1751-908X.1995.tb00158.x.

Imai, N., Terashima, S., Itoh, S., and Ando, A., 1996, 1996 compilation of analytical data on nine GSJ geochemical reference samples, "Sedimentary rock series: Geostandards Newsletter, v. 20, p. 165–216, doi:10.1111/j.1751-908X.1996.tb00184.x.

Imai, N., Terashima, S., Itoh, S., and Ando, A., 1999, 1998 compilation of analytical data for five GSL geochemical reference samples, the "Instrumental analysis series":

Geostandards Newsletter, v. 23, p. 223–250, doi:10.1111/j.1751-908X.1999.tb00576.x.

Knott, T., Reichow, M.K., Branney, M.J., Finn, D.R., Coe, R.S., Storey, M., Bonnichsen, B., 2016, Rhyolitic explosive eruptions and related crustal subsidence on the Yellowstone hotspot-track: The Rogerson Formation (Mid-Miocene), central Snake River Plain, USA. Bulletin of Volcanology.

Knott, T.R., Branney, M.J., Reichow, M.K., Finn, D.R., Coe, R.S., Storey, M., Barfod, D., McCurry, M., 2016, Mid-Miocene record of large-scale Snake River–type explosive volcanism and associated subsidence on the Yellowstone hotspot track: The Cassia Formation of Idaho, USA. GSA Bulletin doi:10.1130/B31324.1

Lee, J.Y., Marti, K., Severinghaus, J.P., Kawamura, K., Yoo, H.S., Lee, J.B., and Kim, J.S., 2006, A redetermination of the isotopic abundances of atmospheric Ar: Geochimica et Cosmochimica Acta, v. 70, p. 4507–4512, doi:10.1016/j.gca.2006.06.1563.

Min, K., Mundil, R., Renne, P.R., and Ludwig, K.R., 2000, A test for systematic errors in 40Ar/39Ar geochronology through comparison with U/Pb analysis of a 1.1-Ga rhyolite: Geochimica et Cosmochimica Acta, v. 64, p. 73–98, doi:10.1016/S0016-7037(99)00204-5.

Pouchou, J.L., and Pichoir, F., 1985, “PAP” procedure for improved quantitative analysis: Microbeam Analysis, v. 20, p. 104–105.

Powell, R., Hergt, J., and Woodhead, J., 2002, Improving isochron calculations with robust statistics and the bootstrap: Chemical Geology, v. 185, p. 191–204, doi:10.1016/S0009-2541(01)00403-X.

Renne, P.R., Knight, K.B., Nomade, S., Leung, K.-N., and Lou, T.-P., 2005, Application of deuteron–deuteron (D–D) fusion neutrons to 40Ar/39Ar geochronology: Applied Radiation and Isotopes, v. 62, p. 25–32, doi:10.1016/j.apradiso.2004.06.004.

Rivera, T.A., Storey, M., Zeeden, C., Hilgen, F.J., and Kuiper, K., 2011, A refined astronomically calibrated 40Ar/39Ar age for Fish Canyon sanidine: Earth and Planetary Science Letters, v. 311, p. 420–426, doi:10.1016/j.epsl.2011.09.017.

Sagnotti, L. (2013). Demagnetization Analysis in Excel (DAIE). An open source workbook in Excel for viewing and analyzing demagnetization data from paleomagnetic discrete samples and u-channels. Annals of Geophysics, 56(1), D0114.

Stephenson, A., Sadikun, S., & Potter, D. K. (1986). A theoretical and experimental comparison of the anisotropies of magnetic susceptibility and remanence in rocks and minerals. Geophysical Journal International, 84(1), 185-200.

Document S1: Anisotropy of Anhysteretic Remanent Magnetizations (AARM)

The AARM was measured and used to correct the remanence directions for samples in CPT VII and XI and its correlatives. This process involves magnetizing samples by application of a large decaying alternating field (AF) and a small direct biasing field (DC = .1 mT). In most experiments, the AF range in which the DC is applied was the same as the AF step range used to calculate the best fit line through the remanence demagnetization data for each sample. By doing this we hoped to best measure the anisotropy of the same population of grains that carried the measured remanence direction. In some samples from (particularly CPT VII) we found using a higher AF range for the AARM experiment then that in which the line fit was calculated resulted in larger AARM corrections better improved the correlation.

The equation relating the applied magnetic field vector (H_{app}) to the acquired anhysteretic remanent magnetization vector (M_{obs}) of a sample is

$$M_{obs}=\chi * H_{app} \quad (1)$$

where χ is the 3x3 symmetric AARM tensor. The AARM ellipsoids were determined by applying an ARM and measuring the remanence of samples along three orthogonal axes using an approach similar to that of Stephenson et al. (1986). First, the ARM is

applied along the X direction, and then remanence M_{xx}, M_{xy}, and M_{xz} was measured in the X, Y, and Z directions, respectively. This was repeated in the second and third ARM applications where the field was applied in the Y and Z directions, respectively. The observed remanent magnetizations consist of the following array of nine values:

M_{xx} M_{xy} M_{xz} (field along x)

M_{yx} M_{yy} M_{yz} (field along y)

M_{zx} M_{zy} M_{zz} (field along z)

Ideally, the off-diagonal pairs of this array should be symmetric (e.g. M_{xy}=M_{yx}), so that dividing the six independent coefficients by the applied field magnitude H_{app} would give the components of the AARM tensor. The least-squares-best-fit tensor to the nine measurements for this simple case is obtained by just taking the average of each off-diagonal pair. The maximum (K1), intermediate (K2), and minimum (K3) principal susceptibility directions and magnitudes are found by computing the eigenvectors and eigenvalues of χ, respectively. The anisotropy (P), lineation (L) and foliation (F) parameters used in this paper are defined by P = K1/K3, L = K1/K2, and F = K2/K3.

Large magnetic anisotropy causes the observed magnetization of a sample to deflect away from the applied field direction and toward a direction or plane of higher susceptibility. To calculate the AARM corrected remanence (paleofield) direction, the

inverse of the laboratory measured AARM tensor χ is multiplied by the observed remnant direction (M_{rem})

$$H_{cor}=Inv(\chi)*M_{rem}$$

Table S1 shows results from anhysteretic remanence anisotropy and natural remanence corrections for CPT VII and XI, and their correlatives.

Document S2: Description of the $^{40}Ar/^{39}Ar$ Dating Method and Results

1. Methodology

$^{40}Ar/^{39}Ar$ geochronologic dating was performed at the Quaternary Dating Laboratory (QUADLAB) at the Natural History Museum of Denmark. Experiments were conducted on single sanidine crystals representing Browns Bench, Black Canyon and China Hill members, and Cougar Point Tuff units V and VII, with Fish Canyon sanidine (FCs) as the neutron fluorescence monitor, using the age of 28.172 ± 0.028 Ma [Rivera et al., 2011] and 40K decay constants of Min et al. [2000]. Handpicked crystals of unknowns and FCs were loaded into 21-pit aluminium irradiation disks, wrapped in aluminium foil and heat-sealed within a quartz glass tube. Irradiation was conducted at the cadmium-lined Oregon State University TRIGA reactor during two separate irradiations with irradiation times of 20 and 16 h, respectively. Single sanidine crystal $^{40}Ar/^{39}Ar$ laser fusion analyses were carried out on a Nu Instruments Noblesse noble gas mass spectrometer that is equipped with one faraday and three ETP multiplier (ion-counting) detectors housed at the Quaternary Dating Laboratory (QUADLAB), Natural History Museum of Denmark, following methods similar to those detailed by Brumm and others [2010]. Crystals were gently degassed prior to fusion using a defocused beam from a 50 W Synrad CO_2 laser, followed by total fusion at 4–12 W power with a focused beam. Analyses of unknowns, blanks and monitor minerals were carried out in identical fashion, by measuring ^{40}Ar and ^{39}Ar on the single (high-mass) faraday detector (F), ^{38}Ar and ^{37}Ar on the axial ion counter, and ^{36}Ar on the low-mass ion counter, with baselines measured every cycle.

Measurement of the ^{40}Ar, ^{38}Ar and ^{36}Ar ion beams was carried out simultaneously and followed by measurement of ^{39}Ar and then the ^{37}Ar beam. Beam switching was achieved by varying the field of the mass spectrometer magnet and with minor adjustment of the quad lenses. All signals measured on the ion counters are dead-time corrected. Observed $^{40}Ar/^{36}Ar$ and $^{40}Ar/^{38}Ar$ ratios were corrected for instrument mass fractionation and detector efficiencies using correction factors calculated for each detector-isotope combination, using a time series of measured blank-corrected air aliquots derived from a calibrated air pipette relative to published atmospheric ratios $(^{40}Ar/^{36}Ar)_A = 298.56$ and $(^{40}Ar/^{38}Ar)_A = 1583.7$ [Lee and others, 2006]. Corrections for interfering isotopes produced by nucleogenic reactions during the irradiation were based on Renne and others [2005] with the exception of the value used for $(^{36}Ar/^{37}Ar)_{Ca} = (2.646 \pm 0.008) \times 10^{-4}$. Data collection and reduction were carried out using the program MASS SPEC (A. Deino, Berkeley Geochronology Centre). J-values were calculated for the irradiation positions of the FCs for the irradiation disk and the $^{40}Ar^*/^{39}Ar_K$ ratio of the FC_S extrapolated to the axial position of the unknowns using a plane-fitting algorithm. This $^{40}Ar^*/^{39}Ar_K$ ratio was used to calculate the J-values for the unknowns. Relative Ar-isotope abundances for samples given in the supplementary data table are blank and decay corrected and given in volts (Table S5). Outlier detection of individual $^{40}Ar/^{39}Ar$ age data within each data population are determined when the normalized median absolute deviation (nMAD) is greater than 1.5 (Powell et al., 2002).

2. Results

China Hill Member (lithoidal sample RGB-11.1–001; Lab ID. 2711)

The China Hill Member sanidine (250–500 □m) measurements yield a normal distribution with a weighted mean age of 11.305 ± 0.016 Ma (MSWD 0.36) including twenty-four of thirty-six single crystal laser fusion experiments (Figure S4). Radiogenic 40Ar* in the analysed sanidine feldspars was generally higher than 75%. This result is statistically in good agreement with the inverse isochron age of 11.324 ± 0.020 Ma (MSWD = 0.8). The corresponding $^{40}Ar/^{36}Ar$ intercept of 290 ± 5 along with consistent Ca/K ratios (Table S5) indicate only one source of radiogenic argon and an atmospheric trapped argon composition. The weighted mean age, which is statistically indistinguishable from the inverse isochron age, is considered to represent the best estimate of the crystallization age for the China Hill Member.

Black Canyon Member (basal vitrophyre sample RG-10.1–013; Lab. ID. 2449)

The Black Canyon Member sanidine measurements define a slight asymmetric age distribution with a weighted mean age of 11.662 ± 0.009 Ma (MSWD 1.53; probability 0.04) including twenty-nine of thirty-nine crystal laser fusion experiments (Figure S5). All sanidine were, except for three analyses, highly radiogenic with 40Ar* >92%. The weighted mean age is statistically in good agreement with the inverse isochron age of 11.658 ± 0.016 Ma (MSWD = 1.0) and the corresponding

$^{40}Ar/^{36}Ar$ intercept of 303 ± 18 along with consistent Ca/K ratios (Table S5) indicate only one source of radiogenic argon and an atmospheric trapped argon composition. We therefore consider the weighted mean age to represent the best estimate of the crystallization age for the Black Canyon Member.

Our new weighted mean age for this member is indistinguishable from the sanidine argon age of 11.667 ± 0.017 Ma by Knott et al. [2016] obtained from the upper vitrophyre, which affirms that the previously separate 'BB-4' and 'BB-5' units [Bonnichsen et al., 2008] represent a single eruption-unit.

Browns Bench Member (basal vitrophyre sample RG-10.1–015; Lab. ID. 2441)

Twenty-four single crystal laser fusion experiments on sanidine feldspar (250–500 □m) of the Browns Bench Member sample RG-10.1–015 were conducted relative to Fish Canyon sanidine monitor minerals. Browns Bench Member sanidine were highly radiogenic with 40Ar* >92% (Figure S6). The single crystal experiments yielded reproducible ages providing a weighted mean age of 10.852 ± 0.009 Ma (MSWD = 1.69; n = 19 of 24) for this member, which is statistically consistent with the inverse isochron age (10.837 ± 0.013 Ma; MSWD = 1). Our age confirms and refines the published age of 11.857 ± 0.007 Ma for this member obtained on a small set of single grains by Knott et al. [2016; n = 9]. Regression of these data provides a $^{40}Ar/^{36}Ar$ intercept of 362 ± 14 which is higher than the published atmospheric ratio [Lee et al., 2006]. Cumulative probability distribution of our data suggests a slight age zonation, implying the presence of four age populations (10.852 Ma, 11.98 Ma, 12.01 Ma and

12.27 Ma) of which only three are statistically different from our weighted mean age. The observed age distribution is interpreted to result from the presence of antecryst sanidine possibly recycled from a previous magmatic episode like the 12.28 Ma old CPT-V member (see below). We therefore consider the weighted mean age with an acceptable MSWD, which excludes the four oldest sanidine ages, to represent the best estimate of the crystallization age.

Cougar Point Tuff VII Member (basal vitrophyre sample CPT-10.2–002; Lab ID. 2481)

Twenty-five single crystal laser fusion experiments on sanidine feldspar (250–500 □m) of the Cougar Point Tuff VII Member sample CPT-10.2–002 were conducted relative to the Fish Canyon sanidine monitor. The single crystal experiments yielded reproducible ages providing a weighted mean age of 10.852 ± 0.007 Ma (MSWD = 1.11; n = 16 of 25) for this member, which is statistically consistent with the inverse isochron age (10.851 ± 0.007 Ma; MSWD = 2). The radiogenic 40Ar* content ranges between 54 to 100% but is above 80% in sanidines included into the weighted mean age (Figure S7). However, cumulative probability distribution of our data suggests a subtle age zonation, implying the presence of older, probably inherited grains. We interpret these data similar to those obtained on the Browns Bench Member above, to represent antecryst sanidine possibly recycled from a previous magmatic episode. The weighted mean age with an acceptable MSWD, which excludes the two youngest and

six oldest sanidine ages, is considered to represent the best estimate of the crystallisation age.

Cougar Point Tuff V Member (basal vitrophyre sample CPT-11.2–001; Lab ID. 2443)

Laser fusion experiments on Cougar Point Tuff V member single sanidine (Figure S8) provided a statistically robust weighted mean age of 12.288 ± 0.014 Ma (MSWD = 1.41; n = 11 of 13). An older, probably xenocrystic grain is also identified in this sample. The radiogenic 40Ar* yield is typically >86% with one low 40Ar* return of 32% in one experiment. The inverse isochron age of 12.287 ± 0.018 Ma (MSWD = 2) and the corresponding $^{40}Ar/^{36}Ar$ intercept of 298.7 ± 1.4 along with consistent Ca/K ratios (Table S5) indicate only one source of radiogenic argon and an atmospheric trapped argon composition. We consider the weighted mean age to represent the best age of crystallisation.

Document S3: Geochemical laboratory methods

1. Whole rock X-ray fluorescence (XRF) methodology (University of Leicester, UK)

Whole rock samples were prepared for major and trace element analysis by grinding in a Retsch planetary mill using agate pots and grinding balls. Major and trace element data were obtained on fusion beads and pressed powder pellets, respectively by X-ray fluorescence (XRF) analysis using a PANalytical Axios Advanced X-ray fluorescence spectrometer at the University of Leicester, UK. The PANalytical Axios runs a 4Kw Rhodium anode end window ceramic technology X-ray tube. Methods and calibrations for major and trace element analyses are described in detail by Knott et al. (2016). The analyses of international reference material indicate that precision for the observed data range and over the period of analytical work was 1% and 5% or better for trace and major elements, respectively (Knott et al., 2016). Results of 41 representative samples from the Cougar Point Tuff and Rogerson formations are listed in Table S6.

2. Electron Microprobe methodology (Open University, Milton Keynes, UK)

Thin sections (30 microns) were cut from select samples of each member of the Cassia Formation, and these were subsequently polished and carbon-coated prior to electron microprobe analysis. Analyses of pyroxene phenocrysts were obtained at the Open University, Milton Keynes using a Cameca SX100 electron microprobe. An operating voltage of 20 kV and probe current of 20 nA (measured on a Faraday cage) with a 10 micron beam diameter were used for quantitative analysis. Data were reduced using the PAP correction routine of Pouchou and Pichoir (1985). Results of pyroxene major elements are listed in Table S6.

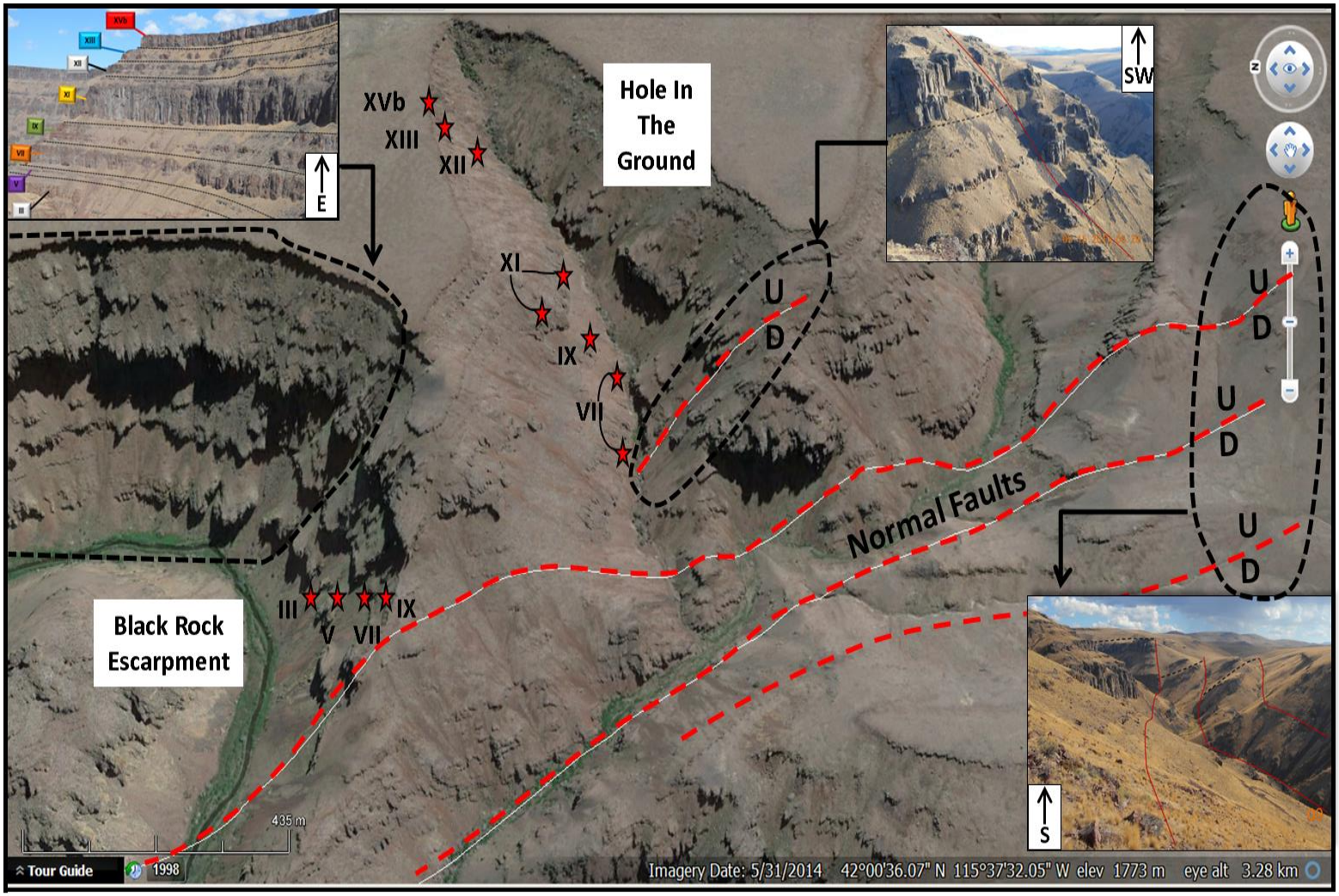

Figure S1: Google image showing two sampled sections on the southern end of the Black Rock escarpment and nearby faults

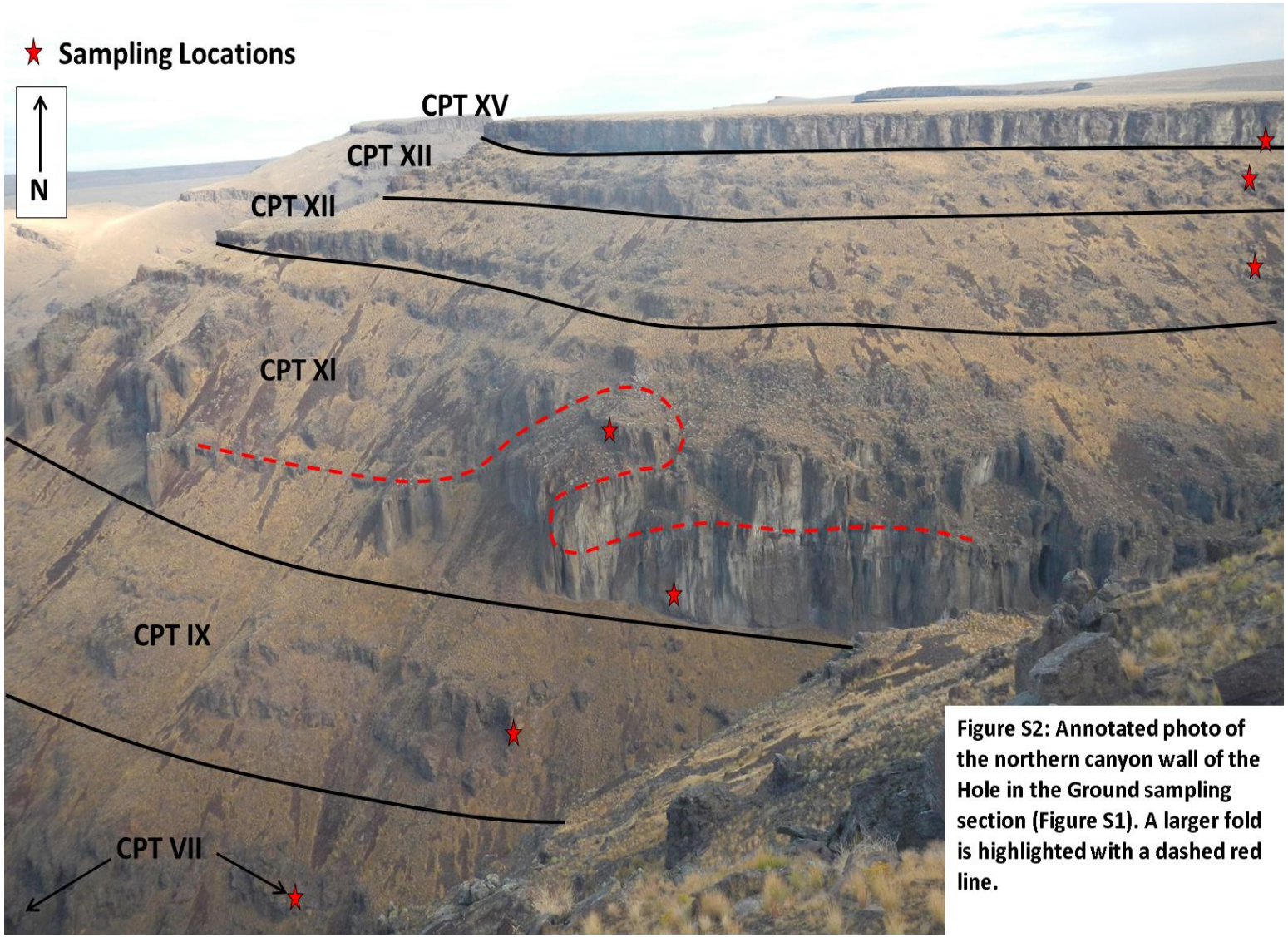

Figure S2: Annotated photo of the northern canyon wall of the Hole in the Ground sampling section (Figure S1). A larger fold is highlighted with a dashed red line.

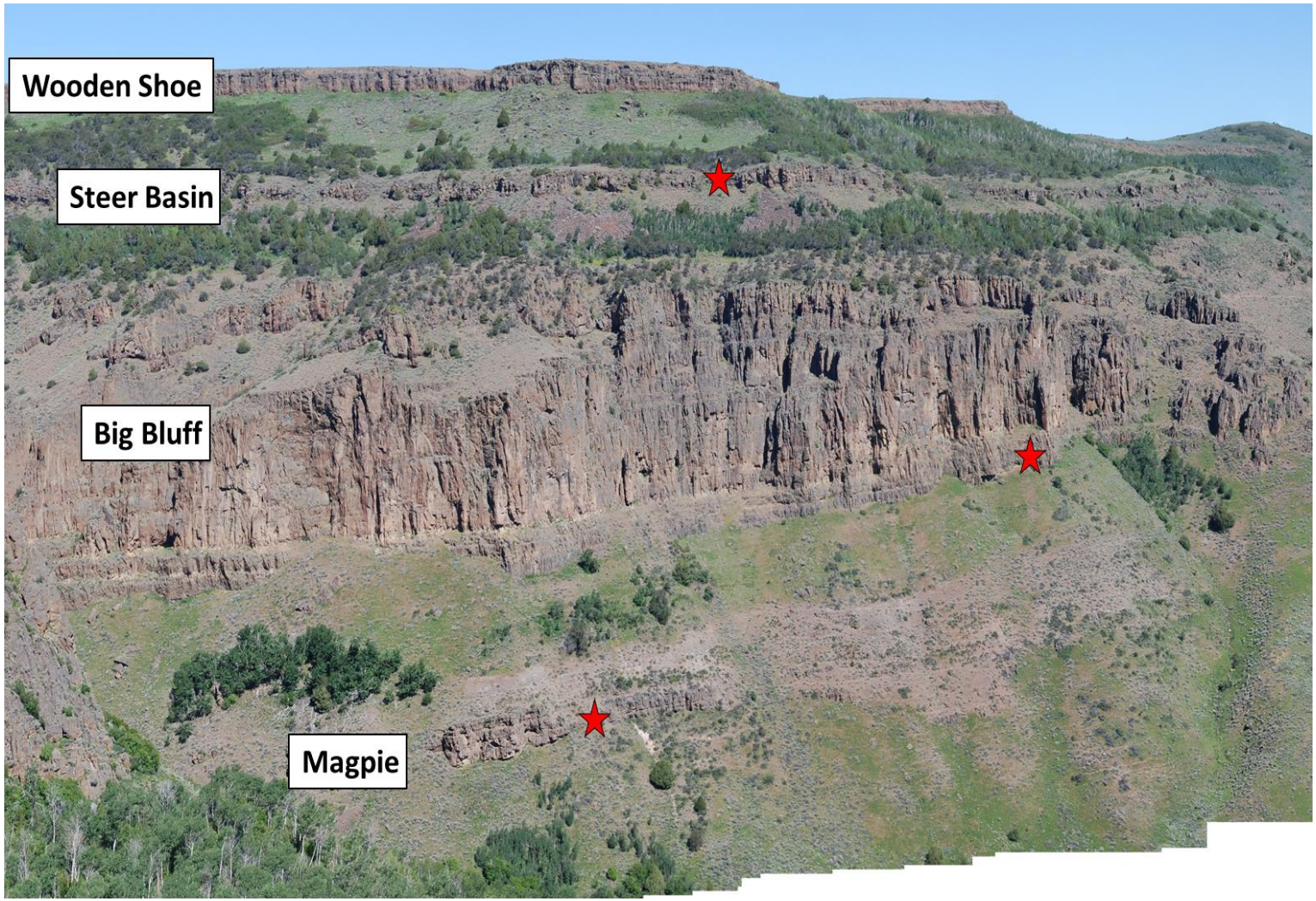

Figure S3: Image of the Cassia Mountains sampling section with red stars indicating the drilling locations

Figure S4;
China Hill Member sample RGB-11.1-001 (Lab. ID. 2711)

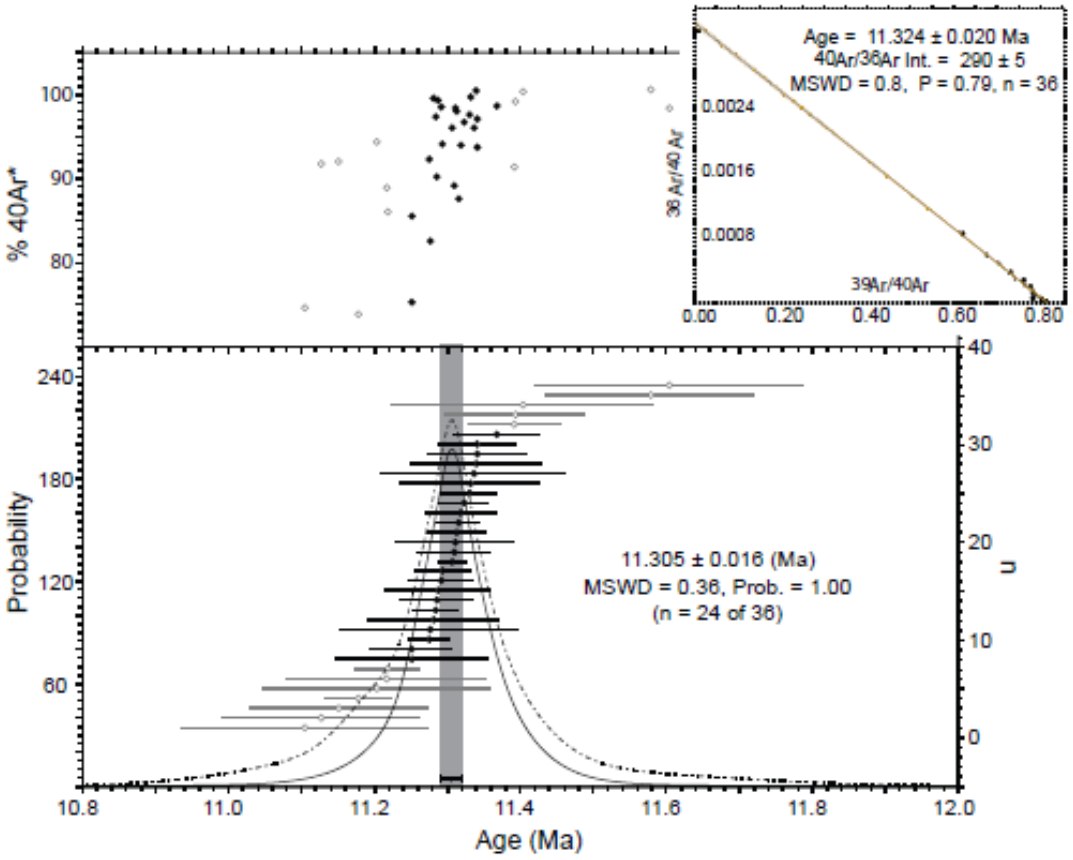

Figure S4 : $^{40}Ar/^{39}Ar$ single sanidine age probability distribution and percent $^{40}Ar^*$ (radiogenic) of the China Hill member of the Rogerson Formation. Open symbols indicate outliers, and solid and dashed lines probability distribution excluding and including outliers, respectively. Individual analyses are shown with one-sigma errors and the weighted mean age with two-sigma uncertainty is indicated by gray bar. $^{39}Ar/^{40}Ar$ inverse isochron diagram (inset).

Figure S5;
Black Canyon Member sample RG-10.1-013 (Lab. ID. 2449; formerly BBU-4)

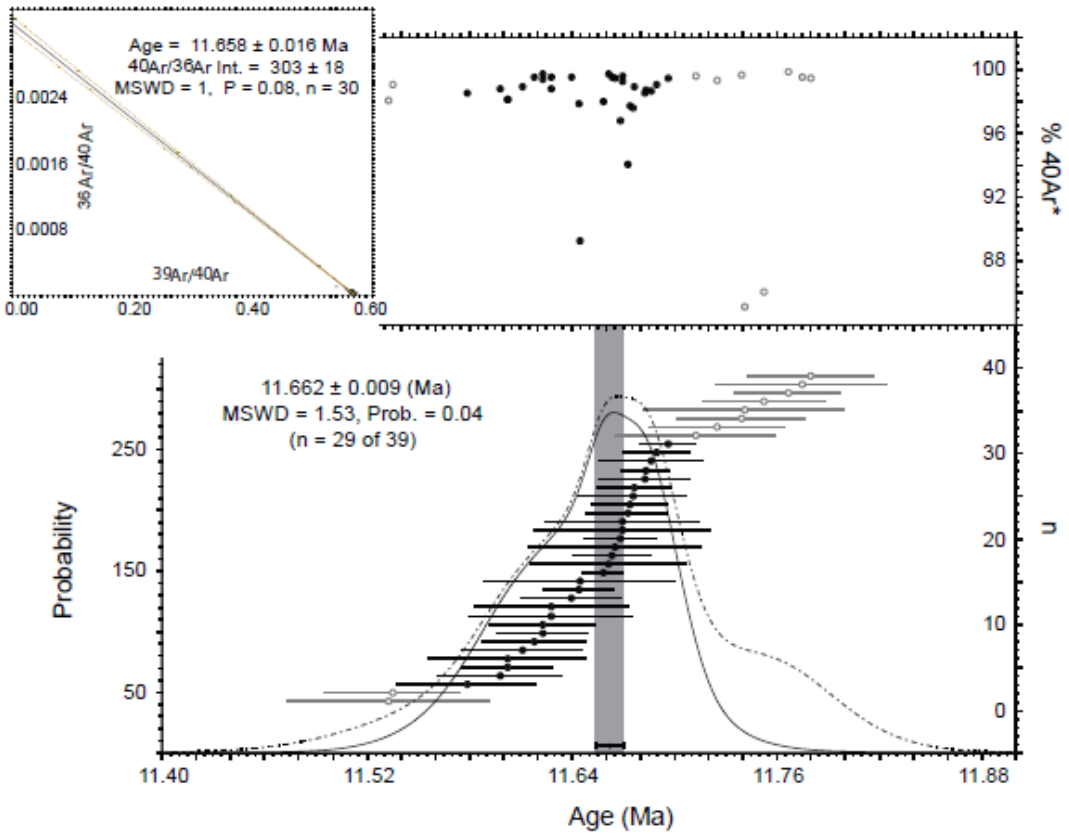

Figure S5: $^{40}Ar/^{39}Ar$ single sanidine age probability distribution and percent $^{40}Ar^*$ (radiogenic) of the Black Canyon member of the Rogerson Formation. Open symbols indicate outliers, and solid and dashed lines probability distribution excluding and including outliers, respectively. Individual analyses are shown with one-sigma errors and the weighted mean age with two-sigma uncertainty is indicated by gray bar. $^{39}Ar/^{40}Ar$ inverse isochron diagram (inset).

Figure S6;
Browns Bench Member sample RG-10.1-015 (Lab. ID. 2441)

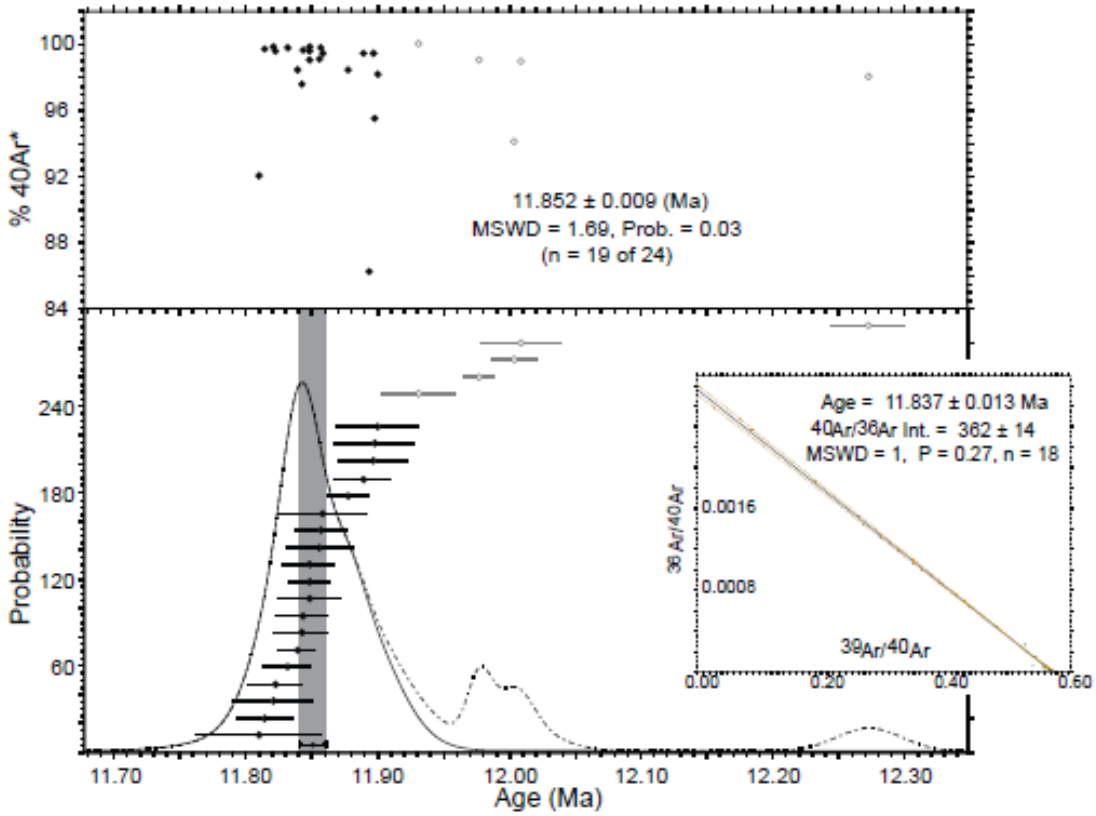

Figure S6 : $^{40}Ar/^{39}Ar$ single sanidine age probability distribution and percent $^{40}Ar^*$ (radiogenic) of the Brown's Bench member of the Rogerson Formation. Open symbols indicate outliers, and solid and dashed lines probability distribution excluding and including outliers, respectively. Individual analyses are shown with one-sigma errors and the weighted mean age with two-sigma uncertainty is indicated by gray bar. $^{39}Ar/^{40}Ar$ inverse isochron diagram (inset).

Figure S7:
Cougar Point Tuff VII sample CPT-10.2-001 (Lab. ID. 2481)

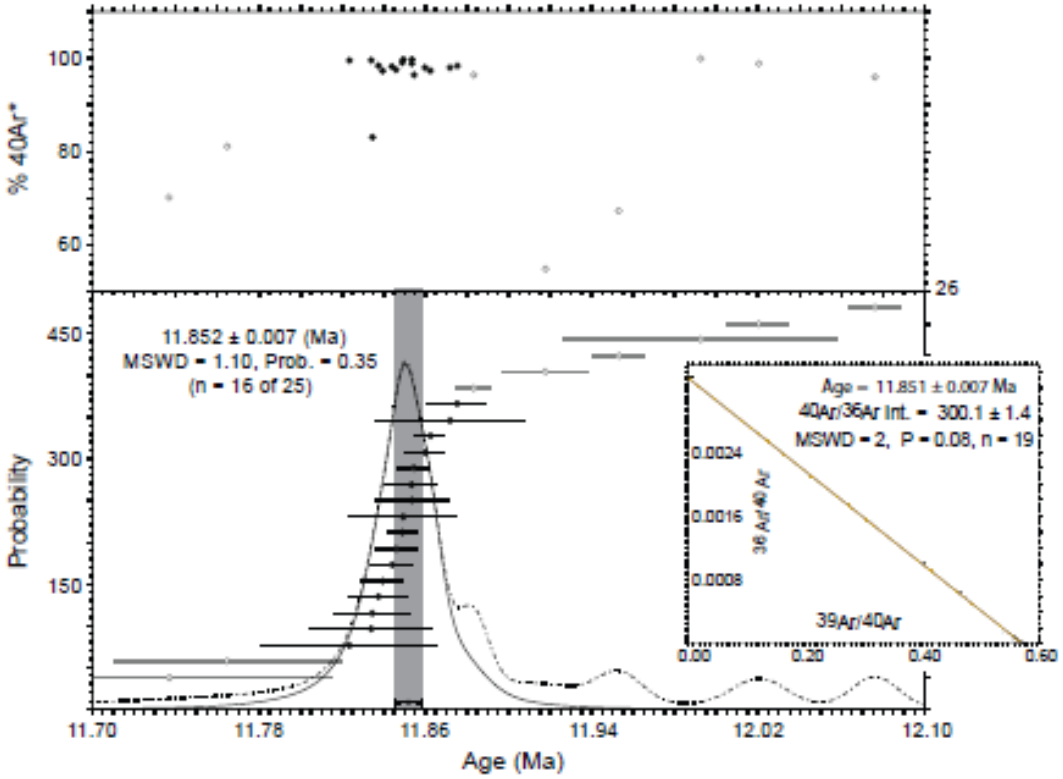

Figure S7 : $^{40}Ar/^{39}Ar$ single sanidine age probability distribution and percent $^{40}Ar^*$ (radiogenic) of Cougar Point Tuff VII. Open symbols indicate outliers, and solid and dashed lines probability distribution excluding and including outliers, respectively. Individual analyses are shown with one-sigma errors and the weighted mean age with two-sigma uncertainty is indicated by gray bar. $^{39}Ar/^{40}Ar$ inverse isochron diagram (inset).

Figure S8:
Cougar Point Tuff V sample CPT-11.2-001 (Lab. ID. 2493)

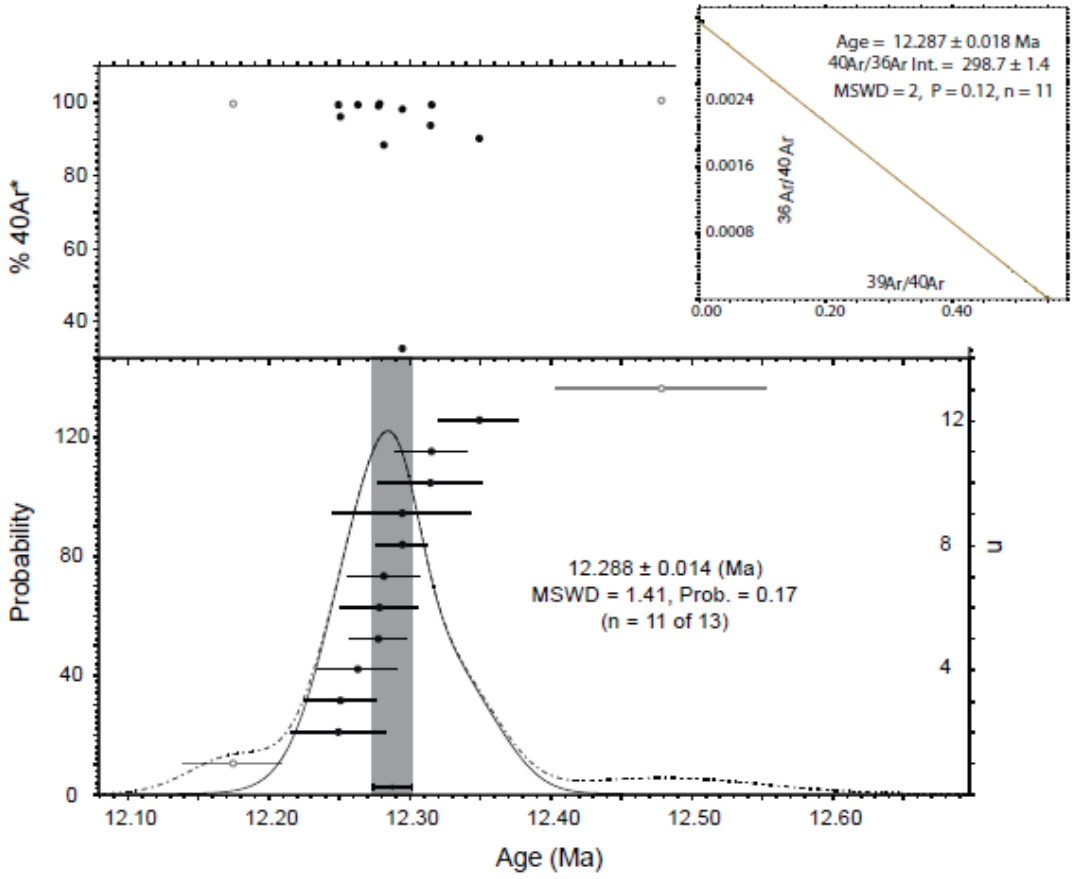

Figure S8 : $^{40}Ar/^{39}Ar$ single sanidine age probability distribution and percent $^{40}Ar^*$ (radiogenic) of Cougar Point Tuff V. Open symbols indicate outliers, and solid and dashed lines probability distribution excluding and including outliers, respectively. Individual analyses are shown with one-sigma errors and the weighted mean age with two-sigma uncertainty is indicated by gray bar. $^{39}Ar/^{40}Ar$ inverse isochron diagram (inset).